

CHAPTER IV

RESULTS AND

DISCUSSION

4. Results and Discussion

4.1 Determination of the effect of different washing agents on *Eri*, *Muga*, and *Pat* fabric

4.1.1 Microscopic image of *Eri*, *Muga*, and *Pat* fabric

The Microscopic visualization of *Eri* fabric (fig 4.1 (a)) and its treatment water (WATER) (fig 4.1 (b)), activated charcoal (CHARCOAL) (fig 4.1 (c)), lemon juice (CITRUS) (fig 4.1 (d)), detergent powder 1 (SUR) (fig 4.1 (e)), detergent powder 2 (TID) (fig 4.1 (f)), detergent bar (RIN) (fig 4.1 (g)), local made detergent bar (LOCAL) (fig 4.1 (h)), fabric stiffener (REVI) (fig 4.1 (i)), fabric conditioner (COMF) (fig 4.1 (j)), liquid detergent for silk and wool (EZY) (fig 4.1 (k)), and fabric whitener (VOX) (fig 4.1 (l)) are shown in Fig. 4.1.

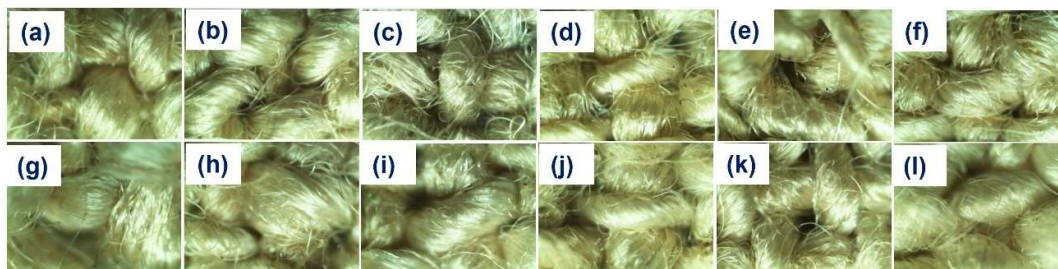


Fig. 4.1 Microscopic images of *Eri* fabric at 100X magnification of a) CONTROL b) WATER c) CHARCOAL d) CITRUS e) SUR f) TID g) RIN h) LOCAL i) REVI j) COMF k) EZY l) VOX

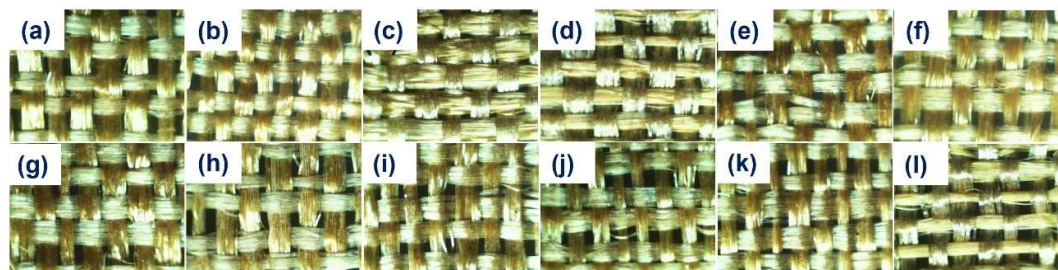


Fig. 4.2 Microscopic images of *Muga* fabric at 100X magnification of a) CONTROL b) WATER c) CHARCOAL d) KOLAKHAR e) SUR f) TID g) RIN h) LOCAL i) REVI j) COMF k) EZY l) VOX

The Microscopic visualization of *Muga* fabric (fig 4.2 (a)) and its treatment with water (WATER) (fig 4.2 (b)), activated charcoal (CHARCOAL) (fig 4.2 (c)), *Kolakhar* water (*KOLAKHAR*) (fig 4.2 (d)), detergent powder 1 (SUR) (fig 4.2 (e)), detergent

powder 2 (TID) (fig 4.2 (f)), detergent bar (RIN) (fig 4.2 (g)), local made detergent bar (LOCAL) (fig 4.2 (h)), fabric stiffener (REVI) (fig 4.2 (i)), fabric conditioner (CFC) (fig 4.2 (j)), liquid detergent for silk and wool (EZY) (fig 4.2 (k)) and fabric whitener (VOX) (fig 4.2 (l)) are shown in Fig. 4.2.

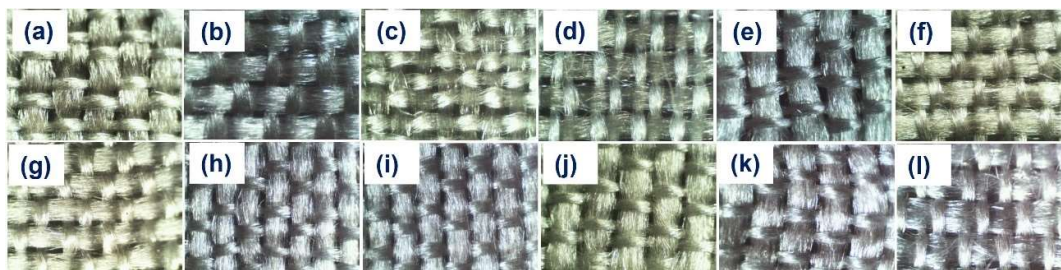


Fig. 4.3 Microscopic images of Pat fabric at 100X magnification of a) CONTROL b) WATER c) CHARCOAL d) CITRUS e) SUR f) TID g) RIN h) LOCAL i) REVI j) COMF k) EZY l) VOX

The microscopic visualization of *Pat* fabric (fig 4.3 (a)) and its treatment with washing agents, namely, water (WATER) (fig 4.3 (b)), activated charcoal (CHARCOAL) (fig 4.3 (c)), lemon juice (CITRUS) (fig 4.3(d)), detergent powder 1 (SUR) (fig 4.3 (e)), detergent powder 2 (TID) (fig 4.3 (f)), detergent bar (RIN) (fig 4.3 (g)), local made detergent bar (LOCAL) (fig 4.3 (h)), fabric stiffener (REVI) (fig 4.3(i)), fabric conditioner (COMF) (fig 4.3(j)), liquid detergent for silk and wool (EZY) (fig 4.3 (k)), and fabric whitener (VOX) (fig 4.3 (l)), are shown in Fig 4.3.

The microscopic images at 100X magnification taken in the Labomed Vision 2000 Binocular microscope showed the general surface change at the fabric level due to the use of different traditional and commercial washing agents compared to the untreated silk. From Fig. 4.1 of *Eri* treated samples, it can be seen that hairiness appearance increased in the cases of CHARCOAL, SUR, TID, RIN, LOCAL, COMF, and EZY; however, for WATER (fig 4.1 (b)), REVI (fig 4.1 (i)), and VOX (fig4.1 (l)), hairiness appearance was less compared to the rest. In the case of *Muga* washing, as seen in Fig. 4.2, VOX (fig 4.2 (l)) showed shrinkage in single yarns, whereas TID (fig 4.2 (f)) showed swelling of the yarns. Not much change was seen in the *Muga* yarns in the rest of the treatments. In the case of *Pat*, hairiness can be seen in the yarns CHARCOAL (fig 4.3 (c)) and VOX (fig 4.3 (l)), whereas other treatments show not much of a change as can be concluded from Fig. 4.3 for *Pat* fabrics. Not much detail can be extracted from

microscopic images, and hence, to study the surface in more detail at the fiber stage, SEM analysis was carried out.

4.1.2 Scanning Electron Microscope (SEM) image of *Eri*, *Muga* and *Pat* fabric

The technique of scanning electron microscopy (SEM) can be used to interpret and capture the structure of various materials at a variety of keV (kiloelectronvolt) energies and magnification levels [1]. Consequently, SEM is a non-destructive technique that enables direct imaging of a material in high-depth focus and at various magnifications. A SEM image is developed by sensing the electrons discharged as the exterior of the sample is scanned with an electron beam [2-4]. Thus, the use of SEM for silk analysis gives a better view at magnified levels [4].

The SEM results show the physical changes taking place due to different treatments. The results captured at 3000 X showed the surface of a single fiber. Alignment of the fibril structures can be seen clearly on the 10 μ m scales for all treated and untreated silk. The smooth fiber of *Eri* and *Pat* in their raw samples can be seen in Figs. 4.4 (a) and 4.6 (a). The surface of unwashed *Muga*, however, shows some unevenness, as can be seen in Fig. 4.5 (a). Damages have been reported with different washing agents, as evident from Fig. 4.4 for *Eri* silk, Fig. 4.5 for *Muga* silk, and Fig. 4.6 for *Pat* silk. Damages were more prominent in *Eri* and *Muga* treatments compared to *Pat* samples. *Eri* and *Pat* silk were washed with Citrus limon juice (Figs. 4.4 (d) and 4.6 (d)), whereas in the case of *Muga*, *Kolakhar* has been used (Fig. 4.5 (d)). For various silks, a single agent causes different damage. The comparison of damage types among the three silks and their respective washes is represented in Table 4.1.

In Fig. 4.4, the smooth raw *Eri* fiber shows no remains of sericin. The appearance of mild roughness in water-washed *Eri* is distinct. Peeling and fibrillation can be found in Charcoal-washed (fig 4.4 (c)), RIN-washed (fig 4.4 (g)), and LOCAL (fig 4.4 (h)) washed *Eri*. SUR-washed *Eri* (fig 4.4 (e)) shows crumpling of the surface, whereas TID (fig 4.4 (f)) and LOCAL (fig 4.4 (h)) washed *Eri* show complete degradation of fiber in many places and give a flaky appearance of the fibers [5]. VOX (fig 4.4 (l)) shows the removal of sericin by making the presence of two attached fibers visible.

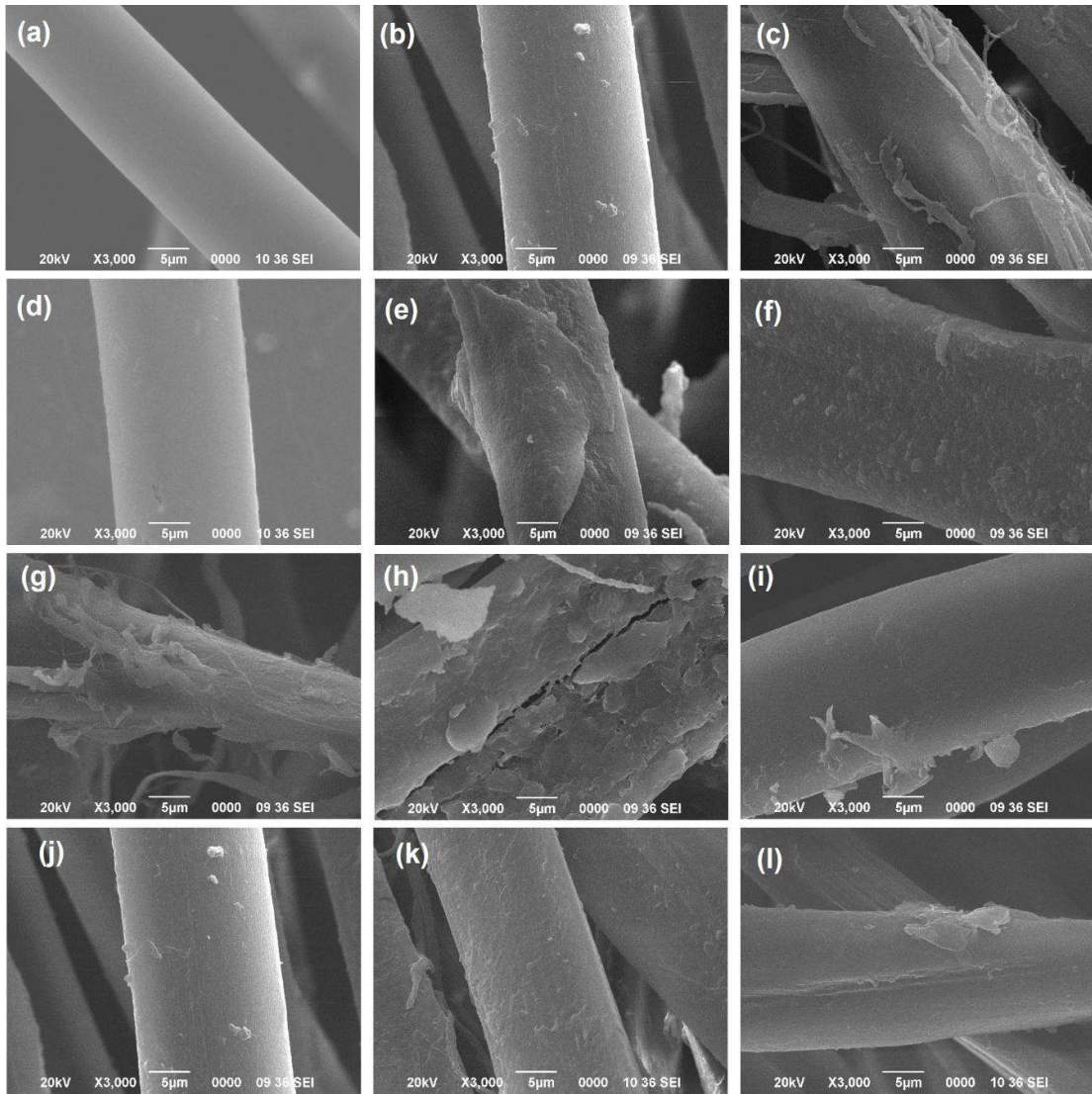


Fig. 4.4 SEM images of *Eri* fabric of a) CONTROL b) WATER c) CHARCOAL d) CITRUS e) SUR f) TID g) RIN h) LOCAL i) REVI j) COMF k) EZY l) VOX at 3000X magnification

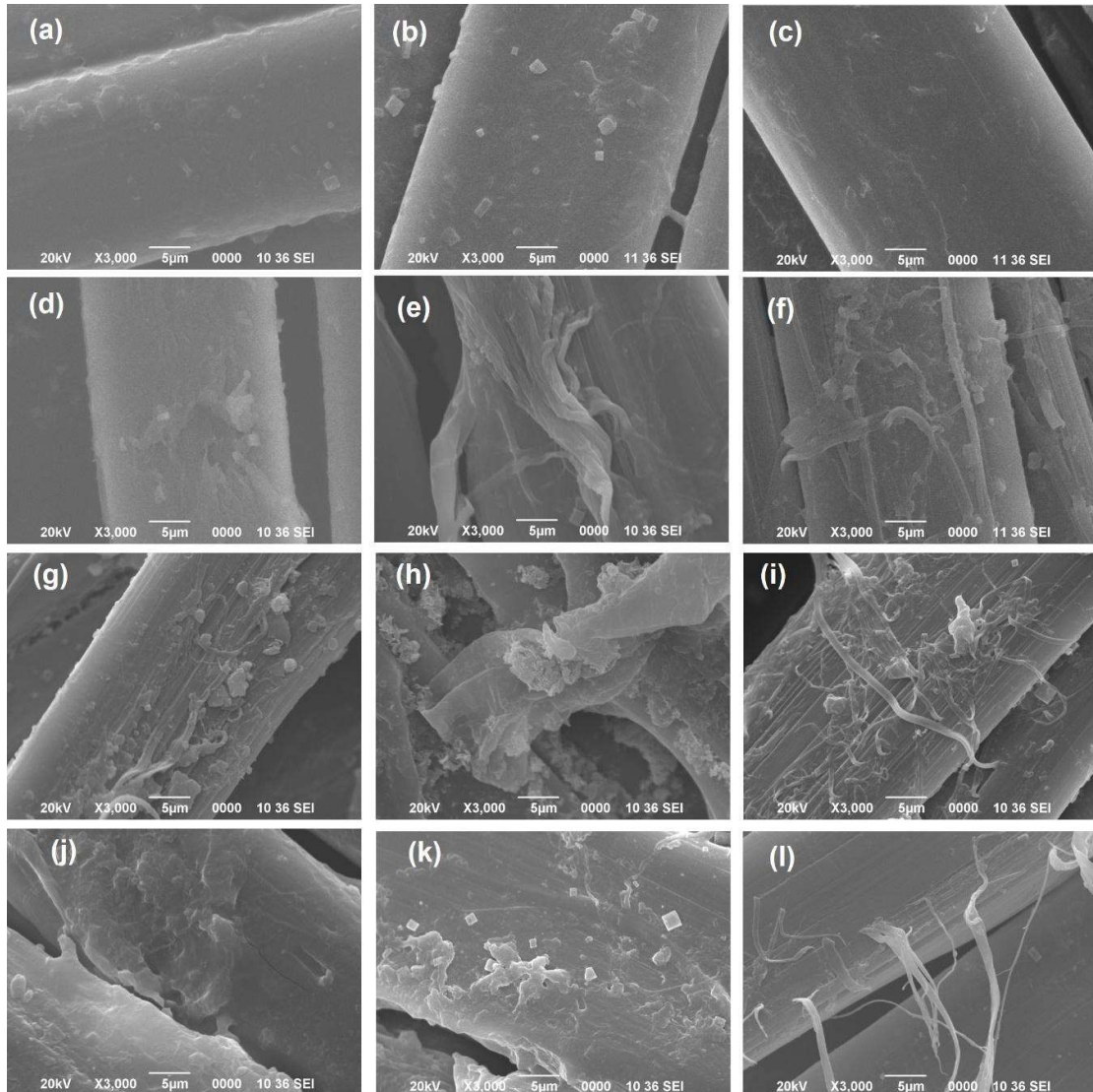


Fig. 4.5 SEM images of *Muga* fabric of a) CONTROL b) WATER c) CHARCOAL d) KOLAKHAR e) SUR f) TID g) RIN h) LOCAL i) REVI j) COMF k) EZY l) VOX at 3000X magnification

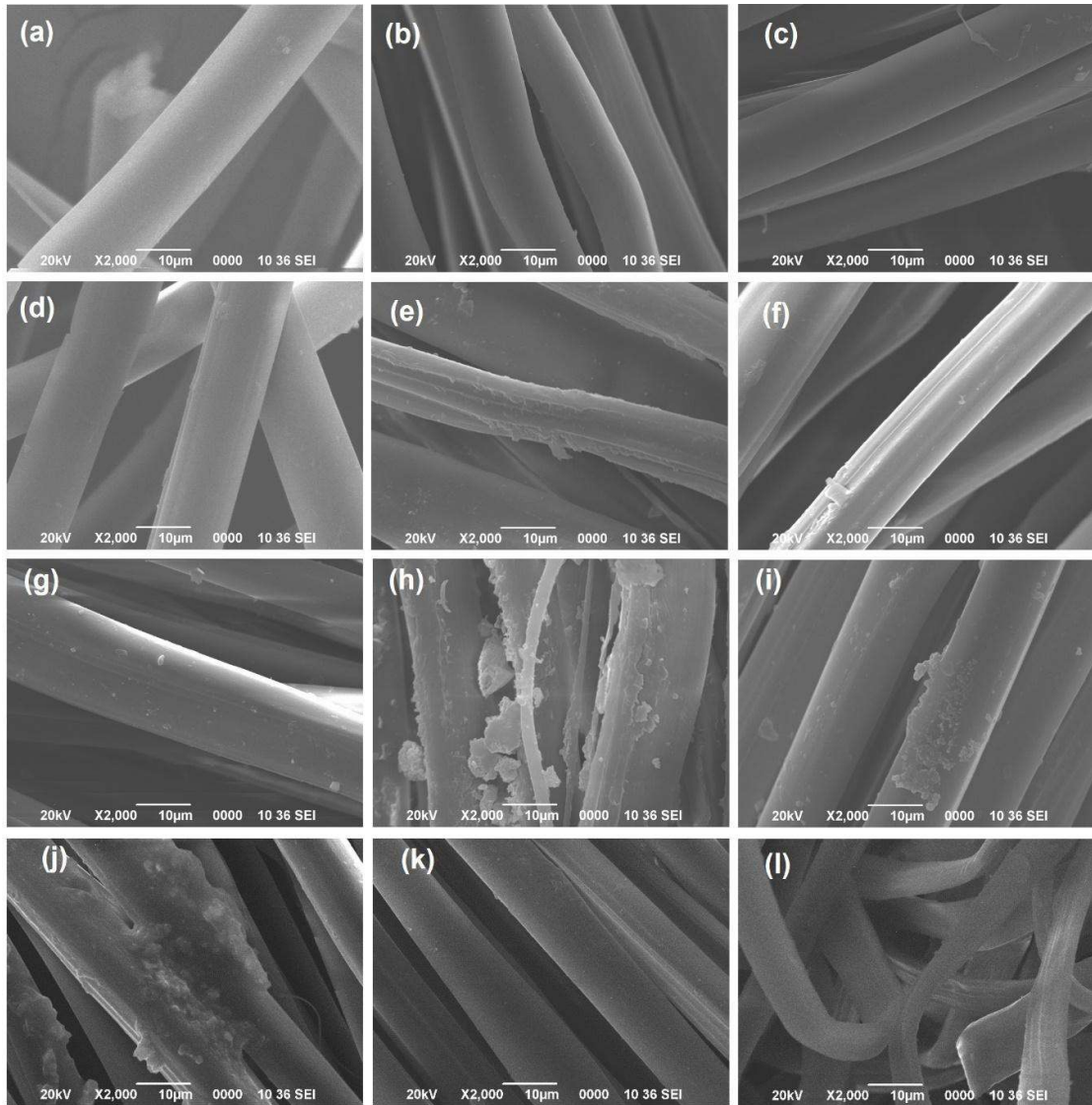


Fig. 4.6 SEM images of *Pat* fabric of a) CONTROL b) WATER c) CHARCOAL d) CITRUS e) SUR f) TID g) RIN h) LOCAL i) REVI j) COMF k) EZY l) VOX at 2000X

The surface of untreated *Muga* can be seen to have structures similar to stripes with grooves [6]. The wavy exterior of untreated *Muga* fiber has spots, which were suggested to appear as globular structures [6]. As seen in Fig. 4.5, when commercial agents like SUR (fig 4.5 (e)), TID (fig 4.5 (f)), RIN (fig 4.5 (g)), LOCAL (fig 4.5 (h)), REVI (fig 4.5 (i)), COMF (fig 4.5 (j)), EZY (fig 4.5 (k)), and VOX (fig 4.5 (l)) were used to treat *Muga* fabric, the results showed damage in the form of longitudinal fibrillation and fiber peeling. Other damage to the silk, such as wrinkling, peeling, blemishing, and fibrillation of the fiber, can also be observed [7, 8].

The SEM images of *Pat* fabric shown in Fig. 4.6 suggest a better result compared to washed *Eri* and *Muga* fabric. The SUR (fig 4.6 (e)) wash shows the appearance of dents in the fiber and some peeling, whereas the TID (fig 4.6 (f)) wash shows flattening of the fiber and the appearance of the bound fibroin in a single fiber. LOCAL (fig 4.6 (h)) shows complete tearing of the fiber along with scarring and crumpling. REVI (fig 4.6 (i)) and COMF (fig 4.6 (j)) show minor crumpling at specific locations, but no breakage or tearing has been seen. WATER (fig 4.6 (b)) and EZY (fig 4.6 (k)) washes showed similar results of mild flattening in some fibers [9]. The VOX (fig 4.6 (l)) washed *Pat* shows complete dried flattening in some fibers and mild flattening in the majority of the fibers [10].

The external structure of raw *Eri* silk fiber is similar to that of raw *Pat* fibers, with a smooth surface. However, stripe-like constructions with profound striations vertically were seen in the fibril in *Muga* silks [6]. The proteins that make up silk fibers are produced in the silk-gland cells, and the silk formation takes place by extending the liquid silk as the silkworm moves its head. Therefore, the morphological structures are related to the genetic code, and thus unique to each species [6]. In case of *Eri*, CHARCOAL (fig 4.4 (c)), RIN (fig 4.4 (g)), LOCAL (fig 4.4 (h)), COMF (fig 4.4 (j)), EZY (fig 4.4 (k)); for *Muga* SUR (fig 4.5 (e)), TID (fig 4.5 (f)), RIN (fig 4.5 (g)), LOCAL (fig 4.5 (h)), REVI (fig 4.5 (i)), COMF (fig 4.5 (j)), EZY (fig 4.5 (k)), VOX (fig 4.5 (l)); and for *Pat* LOCAL (fig 4.6 (h)), COMF (fig 4.6 (j)) all had visible surface particulate remains, which suggested surface erosion—the breakdown of individual silk sheets on the surface [11]. The comparison of damage types among the three silks and their respective washes is represented in Table 4.1. The SEM study highlighted the damage to the fiber level of the

Physico-chemical, Antibacterial, Antioxidant, Bio Compatibility, and Biodegradation Studies of Washed and Dyed Eri, Muga, and Pat Silk Fabric

silks. Identification of the agents that cause maximum damage has been provided. In the aforementioned treated samples, the increase in surface roughness is visible. The agent with maximum damage is LOCAL seen for all three silk fabrics and its composition is oil fat, caustic soda, sodium silicate, and rice bran. The main constituent of rice bran is starch (50%), and the Protein (considering fibroin here) and starch reaction might be a factor in the surface changes in the silk. According to studies, proteins can get adsorbed on the outer layer of starch granules, preventing water molecules from moving inside [12-16]. The protein-starch reaction might have contributed to the deformation of the fiber surface.

Table 4.1: Changes seen in the SEM images of treated and untreated *Eri, Muga,* and *Pat* fabric

	Smoothness			peeling			scarring			cracks			crumpling			Flattening			
	E	M	P	E	M	P	E	M	P	E	M	P	E	M	P	E	M	P	
Raw	+	+	+	-	-	-	-	-	-	-	-	-	-	-	-	-	-	-	-
WATER	+	+	+	-	-	-	+	-	-	-	-	-	-	-	-	-	-	-	-
CHARCOAL	-	+	+	+	-	-	-	-	-	+	-	-	-	-	-	+	-	-	-
CITRUS/KOLAKHAR	+	+	+	-	-	-	-	-	-	-	-	-	-	-	-	-	-	-	-
SUR	-	-	-	-	+	+	+	+	+	+	+	+	+	+	-	-	-	-	-
TID	-	-	+	-	+	-	+	+	-	+	+	-	+	-	-	-	-	-	+
RIN	-	-	+	+	+	-	+	+	-	+	+	-	+	-	-	+	+	-	-
LOCAL	-	-	-	+	+	+	+	+	+	+	+	+	+	+	+	+	+	-	+
REVI	-	-	-	+	+	-	-	+	-	-	+	+	-	-	-	-	-	+	-
COMF	-	-	-	-	-	-	+	+	+	-	+	-	-	+	+	+	-	+	-
EZY	-	-	+	-	-	-	+	+	-	-	+	-	-	+	-	-	+	-	-
VOX	-	-	-	+	+	+	+	-	+	+	+	+	-	-	+	+	-	+	-

Where, E= *Eri*, M=*Muga*, P= *Pat*, +=present, -=absent

4.1.3 Effect in the colour coordinates of *Eri*, *Muga*, and *Pat* fabric

The change in colour due to different treatments has been checked through RGB analysis, from which the luminosity %, saturation %, hue angle, Hex code, and the associated colour have been derived. A table with the results was created for easy comparison. The generated colour's individual code, which corresponds to its precise color coordinates, is called the hex code [17]. To have a better comparison of whether the derived colour matches the original, both the formulated colour and the scanned fabric are shown. The hue component of the HSL color space is comparable to human vision [18]. Using the data's inherent natural structure as a guide, it can accurately and quickly divide color into various partitions.

In the case of *Eri*, maximum Luminosity can be seen in VOX and minimum in the case of charcoal-washed *Eri* (Table 4.2). The saturation percentage was minimum for Water and Maximum for VOX, whereas if the Hue angle is considered, it was found that water wash *Eri* has the closest hue angle to control (Table 4.2). From Fig. 4.7, it is evident that the maximum colour deviation for *Eri* has occurred in VOX-treated samples, followed by LOCAL, RIN, and TID with almost the same deviation. The sequence of color deviations in *Eri*-treated samples is as follows: CHARCOAL < WATER < COMF < SUR < REVI < CITRUS < EZY < TID < RIN < LOCAL < VOX.

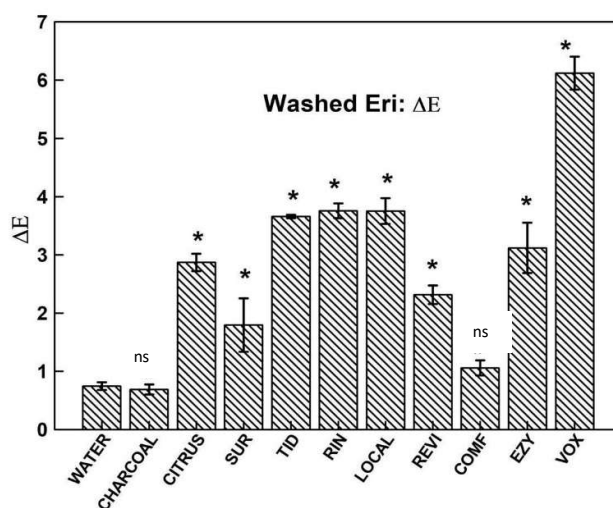


























Fig 4.7: Total difference in coloration (ΔE) of treated *Eri* fabric against untreated (Data are reported as mean \pm SD from three independent experiments; *P < 0.05 compared with control (water); *= significantly different, ns= non-significantly different)

Table 4.2: Luminosity %, Saturation %, Hue angle, colour code, Fabric colour, and associated colour (hex) of Raw (control) and treated Eri samples

Sample	Luminosity	Saturation	Hue angle	Hex code	Fabric	Hex
CONTROL	68.30±0.66	22.71±1.1	24.50±0.09	#c0aa9b		
WATER	68.53±0.17	21.47±0.21	24.38±ND	#c1ad9f		
CHARCOAL	67.79±0.17	21.68±0.57	25.30±0.13	#bfaa9b		
CITRUS	69.60±0.60	30.38±0.26	26.79±0.33	#c9b09c		
SUR	70.66±0.43	26.08±0.59	25.63±0.15	#c8b2a2		
TID	73.25±0.03	27.92±0.07	25.86±0.02	#cdb8a7		
RIN	73.18±0.18	26.95±0.17	26.57±0.03	#cdb8a8		
LOCAL	73.42±0.31	25.76±0.11	25.61±0.04	#ccb8a8		
REVI	71.27±0.17	23.65±0.14	25.48±0.07	#c7b2a3		
COMF	69.65±0.26	24.61±0.23	25.43±0.13	#c6af9f		
EZY	72.22±0.64	23.63±0.41	26.15±0.12	#c9b5a6		
VOX	76.03±0.42	32.80±0.52	28.66±0.15	#d6c1ae		

Hue, Saturation, and Lightness are the three main characteristics of a surface color. Hue enables a particular color to identify an object as red, blue, yellow, green, etc. Hue is primarily what differentiates one surface color from another [18]. Saturation is defined as the hue's strength or the colour's intensity, i.e. the colour's brightness or dullness [19, 20]. Lightness describes the luminosity of a color, such as black (total absorption) and white (total reflection) [21]. CIELAB is the most comprehensive color space defined by the International Commission on Illumination [19]. It describes all visible colors to the human eye and was designed as a device-independent reference model. Because of its widespread application, the CIE LAB system was utilized in order to perform the measurement of the color coordinates [19, 22].

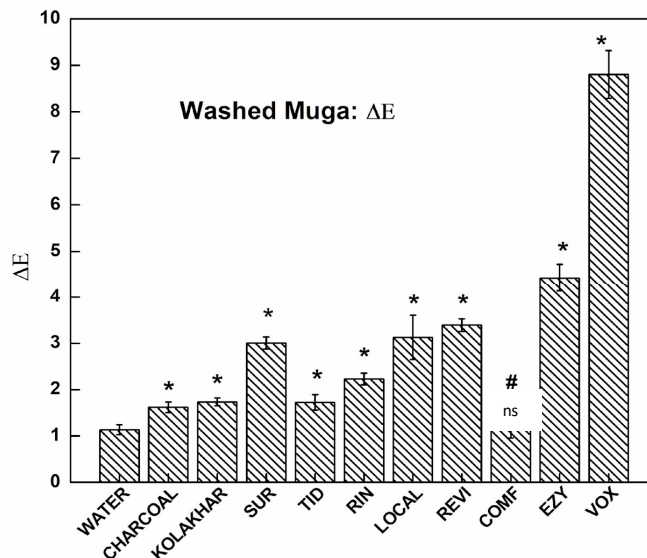


























Fig 4.8: Total difference in coloration (ΔE) of treated *Muga* samples against untreated (Data are reported as mean \pm SD from three independent experiments; *P < 0.05 compared with control (water); *= significantly different, ns= non-significantly different)

As can be seen in Table 4.3 for *Muga* treated and untreated samples, the maximum increase in Luminosity can be seen for VOX, followed by EZY, and the least increase was seen in the case of RIN, whereas a decrease in Luminosity percentage can be observed for TID and WATER in the case of *Muga*. The sequence in ascending order of colour deviation of *Muga*, also shown in Fig 4.8, is as follows:

WATER < COMF < CHARCOAL < TID < KOLAKHAR < RIN < SUR < LOCAL < REVI < EZY < VOX.

The increased luminosity, as well as colour deviation in VOX, is assumed to be due to the presence of oxidative or bleaching agents. Utilizing bleaches causes coloured materials to oxidize into colourless ones. This is accomplished by the chromophore's internal bonds being broken, resulting in small parts that don't absorb light (at least not in the visible spectrum) [23-25]. Additionally, these fragments usually dissolve better in washing water. Oxygen-based and chlorine-based bleaches are the two types of cleaning agents used [23, 25]. VOX uses an oxygen-based formula; here, a white powder called sodium percarbonate is used instead. The primary oxidizing agent is hydrogen peroxide, which decomposes into oxygen and water. Here, the starting material is a fairly stable powder (with the condition of being dry), and the by-products are harmless substances like sodium carbonate and water samples that have increased luminosity with lower saturation suggesting the presence of some bleaching agents in them.

Table 4.3: Luminosity %, Saturation %, Hue angle, colour code, Fabric colour and associated colour (hex) of Raw (control) and treated *Muga* samples

Sample	Luminosity	Saturation	Hue angle	Hex code	Fabric	Hex
CONTROL	65.76±0.22	37.42±0.32	23.21±0.06	#c8a188		
WATER	65.58±0.41	36.44±0.35	24.71±0.10	#c8a389		
CHARCOAL	66.86±0.52	34.57±0.18	24.93±0.04	#c8a68d		
KOLAKHAR	67.26±0.19	40.76±0.50	25.39±0.01	#cda588		
SUR	67.96±0.23	41.16±0.36	26.31±0.20	#cfa98c		
TID	64.15±0.19	36.36±0.06	25.28±0.10	#c49e82		
RIN	65.60±0.78	34.09±0.58	26.37±0.05	#c6a48b		
LOCAL	69.58±0.72	37.44±1.04	24.12±0.07	#cfad96		
REVI	70.05±0.15	41.30±0.26	24.58±0.10	#d2ad93		
COMF	66.88±0.30	40.73±0.22	24.67±0.04	#cda588		
EZY	71.34±0.41	42.07±0.60	24.92±0.15	#d4b096		
VOX	74.82±0.19	47.70±0.19	30.64±0.09	#dec0a1		

Physico-chemical, Antibacterial, Antioxidant, Bio Compatibility, and Biodegradation Studies of Washed and Dyed Eri, Muga, and Pat Silk Fabric

In the case of *Pat*-treated samples, LOCAL showed the highest luminosity percentage, whereas charcoal-treated samples showed the lowest luminosity, as can be seen in Table 4.4. The background of *Pat*'s colors was made black to avoid color confusion with the white background (Table 4.4). The color deviation suggests CHARCOAL has the highest deviation, whereas WATER and TID have the least color deviation, as shown in Fig. 4.9. The remains of Charcoal particles in the case of *Pat* might be the possible reason for the color deviation. Interestingly, EZY shows no damage to *Pat* silk; however, it shows significant color deviation, suggesting that EZY may have targeted the color component of the *Pat* silk. In another set, LOCAL shows clear damage to the fiber in SEM images, but color analysis suggests an insignificant color deviation. The sequence, in ascending order of colour deviation, is as follows:

TID < WATER < RIN < LOCAL < VOX < SUR < COMF < REVI < CITRUS < EZY
< CHARCOAL

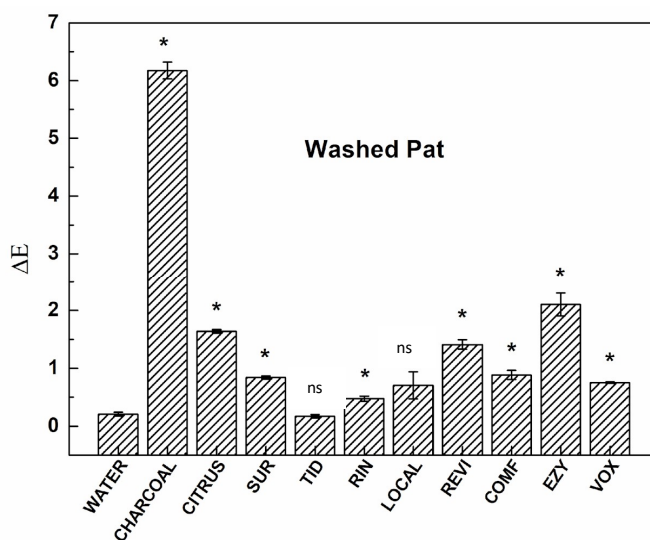

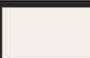

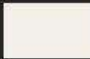

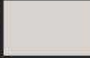

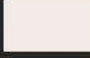



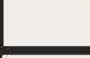














Fig 4.9: Total difference in coloration (ΔE) of treated *Pat* samples against untreated (Data are reported as mean \pm SD from three independent experiments; *P < 0.05 compared with control (water); *= significantly different, ns= non-significantly different)

TABLE 4.4 : Luminosity %, Saturation %, Hue angle, colour code, Fabric colour and associated colour (hex) of Raw (control) and treated *Pat* samples

Sample	Luminosity	Saturation	Hue angle	Hex code	Fabric	Hex
CONTROL	94.21±0.11	24.82±0.36	36.99±0.35	#f3f1ec		
WATER	94.00±0.21	24.78±0.76	37.30±0.24	#f4f1ec		
CHARCOAL	83.63±0.25	08.06±0.06	28.32±0.07	#d9d6d3		
CITRUS	92.82±0.11	33.00±0.47	38.84±0.18	#f3efe7		
SUR	93.62±0.07	21.40±0.39	30.16±0.17	#f3f0ec		
TID	94.11±0.04	24.13±0.52	35.63±0.05	#f3f0ec		
RIN	93.88±0.16	19.61±0.60	41.06±0.49	#f3f1ed		
LOCAL	94.92±0.36	20.88±1.14	41.38±0.80	#f5f3f0		
REVI	91.62±0.14	18.72±0.16	35.78±0.22	#eeebe7		
COMF	93.59±0.10	29.74±0.30	39.13±0.17	#f4f0ea		
EZY	90.64±0.39	19.63±0.40	32.74±0.16	#ede9e3		
VOX	94.34±0.06	16.89±0.20	38.05±0.14	#f2f0ed		

4.1.4 FTIR analysis of treated and untreated *Eri*, *Muga*, and *Pat* fabric

Fourier transform infrared (FTIR) spectroscopy is a standard method used in the study of proteins, as proteins have the majority of their information within an infrared spectrum [26,27]. FTIR, being a non-destructive process, can locate a wide range of functional groups; it is also sensitive to slight structural changes in the molecule. It is used for the detection of small soluble to large membrane proteins. Apart from being easy in sample preparation, in spectrum of protein contains all the information from conformation, side-chains, and environment [28-31]. FTIR spectroscopy is important for the information of protein folding/unfolding [32]. After adsorption, heating, and storage of solutions and emulsions, FTIR spectroscopy has also been used to detect changes in the secondary structure of protein molecules [33].

The control and treated silks were powdered and mixed with KBr. The recording of the spectrum has been carried out from 4000-400 cm⁻¹. The FTIR graphs have been divided into non-commercial agents and commercial agents and compared with the control [7,34].

As can be seen in Fig. 4.10, control *Eri* and washed *Eri* have the main signature almost intact; however, some formation of peaks, shifting of peaks, and deletion of some peaks were found. Table 4.5 shows the changes in peaks and their association with control *Eri* and washed *Eri*. In Table 4.8, the associated peaks with secondary structure have been mentioned.

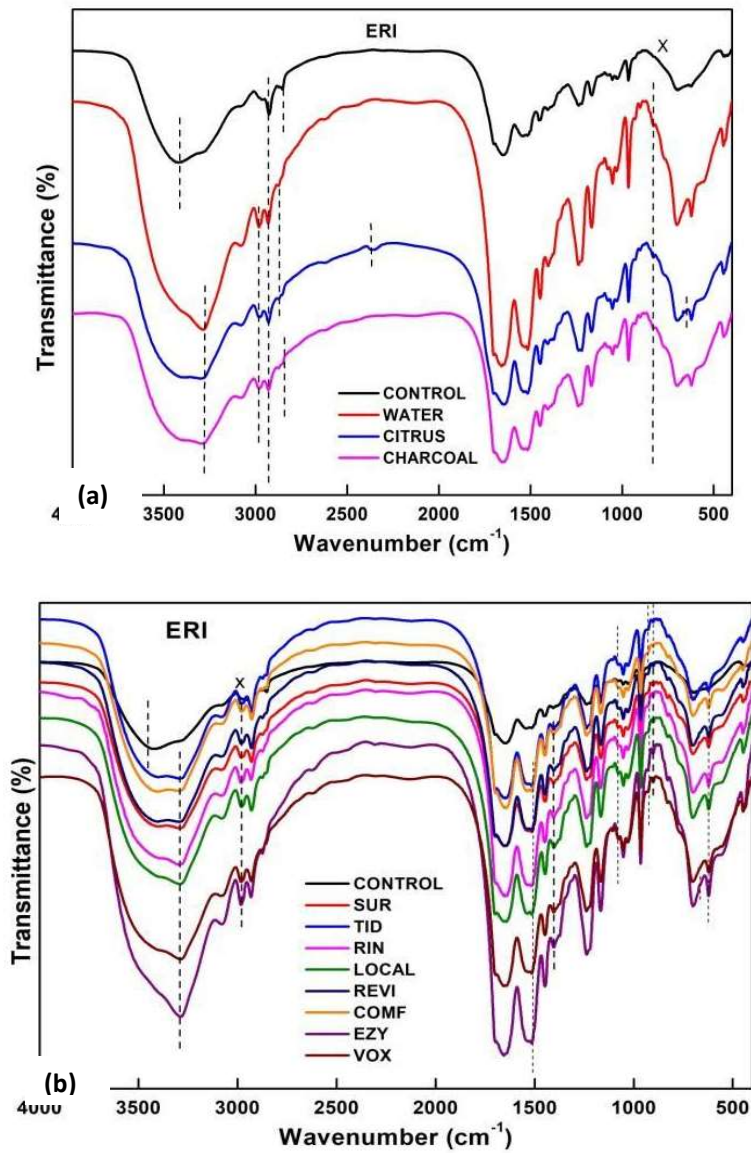


Fig 4.10: FTIR spectra of *Eri* treated with a) non-commercial, b) commercial washing agents

Physico-chemical, Antibacterial, Antioxidant, Bio Compatibility, and Biodegradation Studies of Washed and Dyed Eri, Muga, and Pat Silk Fabric

Table 4.5: FTIR peaks and corresponding functional groups of washed *Eri* sample

SAMPLES (<i>ERI</i>)	PEAKS (cm ⁻¹)	ASSOCIATION	LITERATURE	REF
ALL	3079-3086	Unsaturated (C=C-H) and/or aromatic rings	3150-3000	
ALL	2978-2982	Not found		
ALL	2927-2931	Methylene C-H asym	2935-2915	[35]
ALL	2873-2875	Methyl (-CH ₃) C-H Symmetric stretch	2880-2860	[36]
CONTROL, TID, LOCAL, COMF	2854-2855	Methylene (-CH ₂ -) C-H Symmetric stretch	2865-2845	[36]
CONTROL, WATER, CITRUS, SUR, TID, LOCAL, REVI, COMF, VOX	1698-1699	stretching C=O in aromatic carboxylic acids	1680-1740	[37]
ALL	1650-1658	C=O stretching	1650-1750	[38]
CITRUS, TID, LOCAL, COMF, VOX	1627-1650	C=O	1627-1650	[38]
CONROL, WATER, CITRUS, CHARCOAL, RIN, LOCAL, REVI, COMF	1530-1543	N-O	1550-1500	[39]
ALL	1514-1516	C-C aromatic compounds	1514-1521	[40]
ALL	1446-1453	Methylene C-H bend (=CH ₂)	1485-1445	[36]
ALL	1403-1407	COO ⁻ symmetric stretches.		[41]
ALL	1236-1239	Aromatic ethers,	1230-1270	[36]
ALL	1166-1167	C-O stretching and C-H bending	1166 cm ⁻¹	[42]
ALL	1077-1080	Primary amine, CN stretch	1090-1020	[36]
SUR, TID, RIN, LOCAL, REVI, COMF, EZY, VOX	1105-1107	C-C and C-O-C, Organic siloxane or silicone (Si-O-C)	~1105, 1110-1080	[43]
ALL	1052-1053	Methylene Cyclo-hexane ring vibrations	1055-1000	[35]
ALL	1028-1031	C-O stretching.	~1028	[44]
ALL	965	trans-C-H out-of-plane bend	970-960	[36]
WATER, CHARCOAL, REVI, EZY, VOX	929-930	deformational vibrations (C-H)	~930	[45]
WATER, CITRUS, CHARCOAL, SUR, TID, RIN, LOCAL, REVI, COMF, EZY, VOX	901-902	not known		
WATER, CHARCOAL, SUR, TID, RIN, LOCAL, REVI, COMF, EZY	876-877	CO ₃ ²⁻	877	[46]
WATER, CITRUS, CHARCOAL, SUR, TID, RIN, LOCAL, REVI, COMF, EZY, VOX	829	bending of a strong C-H aromatic bending group		[47]
CONTROL, WATER, CHARCOAL, SUR, TID, RIN, LOCAL, REVI, COMF, EZY, VOX	697-703	Thiol or thioether, CH ₂ -S- (C-S stretch)	710-685	[36]
CITRUS	660	out of plane (OOP) -C-H bonds	660	[48]
RIN, REVI	560	PO ₄ ³⁻	560	[49]
ALL	621-625	Alkyne C-H bend	680-610	[36]
ALL	446-448	Aryl disulfides (S-S stretch)	500-430	[36]
VOX	412	not found		

FTIR analysis of *Eri* treated and untreated samples shows majority of the peaks remained unchanged. However, there have been a few changes to some specific agent washing procedures. With the exception of TID, LOCAL, and COMF, (table 4.5) the Methylene (-CH₂-) C-H Symmetric Stretch (2865-2845 cm⁻¹) of the control (*Eri*) was lost during the treatments [36]. CHARCOAL, RIN, and EZY were deficient in the aromatic carboxylic acid (1680-1740 cm⁻¹) C=O stretching [37]. All of the *Eri* samples have been found to exhibit C=O stretching; however, the C=O groups of the hydrogen-bonded peptide moieties in the CITRUS, TID, LOCAL, COMF, and VOX samples have formed strong bands at 1627–1650 cm⁻¹ [38].

The main component of amide I absorption is the amide group's C-O stretching vibrations. Infrared radiation with various wave numbers is absorbed by the amide C-O bonds present in various secondary structures. This happens as a result of hydrogen bonds between N-H and C-O, which are affected by the conformations that protein chains adopt [6]. These hydrogen bonds cause the frequency of vibration of C-O in the protein backbone to change. Its association with the OH bend is supported by a distinct peak that can be seen at 1400 cm⁻¹ that is caused by the CH₄ group frequencies of alanine [36,50]. Peak formation was seen in SUR, TID, RIN, LOCAL, REVI, COMF, EZY, and VOX, as seen in Table 4.5 between 1105 cm⁻¹ and 1107 cm⁻¹, which is thought to be the result of either C-C and C-O-C, organic siloxane, or silicone (Si-O-C). Since silicone is frequently used in the production of silicone-based materials like elastomers, resins, foams, and coatings, the likelihood of the peak having a link to silicone is higher [43, 51]. For WATER, CHARCOAL, REVI, EZY, and VOX, (table 4.5) deformational vibration (C-H) at peak 930 cm⁻¹ was observed to have recently formed [45]. A peak at 901 cm⁻¹ and 902 cm⁻¹ has been formed in all treated samples. All of the samples that were treated have formed a peak at 901 cm⁻¹ and 902 cm⁻¹. In all of *Eri*'s treatments, a strong C-H aromatic bending group has bent, whereas this group was not present in Control [47]. Thiol or thioether peak was absent after CITRUS treatment; instead, the formation of out-of-plane (OOP) -C-H bonds at 660 cm cm⁻¹ was observed [48]. Peak formation, which is attributed to PO4 -3, is shown by RIN and REVI (table 4.5) [49]. In both treated and untreated *Eri* samples, aryl disulfides (S-S stretch) were discovered [36].

Physico-chemical, Antibacterial, Antioxidant, Bio Compatibility, and Biodegradation Studies of Washed and Dyed Eri, Muga, and Pat Silk Fabric

Table 4.6: Assignments of FTIR peaks to secondary structure for protein of control and washed *Eri* samples

SAMPLE	PEAK 1 (cm ⁻¹)	PEAK 2 (cm ⁻¹)	PEAK 3 (cm ⁻¹)	PEAK 4 (cm ⁻¹)	PEAK 5 (cm ⁻¹)
CONTROL	1698 β-turn conformation of the hairpin-folded antiparallel β-sheet structure	1651 Random Coil/ α-helix	1543 Random coil/ α-helix	1238 Random coil/ β-sheet	X
WATER	1697 β-turn conformation of the hairpin-folded antiparallel β-sheet structure	1658 random coil/α-helix	1530 β-sheet	1239 Random coil/ β-sheet	X
CITRUS	1699 β-turn conformation of the hairpin-folded antiparallel β-sheet structure	1639 Random coil/extended chains/ intramolecular β-sheets	1538 Random coil/ α-helix	1236 Random coil/ β-sheet	660 Random coil
CHARCOAL	X	1654 Random coil/ α-helix	1534 β-sheet	1239 Random coil/ β-sheet	X
SUR	1698 β-turn conformation of the hairpin-folded antiparallel β-sheet structure	1654 Random coil/ α-helix	X	1239 Random coil/ β-sheet	X
TID	1698 β-turn conformation of the hairpin-folded antiparallel β-sheet structure	1649 Random coil/ α-helix	X	1239 Random coil/ β-sheet	X
RIN	X	1651 Random coil/ α-helix	1538 Random coil/ α-helix	1239 Random coil/ β-sheet	X
LOCAL	1698 β-turn conformation of the hairpin-folded antiparallel β-sheet structure	1642 Random coil/ extended chains	1537 Random coil/ α-helix	1238 Random coil/ β-sheet	1658 α-helix
REVI	1699 β-turn conformation of the hairpin-folded antiparallel β-sheet structure	1643 Random coil/extended chains	1540 Random coil/ α-helix	1239 Random coil/ β-sheet	X
COMF	1699 β-turn conformation of the hairpin-folded antiparallel β-sheet structure	1649 Random coil/ α-helix	X	1239 Random coil/ β-sheet	1640 Random coil
EZY	X	1656 Random coil/ α-helix	X	1239 Random coil/ β-sheet	X
VOX	1698 β-turn conformation of the hairpin-folded antiparallel β-sheet structure	1643 Random coil/ extended chains	X	1239 Random coil/ β-sheet	1657 α-helix
REFERENCE	[52]	[53,54]	[54]	[54]	[54]

Through FTIR analysis, it was possible to identify the secondary structure changes in *Eri* silk. It has been stated that with the water molecules transferring across the polymer molecular layers, a structure transformation will be induced. Even with very little water present and the system in a solid-like state, water molecules are still crucial to the polymer and water system [55]. β -sheets are formed mostly during the spinning of silk fiber. Insoluble β -sheet structures were formed in fibroin materials after they were subjected to solvents, physical stress, saline, and thermal treatment, which are mostly carried out during silk fiber processing [55]. The peak linked with *Eri* (control) (table 4.6 peak 1 control) at 1698 cm^{-1} is for β -turn conformation of the hairpin-folded antiparallel β -sheet structure which, gets missing in the case of CHARCOAL, RIN, and EZY washed *Eri* (table 4.6 peak 1). In the present analysis, we consider all literature on silk FTIR for identifying β -sheets and α -helix even if some contradict the other. *Eri* (control) shows the three conformations of β -turn conformation of the hairpin-folded antiparallel β -sheet structure, α -helix, and random coils. However, there were some visible conformational changes in WATER and CHARCOAL treatment where β -sheet has been formed represented by a peak at 1530 cm^{-1} and 1534 cm^{-1} against random coil/ α -helix in *Eri* (CONTROL) represented by a peak at 1543 cm^{-1} [51-53] as seen in table 4.6 peak 3. There were complete missing peaks close to 1543 cm^{-1} for SUR, TID, COMF, EZY, and VOX-treated *Eri*. It has been stated that the assignment of β -sheet structure has been controversial as different research groups suggest different ranges, and even researchers of the same group give different ranges in different papers [52]. The peak at 1238 cm^{-1} (table 4.5 peak 4) remains intact with very slight shifts but is in the same range. The peak at 1651 cm^{-1} for random coils and α -helix in CONTROL was shifted to β -sheets for CITRUS-treated *Eri*; LOCAL (1643 cm^{-1}), REVI (1642 cm^{-1}), and VOX (1642 cm^{-1}) have only random coils or extended chains as seen in table 4.6 peak 2. But there is another peak in the area connected to the α -helix for LOCAL (1658 cm^{-1}) and VOX (1657 cm^{-1}) [53, 54]. Furthermore, for CITRUS-washed *Eri*, peaks 700 assigned to β -sheets vanished [56]. Without ruling out the option that the high wavenumber band could be caused by the Amide III mode of the disordered chain, CONTROL, and all treatments have peaks at 1240 that are due to the splitting of amide III in the antiparallel α -sheet conformation [57]. Overall, it was discovered that CHARCOAL, RIN, and EZY were denaturing the secondary structure of the B-sheet, whereas SUR, TID, COMF, EZY, and VOX were

Physico-chemical, Antibacterial, Antioxidant, Bio Compatibility, and Biodegradation Studies of Washed and Dyed Eri, Muga, and Pat Silk Fabric

found to be denaturing the peak for the random coil/ α -helix because none of these peaks were found to be close to CONTROL *Eri* [52-54].

The FTIR spectrum of *Muga* of non-commercial and commercial washing agents has been shown in Fig 4.11, and the peaks associated with the difference are shown in Table 4.6. The secondary structure change derived from peak change is shown in Table 4.9

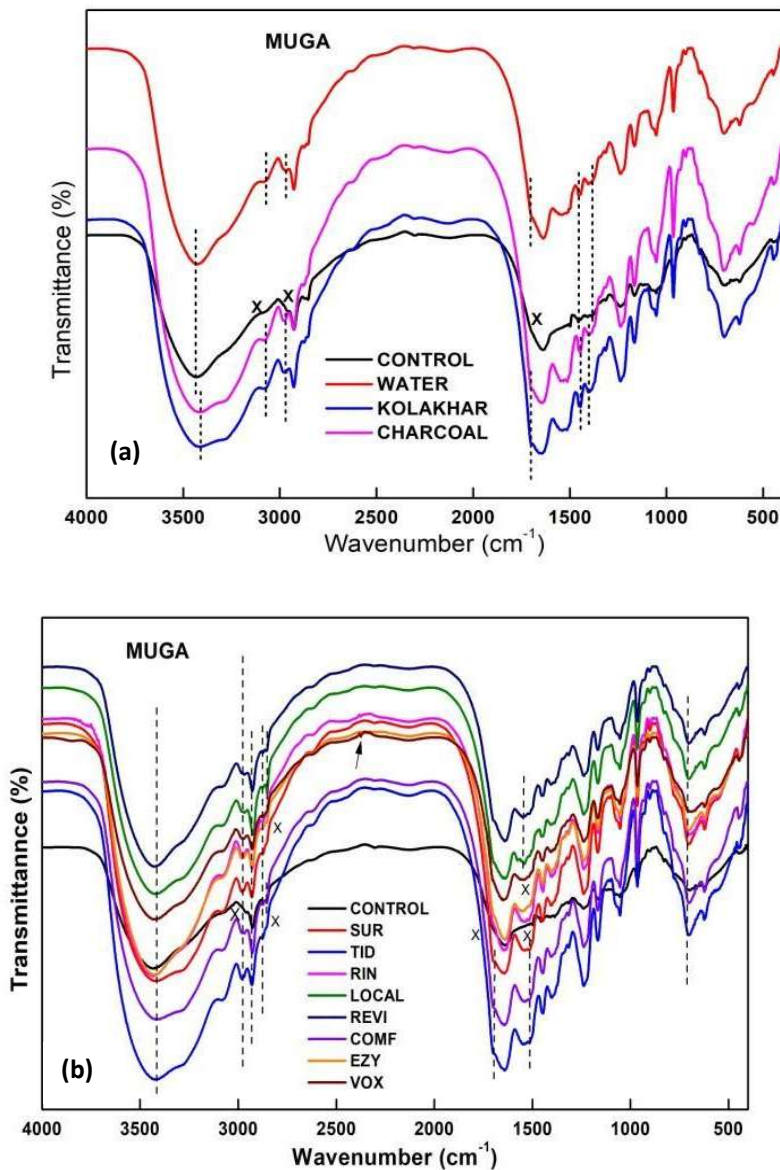


Fig 4.11: FTIR spectra of *Muga* treated with a) non-commercial, b) commercial washing agents

Physico-chemical, Antibacterial, Antioxidant, Bio Compatibility, and Biodegradation Studies of Washed and Dyed Eri, Muga, and Pat Silk Fabric

Table 4.7: FTIR peaks and corresponding functional groups of washed *Muga* samples

SAMPLES (Muga)	PEAKS (cm ⁻¹)	ASSOCIATION	LITERATURE	REF
All 3412-3434				
WATER, KOLAKHAR, CHARCOAL, SUR, TID, RIN, LOCAL, REVI, COMF, EZY, VOX	3079-3086	Aromatic C-H frame and Terminal (Vinyl) C-H stretch		
CONTROL, WATER, KOLAKHAR, LOCAL, REVI, COMF	2958-2970	Methyl C-H asymmetric stretch	2970-2950	
	All 2927-2930	Methylene C-H asym	2935-2915	[35]
	All 2870-2876	Methyl (-CH ₃) C-H Symmetric stretch	2880-2860	[36]
CONTROL, WATER, LOCAL, REVI, COMF	2852-2855	Methylene (-CH ₂ -) C-H Symmetric stretch	2865-2845	[36]
	All 1637-1648	Alkenyl C=C stretch, Secondary amine, NH bend, Open-chain imino (-C=N-)	1680-1620, 1650-1550, 1690-1590	[36]
WATER, KOLAKHAR, CHARCOAL, TID, RIN, LOCAL, REVI, COMF, EZY, VOX	1527-1547	N-O	1550-1500	[39]
	VOX 1554	N-H stretching	1554	[58]
	LOCAL 1576	C-C stretching	1576	[59]
CONTROL, WATER	1498, 1505	Aromatic ring stretch (C=C-C used as an approximation of the unique aromatic ring bonding)	1450-1510	[36,60]
KOLAKHAR, CHARCOAL, SUR, TID, RIN, LOCAL, REVI, COMF, EZY, VOX	1514-1518	C-C aromatic compounds	1514-1521	[40]
	All 1445-1456	Methylene C-H bend (=CH ₂)	1485-1445	[36]
	All 1401-1409	COO- symmetric stretches.	1400-1420	[41]
CONTROL, WATER	1385	bending vibrations of -OH of phenols	1385	[61]
CONTROL, WATER, KOLAKHAR, CHARCOAL, SUR, TID, RIN, LOCAL, REVI, COMF, EZY	1314-1316	Phenolic -C-O and O-H stretching modes	~1314	[62]
	All 1237-1240	Aromatic ethers	1230-1270	[36]
	All 1165-1167	C-O stretching and C-H bending	1166	[42]
Exp VOX	1104-1120	Silicone, C-C and C-O-C	~1105	[36,43]
EXP TID	1053-1054	Methylene Cyclohexane ring vibrations	1055-1000	[35]
	All 965	trans-C-H out-of-plane bend	970-960	[36]
	EZY 929	deformational vibrations (C-H) vibration	~930	[35]
	All 903-901	not known		
EXP CONTROL, RIN, REVI	876-879	CO ₃ (2-)	877	[46]
EXP TID, VOX, RIN	695-704	Thiol or thioether, CH ₂ -S- (C-S stretch)	710-685	[36]
COTROL, WATER, LOCAL, RIN	662-680	Alkyne C-H bend	680-610	[36]
	All 621-623	Alkyne C-H bend	680-610	[36]
TID, RIN	557-560	Aliphatic iodo compounds, C-I stretch	600-500	[36]
	All 440-448	Aryl disulfides (S-S stretch)	500-430	[36]

The FTIR peaks of *Muga* control and treated are given in Table 4.7. Bands between 3079-3091 cm^{-1} were seen for all treated *Muga* samples except the control. These bands are linked with the Aromatic C-H frame and Terminal (Vinyl) C-H stretch [36]. A Fermi resonance doublet typically includes the amide-A stretch between 3310 cm^{-1} and 3270 cm^{-1} , and the second stretch (weak) absorbance, which is attributed to the amide-B stretch, is found between 3100 cm^{-1} and 3030 cm^{-1} . These two bands are prominent in the treatments, but the peak is missing in the CONTROL case [63]. The C-O stretch vibration, the desynchronized C-N stretching vibration, the N-H in-plane bend, and the C-N distortion, which induces tremors in the amide-I region near 1650 cm^{-1} , are all perceptible in all samples (table 4.7). Peaks near 1400 cm^{-1} in all samples are caused by alanine's CH₄ group frequency. In the amide II region, CONTROL and all treatments fall into aromatic nitro compounds. Additionally, all samples have a peak at 1445–1456 cm^{-1} that is attributed to aromatic ring stretch and methyl C–H asymmetric/symmetric stretch [36]. All of the peaks fall within the range of 1340–1456 cm^{-1} , which is typically attributed to the vibration mode of residues [31]. The aromatic amino group in the amide III region includes the aromatic primary amine (C-N stretch) (1340-1250 cm^{-1}), aromatic secondary amine (C-N stretch) (1350-1280 cm^{-1}), an aromatic tertiary amine (C-N stretch) (1360-1310 cm^{-1}), which overlaps all samples except for VOX where it vanished [36, 64, 65]. All of the peaks fall within the range of 1340 cm^{-1} to 1456 cm^{-1} (table 4.7), which is typically attributed to the vibration mode of residues [31]. A distinct peak can be seen at 1400 cm^{-1} , which is caused by the CH₄ group frequencies of alanine, supporting its association with the OH bend [36, 50]. The modification in molecular conformation was discovered to be consistent across all treatments, indicating that the treatments' chemical effects on the fabric were also consistent.

Physico-chemical, Antibacterial, Antioxidant, Bio Compatibility, and Biodegradation Studies of Washed and Dyed Eri, Muga, and Pat Silk Fabric

Table 4.8: Assignments of FTIR peaks to secondary structure for protein of control and washed *Muga* samples

SAMPLE	PEAK 1 (cm ⁻¹)	PEAK 2 (cm ⁻¹)	PEAK 3 (cm ⁻¹)	PEAK 4 (cm ⁻¹)
CONTROL	X	1638 random coils/extended chains	1316 α-helix	1239 β-sheet
WATER	1698 β-turn conformation of the hairpin-folded antiparallel β-sheet structure	1637 Random coils/ β-sheets	1315 α-helix	1239 β-sheet
KOLAKHAR	1698 β-turn conformation of the hairpin-folded antiparallel β-sheet structure	1642 random coils/extended chains	1315 α-helix	1239 β-sheet
CHARCOAL	1698 β-turn conformation of the hairpin-folded antiparallel β-sheet structure	1642 random coils/extended chains	1314 α-helix	1238 β-sheet
SUR	1702 β-sheets	1643 random coils/extended chains	1315 α-helix	1239 β-sheet
TID	1702 β-sheets	1642 random coils/extended chains	1314 α-helix	1240 β-sheet/random coils
RIN	1701 β-sheets	1643 random coils/extended chains	1316 α-helix	1237 β-sheet
LOCAL	1702 β-sheets	1641 random coils/extended chains	1316 α-helix	1239 β-sheet
REVI	1703 β-sheets	1641 random coils/extended chains	1314 α-helix	1239 β-sheet
COMF	1702 β-sheets	1641 random coils/extended chains	1315 α-helix	1238 β-sheet
EZY	1701 β-sheets	1640 random coils/extended chains	1315 α-helix	1239 β-sheet
VOX	1702 β-sheets	1648 random coils/ α-helix	x	1240 β-sheet/random coils
REF	[66]	[53,54]	[67]	[54]

The crystalline nature of a protein can be stipulated from β-sheet [66]. Stress in the fibroin protein and change in it can be because of relaxation in the fibroin protein leading to β-sheet [66]. The secondary structure of *Muga* control suggests it has a random

coil, α -helix, and β -sheet conformations. Formation of a new peak around 1515cm^{-1} was seen in all the treatments *KOLAKHAR*, CHARCOAL, SUR, TID, RIN, LOCAL, REVI, COMF, EZY, VOX that may be attributed to stretching vibration of C-N group and deformation vibration of N-H groups as well as the formation of β -Sheets in case of secondary structures [68, 69]. Except for the untreated sample, all samples ($1698\text{-}1703\text{ cm}^{-1}$) (table 4.8 peak 1) formed a small peak linked to the β -turn conformation of the hairpin-folded antiparallel β -sheet structure [66,70]; however, literature also suggests only β -sheet for peaks 1700cm^{-1} (table 4.8 peak 1), which include SUR, TID, RIN, REVI, LOCAL, EZY, COMF, and VOX [52, 66]. The peaks from 1638cm^{-1} - 1646cm^{-1} are associated with random coils and extended chains (table 4.8 peak 2), as seen in the cases of CONTROL, WATER, CHARCOAL, *KOLAKHAR*, SUR, TID, RIN, LOCAL, REVI, EZY, and COMF, but for VOX it is only associated with random coils (1647cm^{-1} - 1655cm^{-1}), while for WATER some literature also suggests the peak for β -Sheets [71]. Peak $\sim 1230\text{cm}^{-1}$ remained unchanged in all the treatments, which is attributed to β -Sheets (table 4.8 peak 4). The α -helix around 1315 cm^{-1} was found in all *Muga* treatments except for VOX (table 4.8 peak 3). Literature shows that in *Muga* α -helix and β -Sheets, conformation is present, and interconversion takes place for stress [6]. The peak in $\sim 964\text{cm}^{-1}$ (amide IV) was seen in all *Muga* samples that are associated with the crystalline region of β -phase [72]. The peak at $\sim 698\text{cm}^{-1}$ (amide V) was seen in all samples except for TID, RIN, and VOX also attributed to β -Sheets [73].

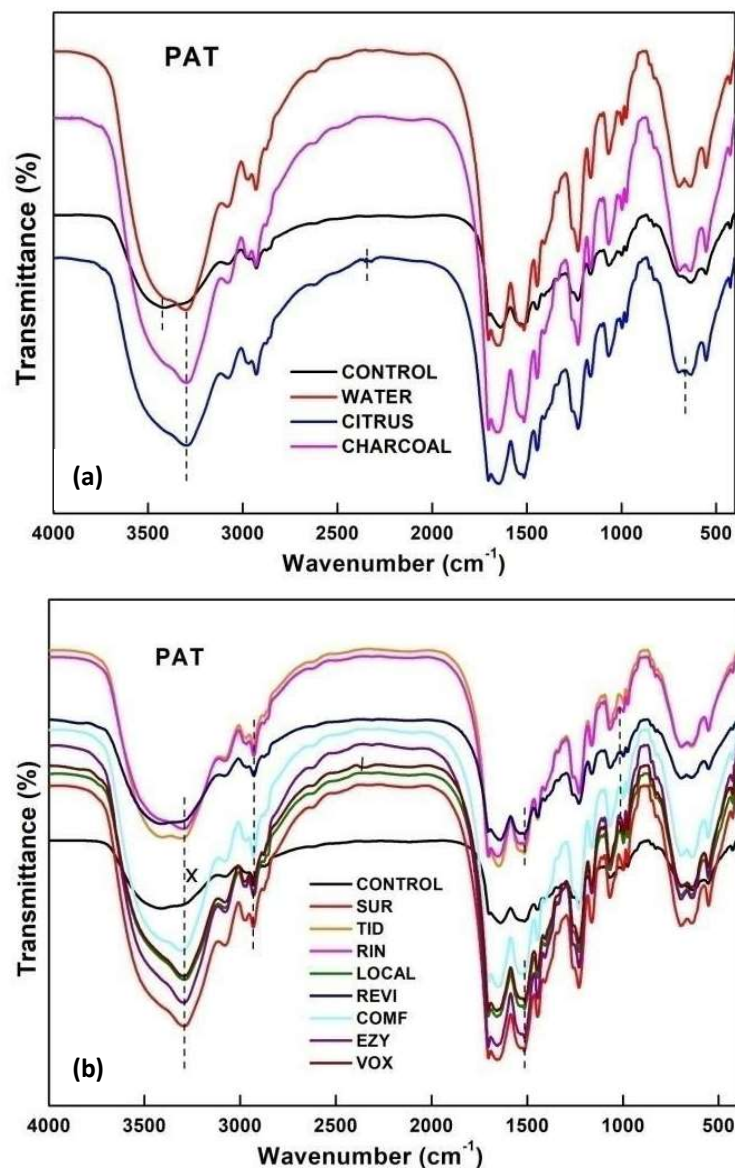


Fig 4.12: FTIR spectra of *Pat* treated with a) non-commercial, b) commercial washing agents

Fig. 4.12 shows the FTIR graph of *Pat* of non-commercial and commercial washing agents and the peaks associated with the difference are shown in Table 4.7. The secondary structure change derived from peak change is shown in Table 4.10.

Physico-chemical, Antibacterial, Antioxidant, Bio Compatibility, and Biodegradation Studies of Washed and Dyed Eri, Muga, and Pat Silk Fabric

Table 4.9: FTIR peaks and corresponding functional groups of washed *Pat* samples

SAMPLES (PAT)	PEAKS (cm ⁻¹)	ASSOCIATION	LITERATURE	REF
ALL	3079-3083	Unsaturation (C=C-H) and/or aromatic rings	3150-3000	
ALL	2928-2932	Methylene C-H asym	2935-2915	[35]
ALL	2875-2877	Methyl (-CH3) C-H Symmetric stretch	2880-2860	[36]
ALL	1698-1703	CO stretching	1698-1703	[74]
WATER, REVI	1532-1538	N-O	1550-1500	[39]
ALL	1514-1516	C-C aromatic compounds/CN stretching/NH bending	1514-1521	[40]
ALL	1445-1447	Methylene C-H bend (=CH2)	1485-1445	[36]
ALL	1407-1408	COO- symmetric stretches.	1400-1420	[41]
CONTROL, SUR, TID, RIN, LOCAL, REVI	1340-1341	bending vibration of alkanes, Organic phosphates (P=O stretch)	~1341, 1350-1250	[36,75]
CONTROL, RIN, REVI	1261	Organic phosphates (P=O stretch)	1350-1250	[36]
ALL	1230-1239	Aromatic ethers	1230-1270	[36]
ALL	1162-1163	C-O stretching and C-H bending	1166	[42]
ALL	1104-1105	Silicon, C-C, C-O-C	~1105	[36,43]
CONTROL, WATER, CITRUS, CHARCOAL, SUR, TID, RIN, LOCAL, REVI, EZY, VOX	1069-1070	Primary amine, CN stretch	1090-1020	[36]
CONTROL, WATER, CITRUS, CHARCOAL, RIN, LOCAL, REVI, COMF	1016-1017	Phosphate ion/Silicate ion/Aliphatic phosphates (P-O-C stretch)	1100-1000, 1100-900, 1050-990	[36]
ALL	997-998	Aliphatic phosphates (P-O-C stretch)/Silicate ion/	1050-990, 1100-900	[36]
ALL	975-976	trans-C-H out-of-plane bend	970-960	[36]
SUR, TID	878-877	CO ₃ (2-)	877	[46]
CONTROL, WATER, CITRUS, CHARCOAL, SUR, RIN, LOCAL, REVI, COMF, EZY, VOX	851-852	not found		
ALL	826-828	bending of a strong C-H aromatic bending group	~826	[47]
ALL	690-697	Thiol or thio ether, CH ₂ -S- (C-S stretch)	710-685	[36]
CITRUS, CHARCOAL	667	Alkyne C-H bend	680-610	[36]
CONTROL, WATER, CITRUS, CHARCOAL, SUR, TID, LOCAL, REVI, EZY, VOX	633-643	Alkyne C-H bend	680-610	[36]
ALL	551-554	Aliphatic iodo compounds, C-I stretch	600-500	[36]
ALL	420-428	not found		

In the FTIR analysis of Control *Pat* and treated *Pat*, it was found that Control *Pat*'s Amide I absorption (table 4.9) was between 1698 cm⁻¹ and 1699 cm⁻¹ (C=O stretching) [74]. At 1514 cm⁻¹ (CN stretching and NH bending), Amide II was displayed [40]. Amide III bands were between 1258 cm⁻¹ and 1229 cm⁻¹ [36]. At 3282 cm⁻¹, (table 4.9) a prominent and intense amide A band was seen, indicating NH bending. In the cases of WATER and REVI, where the formation of the N-O bond can be found at 1532 cm⁻¹, the first change in the peak was noticed [39]. For CONTROL, SUR, TID, RIN, LOCAL, and REVI, bending vibration of alkanes/organic phosphates (P=O stretch) peaks near 1340 cm⁻¹ were discovered [36, 75]; however, they were not present in the rest of the samples. A similar pattern was seen in the Amide II band at 1258, which was present for CONTROL, RIN, and REVI but not for rest [36]. Primary amine, CN stretch, which vanished in the case of COMF around peak 1069 cm⁻¹, is present in CONTROL, WATER, CITRUS, CHARCOAL, SUR, TID, RIN, LOCAL, REVI, EZY, and VOX (table 4.9) [36].

Phosphate ion peak was found at 1016–1017 cm⁻¹ for CONTROL, WATER, CITRUS, CHARCOAL, RIN, LOCAL, REVI, and COMF [36]. The peak of the following variables—CONTROL, WATER, CITRUS, CHARCOAL, SUR, RIN, LOCAL, REVI, COMF, EZY, VOX—was around 850 cm⁻¹ and vanished in the case of TID (table 4.9). The Alkyne C-H bend of CONTROL, WATER, CITRUS, CHARCOAL, SUR, TID, LOCAL, REVI, EZY, and VOX at 633-643 cm⁻¹ was also present as the second peak for citrus, and charcoal at 667 cm⁻¹ [36].

In the secondary structure of the FTIR peaks (table 4.10), it was found that the β -turn conformation of the hairpin-folded antiparallel β -sheet structure of control *Pat* (1698 cm⁻¹) changed to β -sheet in all the rest treatments (~1703 cm⁻¹) (table 4.10 peak 1) [65]. The peak of control *Pat* at 1642 cm⁻¹ (table 4.10 peak 2) is attributed to random coils/extended chains which, however, got limited to random coils in the case of CITRUS, CHARCOAL, LOCAL, and COMF [52, 53]. The peak shift for SUR, RIN, EZY, and VOX at the same region suggests having alpha-helices. The peak at ~1230cm⁻¹ denoting β -sheet remained unchanged in all the treatments (table 4.10 peak 3) [53]. The peak at 698.3 cm⁻¹ (amide V) denotes the presence of β -sheet, which remained unchanged in all treatments [72].

Table 4.10: Assignments of FTIR peaks to secondary structure for protein of control and washed *Pat* samples

SAMPLE	PEAK 1 (cm ⁻¹)	PEAK 2(cm ⁻¹)	PEAK 3 (cm ⁻¹)
CONTROL	1698 β-turn conformation of the hairpin-folded antiparallel β-sheet structure	1642 random coils/extended chains	1231 β-sheet
WATER	1702 β-sheets	1645 random coils/extended chains	1230 β-sheet
CITRUS	1703 β-sheets	1647 random coils	1229 β-sheet
CHARCOAL	1702 β-sheets	1655 random coils	1230 β-sheet
SUR	1703 β-sheets	1659 alpha-helices	1230 β-sheet
TID	1703 β-sheets	1640 random coils/extended chains	1230 β-sheet
RIN	1704 β-sheets	1657 alpha-helices	1230 β-sheet
LOCAL	1704 β-sheets	1649 random coils	1230 β-sheet
REVI	1704 β-sheets	1640 random coils/extended chains	1231 β-sheet
COMF	1702 β-sheets	1653 random coils	1230 β-sheet
EZY	1703 β-sheets	1657 alpha-helices	1230 β-sheet
VOX	1703 β-sheets	1657 alpha-helices	1230 β-sheet
REFERENCE	[66]	[53,54]	[54]

Proteins and polypeptides show nine amides in their infrared spectra. The amide I band is the most frequently used band among the amide I, II, and III bands for protein conformation [29, 76-80]. The outcome might be attributed to a degree of disorder that is present in the crystalline regions, most likely as a result of weak inter-helical

interactions and greater interhelical spaces brought on by the addition of amino acid residues with large side chains during crystallization [81]. The foundation of the amorphous areas of the fiber involves polar and bulky side-chain amino acids; the reduction in the number of acidic and basic amino acid residues can be associated with the removal of oligomers or small peptides as a result of major chain scission during degumming [81, 82]. By using heat kinetic energy, the molecules of fibroin start to combine with hydrophobic areas and create the building blocks of a β -sheet structure. Localized stress can occur in the chain segments due to the formation of β -sheet nuclei [83, 84]. The chain segments of fibroin can repeatedly stretch and rotate around the primary axis when subjected to local stress, enough water, and time. As a result, hydrogen bonds are rearranged, and β -sheet nuclei are encouraged to grow [84, 85]. According to reports, peptide bond hydrolysis can occur during degumming and may contribute to secondary structural alterations in the *Eri*, *Muga*, and *Pat* [86, 87].

4.2 Effect of curcumin and tannic acid on dyeing of *Eri*, *Muga*, and *Pat* silk fabric

4.2.1 Light fastness and wash fastness of different combinations of dye and mordant

Decolorization and staining issues can occur during laundry if textiles do not have a desired level of color fastness. Many natural dyes have poor color-fastness qualities, which lessens their appeal. It is necessary to apply a fixing treatment in order to increase the color-fastness of natural dyes [88]. The photochemical stability of curcumin is strongly influenced by the solvent, oxygen, and pH [88-90]. Curcumin is not stable when exposed to light [91, 92]. Investigations have been done into the effects of various dye (curcumin) and mordant (tannic acid) mixtures. Numerous elements, including the characteristics of fibers, the molecular makeup of dyes, and the mordanting, affect dye exhaustion, fixation, and levelness of dyeing.

To improve the dye's fastness against water and light, mordant agents are used to fix the dye into the silk [93]. In comparison to samples without a mordant, samples of silk have a deeper color when a mordant is present. In relation to the mordant sequence, various color hues were obtained. The findings suggest that curcumin gives silk fabrics a variety of color hues with excellent affinity when a mordant is present. This could be due to the mordant's affinity for certain colors and fabrics.



Fig 4.13: Scanned image of *Eri* samples treated with 5 light exposure cycles

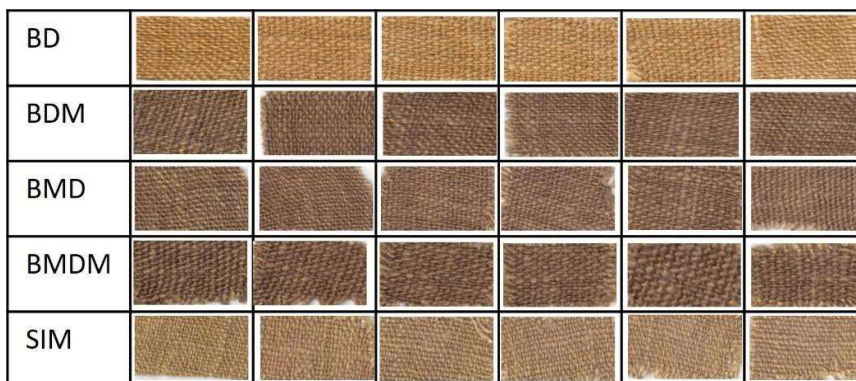


Fig 4.14: Scanned image of *Eri* samples treated with 5 wash cycles

The higher dye uptake value of double mordanting could be attributed to the mordants' increased concentration, which may have bound the most natural dye molecules to the fabric. Silk is made up of units of amino acids [94]. Amino acids with free amino and carboxyl groups are the building blocks of proteins. The dyestuff and silk's amino acid groups form coordinative and intermolecular hydrogen bonds while the silk is being dyed. The type of mordant used has a significant impact on the light fastness of natural dyeing in many instances.

Bright, intense colors with good fastness properties must be found for use in a textile dyeing process. Application in a standardized dyeing process was tested in order to gauge the potential of curcumin dye. The key indicator for a tested natural dye's general introduction was determined to be its light fastness. Curcumin's technical potential in terms of color strength and dyeing fastness was examined. By computing numerical values of the Red-Green-Blue derived from the fabric's surface, quantifiable parameters

for the comparison of the color change were taken into consideration. The quantitative evaluation of color difference used the numerical parameters as raw data.

The results of the dyeing experiments are shown as luminosity, color deviation derived from hue saturation and luminosity coordinates, and fastness characteristics. Fig. 4.15 (a & b) and 4.16 (a & b) for *Eri*, Fig. 4.19 (a & b) and 4.20 (a & b) for *Muga*, and Fig. 4.23 (a & b) and 4.24 (a & b) for *Pat*, respectively, show the fastness properties against sunlight and washing with a combination of BD, BDM, BMD, BMDM, and SIM up to 5 cycles. According to the findings, all mordant samples have significantly improved light fastness. Tannic acid was used to treat silk fabrics as pre- and post-mordant, and it was found that the color quality of these fabrics was superior to that of unmordanted fabrics.

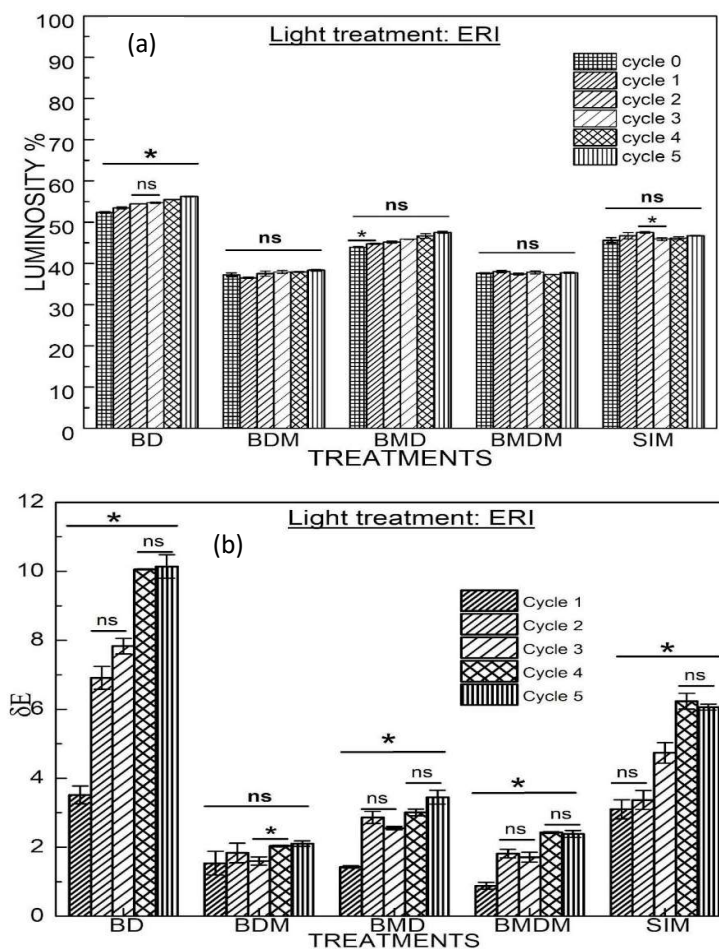


Fig 4.15: a) Luminosity graph of light-treated samples of dyed Eri samples b) δE of light-treated samples with untreated samples (Data are reported as mean \pm SD from three independent experiments; *P < 0.05 compared with the previous cycle of the treatment ; *= significantly different, ns= non-significantly different)

The Luminosity Change in *Eri* samples up to 5 cycles against sunlight, as shown in Fig. 4.15 (a), suggests significant change at a p-value of 0.05 in overall cycles for non-mordant samples but non-significant change for mordanted samples. *Eri*-BD underwent a non-significant change between cycles two and three, whereas *Eri*-SIM underwent a significant change between cycles two and three. After calculating the total color difference Delta E using hue, saturation, and luminosity, it was discovered that post-mordant samples (BDM) did not change significantly during any of the five cycles.

The highest change in *Delta E* has been found in the non-mordant *Eri* sample (BD) for sunlight with colour difference of ~ 3.8 in the first cycle to ~ 10 in the 4th-5th

Physico-chemical, Antibacterial, Antioxidant, Bio Compatibility, and Biodegradation Studies of Washed and Dyed Eri, Muga, and Pat Silk Fabric

cycle, as seen in Fig 4.15 (b). The next deviations have been seen for *Eri*-SIM where the 1st cycle has a value of ~3.2, and the 5th cycle has a difference value of ~6.2. The 4th-5th cycle of all samples has non-significant colour differences suggesting the maximum colour change to occur at the 4th cycle. From the results, it is clear that post-mordant (*Eri*-BDM) and pre-post-mordant (*Eri*-BMDM) show good fastness against sunlight for *Eri* fabrics.

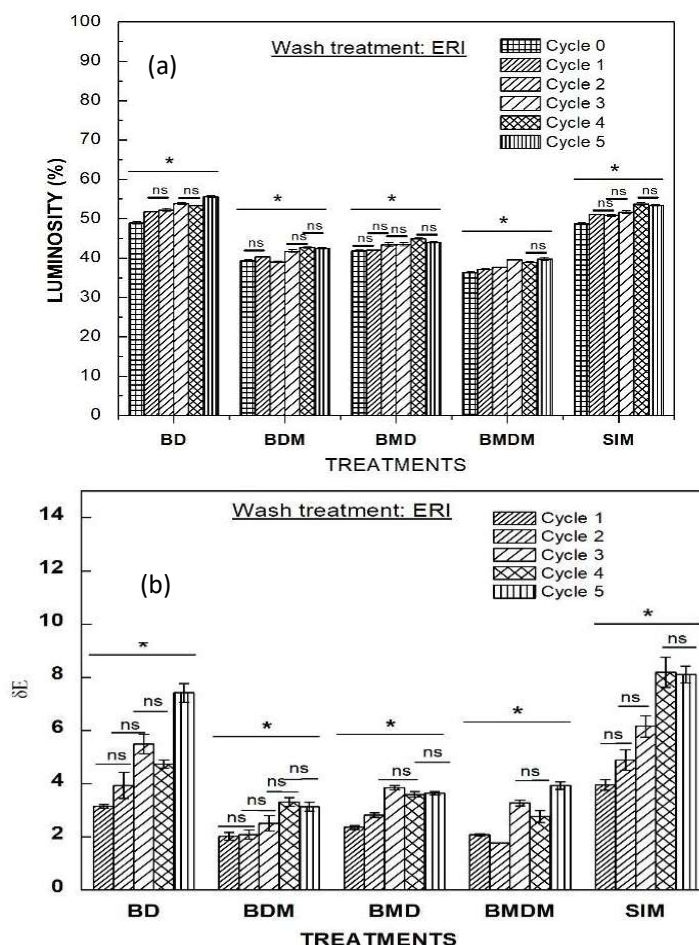


Fig 4.16: a) Luminosity graph of washed samples of dyed *Eri* samples b) ΔE of light treated samples with untreated samples (Data are reported as mean \pm SD from three independent experiments; *P < 0.05 compared with the previous cycle of the treatment ; *= significantly different, ns= non-significantly different)

The luminosity of dyed *Eri* samples that were washed five times is illustrated in fig 4.16 (a). Contrary to light-treated samples, washed samples have significantly different maximum cycles. After the fourth cycle of washing, samples with a mordant

show no discernible change in luminosity. There was a non-significant change in luminosity in many of the adjacent cycles. An overall increase in luminosity can be found in all the washed *Eri* samples as the cycle increases. The highest luminosity is produced by *Eri*-BD, followed by *Eri*-SIM (fig 4.16 (a)).

Eri-BD and *Eri*-SIM exhibit the highest deviation in the Del E (color change) of treated *Eri* as seen in Fig 4.16 (b). In the case of *Eri*-BDM, the overall change up until the fifth cycle appears significant, but if we take the cycles into account with their subsequent cycles, they become insignificant. The unevenness of the woven surface is the cause of the color discrepancy in color appearance that results in a high standard error. The first two wash cycles in the case of *Eri*-BMD show a significant difference in color change, but after the third wash cycle, there are no changes that are worth noting. In many cases, the higher cycle exhibits less color deviation even though there are insignificant changes in cycles. This can be explained by the yellow color turning red as a result of curcumin's reaction with alkaline solutions, which eventually causes changes in subsequent washes. According to the findings, mordant prevents (curcumin) from changing color during an alkali wash, whereas it is easily harmed in the absence of mordant. It was discovered that, in the case of *Eri*-BD Fig 4.15 (b), the light treatment causes a higher level of color change (fading) when compared to the wash treatment (fig 4.16) when comparing the color deviation of the two treatments. The mordant samples were, however, good at retaining their colour in both treatments. The wash fastness of *Eri* in the sequence was found (fig 4.16) to be *Eri*-BDM > *Eri*-BMDM > *Eri*-BMD > *Eri*-BD > *Eri*-SIM. However, *Eri*-BD and *Eri*-SIM were found to have similar wash fastness.

The scanned samples of dyed *Muga* following 5 cycles of light treatments and 5 cycles of washing are depicted in Fig 4.17 and Fig 4.18. In light treatments, there is a clear fading of curcumin toward the fourth and fifth cycles. Graphs of luminosity and Del E for both light treatment and washing are displayed for quantitative analysis of the color changes. Overall significant changes in luminosity, as seen in Fig 4.19 (a) were found in *Muga*-BD, *Muga*-BDM, and *Muga*-BMD; however, *Muga*-BMDM and *Muga*-SIM showed non-significant changes in luminosity. It is interesting to note that in *Muga*-BDM, the overall change is significant but individual cycles are all non-significant when

compared to one another. The samples' general luminosity indicates that change has occurred unevenly.

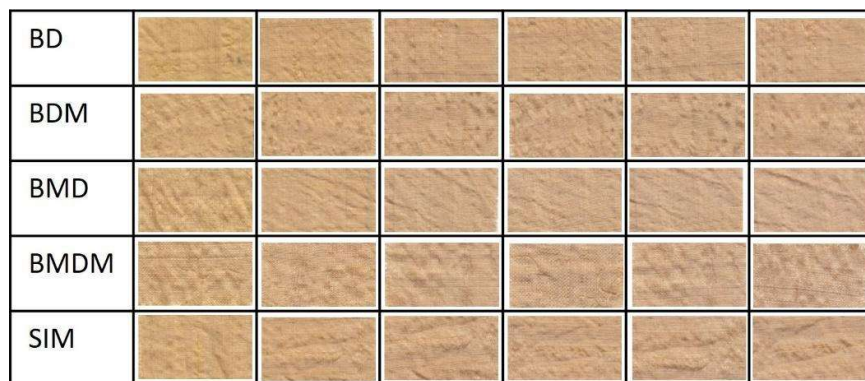


Fig 4.17: Scanned image of Muga samples treated with 5 light exposure cycles



Fig 4.18: Scanned image of Muga samples treated with 5 wash cycles

The Del E graph displays a quantitative change in color while accounting for Hue, Saturation, and Luminosity. The highest deviation del E for *Muga* samples is lower than it is for *Eri* samples. When looking at individual levels, non-significant changes can be seen in the second, third, and fourth *Muga*-BD and *Muga*-BDM of light-treated samples. However, all treatments showed overall results that were significantly different from one another.

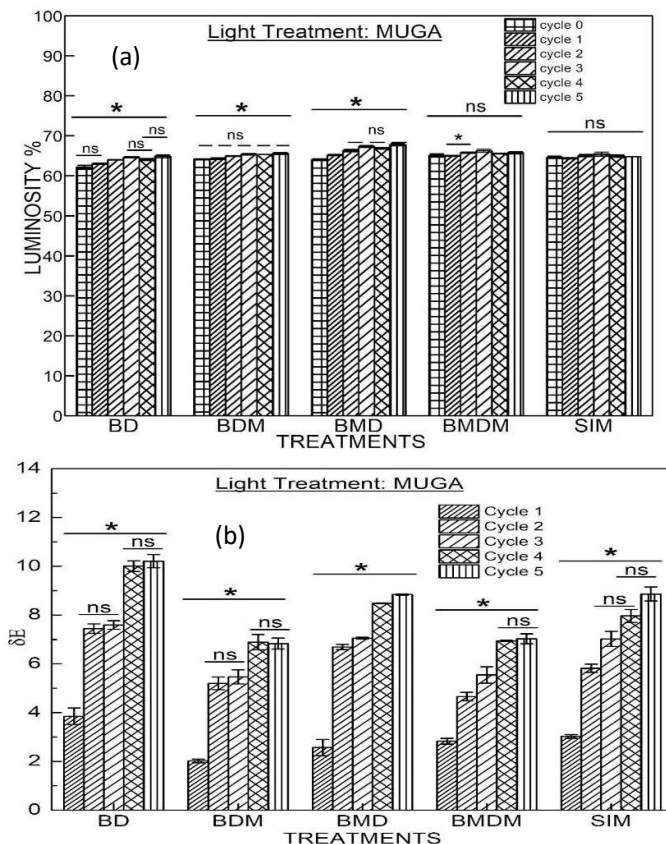


Fig 4.19: a) Luminosity graph of light treated *Muga* samples b) ΔE of light treated samples with untreated samples (Data are reported as mean \pm SD from three independent experiments; *P < 0.05 compared with the previous cycle of the treatment ; *= significantly different, ns= non-significantly different)

For *Muga*-BMDM, the fourth and fifth cycles are non-significant, and for *Muga*-SIM, the third, fourth, and fifth cycles are non-significant as can be seen in Fig 4.19 (b). In all of the samples, the change in ΔE between the first and second cycles is the highest, indicating that the majority of color loss from sunlight occurs in the first and second cycles. From the fourth to the fifth cycles, the change becomes almost stationary. The sequence (fig 4.19) *Muga*-BDM > *Muga*-BMDM > *Muga*-BMD > *Muga*-SIM > *Muga*-BD indicates *Muga*'s lightfastness sequence. The 4th-5th cycle of ΔE exhibits negligible changes, indicating that in the case of *Muga*, the majority of the exposed dye particles on the surface are accessed by sunlight by the 4th cycle.

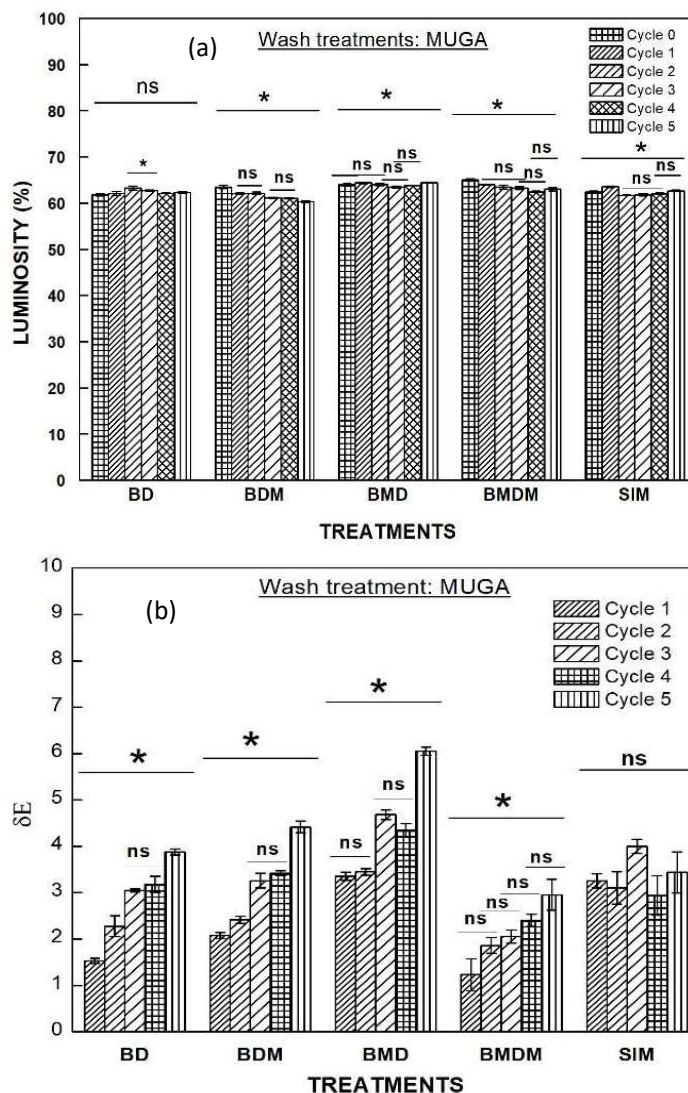


Fig 4.20: a) Luminosity graph of wash *Muga* samples b) δE of wash samples with untreated samples (Data are reported as mean \pm SD from three independent experiments; * $P < 0.05$ compared with the previous cycle of the treatment; * = significantly different, ns = non-significantly different)

The luminosity of washed *Muga* samples shows overall non-significant change in the case of *Muga*-BD whereas significant changes were marked in rest treatments. The overall significance contradicts in individual cases as seen in Fig 4. 20 (a); in *Muga*-BDM, the 2nd-3rd and 4th-5th cycle has a non-significant change in luminosity against wash whereas, for *Muga*-BMD, 0-1st, 1st-2nd, 2nd-3rd and 3rd-4th are a non-significant. In case of *Muga*-BMDM 1st-3rd, 3rd-4th, 4th -5th are non-significant. The *Muga*-SIM samples have 2nd-4th and 4th-5th non-significant. However, the Luminosity graph suggests uneven or

decreasing luminosity in higher washing cycles. *Muga*-BMDM exhibits the best wash fastness properties, as shown in the Del E graph (Fig. 4.20 (b)), with overall significant differences in the 5 cycles but non-significant changes when the adjacent cycles are examined separately. With *Muga*-BMDM, the overall changes are less pronounced. The highest difference is seen in *Muga*-BMD, which can be attributed to a reddish curcumin dye that is attached but may have changed form during washing in *Muga*-BD. The dye molecules in *Muga*-BMDM are not directly accessible, which prevents color change. *Muga*-BMDM is therefore thought to be the best in terms of *Muga* wash fastness.

Figure 4.21 and Fig 4.22 display the scanned copies of *Pat* samples that underwent 5 cycles of sunlight exposure and 5 cycles of washing. It is clear from the scanned images how curcumin's yellow color fades from *Pat* fabric. If we measure qualitatively, *Pat*-BD has the greatest color fading, followed by *Pat*-SIM. Almost all treatments result in some degree of fading. More than just fading is visible when the number of wash cycles is taken into account. If the fastness of sunlight and wash are compared, it is evident that, in the case of *Pat*, the fastness of light is significantly lower than wash. The quantitative analysis helps to clarify the changes occurring in the treatments. Wash scanned images show an uneven formation of red color, which may be caused by dye concentration in particular fabric areas. However, the unevenness is absent from longer wash cycles. Del E, which also takes hue into account, makes it simple to calculate the change in color. As a result, the overall change in color will reveal the actual departure of each dyed sample from its original color. The effective dye absorption and the ease with which mordant-dye complexes can form with silk can both contribute to an increase in the darkness of the shades on the fabrics [95].



Fig 4.21: Scanned image of Pat samples treated with 5 cycles of Sunlight



Fig 4.22: Scanned image of Pat samples treated with 5 wash cycles

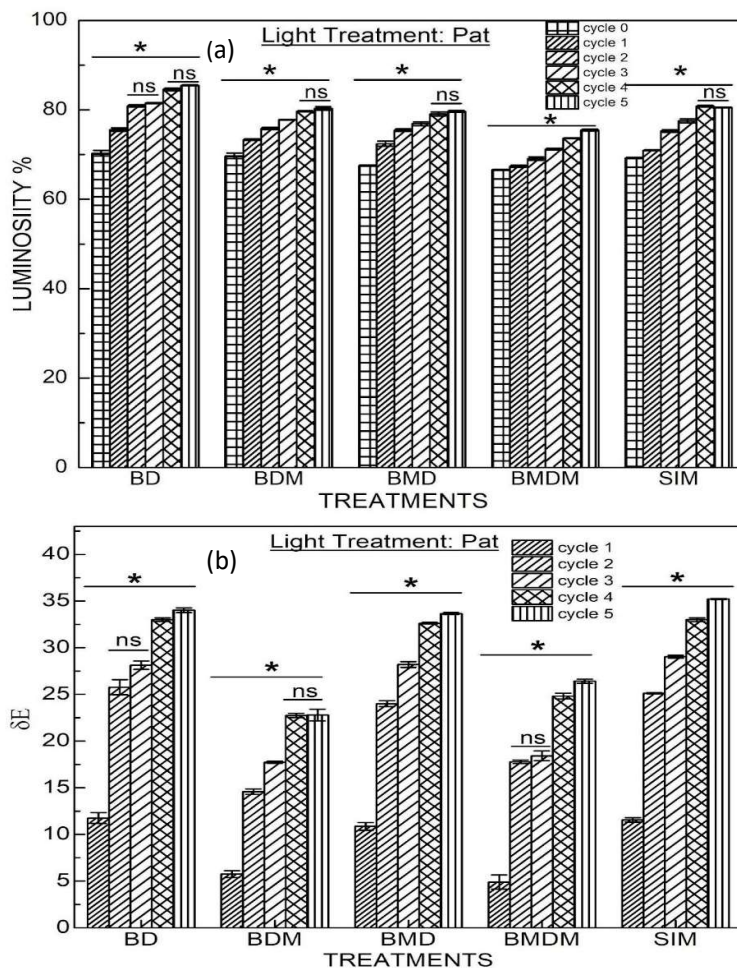


Fig 4.23: a) Luminosity graph of light treated *Pat* samples b) δE of light treated samples with untreated samples (Data are reported as mean \pm SD from three independent experiments; * $P < 0.05$ compared with previous cycle of the treatment ; *= significantly different, ns= non-significantly different)

Due to its light color, *Pat* has the highest Luminosity value when compared to *Eri* and *Muga*. The amount of relative black or white that is combined with a specific hue is measured as luminosity or lightness [96]. In contrast to black mix, which creates shades that reduce luminosity, white mix creates tints that increase luminosity. Luminosity values of *Pat* samples that have been exposed to sunlight are displayed in the graph in Fig 4.23 (a). When compared to the rest, *Pat*-BMDM exhibits the lowest luminosity values, while the other treatments exhibit similar changes. Each cycle's gradual increase in luminosity suggests that fading occurs consistently throughout. The lack of significance in the luminosity% (fig 4.23 (a)) between the 4th and 5th cycles in *Pat*-BD, *Pat*-BDM, *Pat*-BMD, and *Pat*-SIM suggests that the 4th cycle has already attacked the

majority of the dye that can be exposed to sunlight. The colour change determined by Del E is highest in *Pat* displayed in Fig 4.23 (b). The overall color deviation for *Pat*-BD, *Pat*-BMD, and *Pat*-SIM is comparable to their untreated sample (fig 4.23 (b)). Comparatively lower deviations are found in *Pat*-BDM and *Pat*-BMDM. We can infer from the findings that BDM and BMDM are effective against sunlight fastness for *Pat* samples.

The samples of *Pats* that have been subjected to washing exhibit a noticeable change. For the luminosity values, it can be said that while there are numerous non-significant changes within the cycles, the overall change in one treatment is significantly different as seen in Fig 4.24 (a). Wash-treated samples do not gradually become more luminescent over time as light treatments do because of the red color formation that adds shade. Due to the red color formation that adds shade, wash-treated samples do not increase in luminosity gradually as light treatments do. Fig 4.24 (b) presents the Del E's findings. As seen, *Pat*-BD exhibits a typical, steady increase in Del E, whereas *Pat*-BMD and *Pat*-SIM exhibit a non-uniform deviation. A similar situation has also been observed in the case of *Pat*-BMDM, however, the change is insignificant. This non-uniform deviation can be attributed to the reaction of the alkali wash with the available curcumin dye on the surface, which eventually fades, thus decreasing the deviation in the next cycle.

Physico-chemical, Antibacterial, Antioxidant, Bio Compatibility, and Biodegradation Studies of Washed and Dyed Eri, Muga, and Pat Silk Fabric

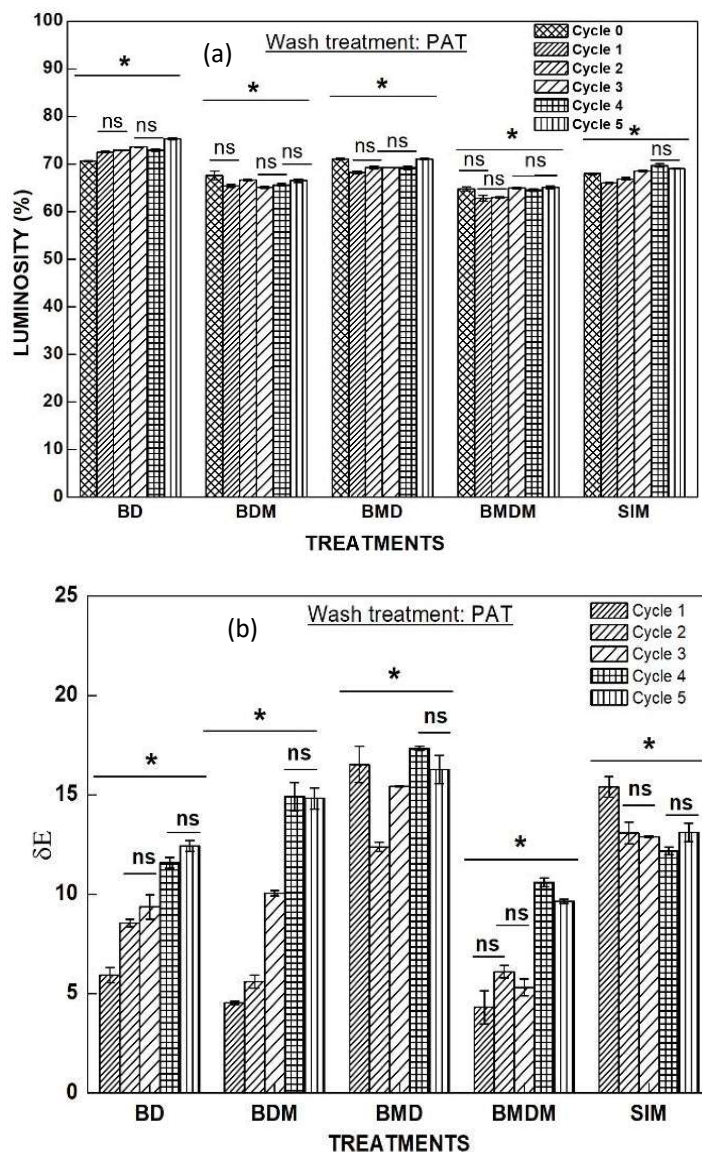


Fig 4.24: a) Luminosity graph of washed *Pat* samples b) δE of washed *Pat* samples with untreated samples (Data are reported as mean \pm SD from three independent experiments; *P < 0.05 compared with previous cycle of the treatment; *= significantly different, ns= non-significantly different)

Fixing agents, as we all know, have the ability to increase the fastness of dyed fabrics by creating intermolecular forces. The separation provided by auxiliaries appears to affect the color characteristics of dyeing, irrespective of the targeted action in dye molecules or among dyes and fibers [88, 97, 98]. In addition to offering particular colors, mordants also enhance the characteristics of color fastness [95]. With regard to the type of mordants, various color shades were obtained [95]. Compared to the best synthetic

dyes, most natural dyes have poor stability. Consequently, mordant dyes make up a large portion of natural dyes. Wash and light fastness of the color are significantly influenced by the nature and concentration of mordants [95]. Increased dye-fibre bonds and decreased dye molecule surface activity may be the causes of the improved light fastness of dyed fabrics [99]. Curcumin desorption from the fabric occurs during washing, which results in an obvious change in color depth [88]. Desorption is inhibited in the presence of a mordant, but the bounded curcumin reacts with an alkaline wash to change color. Silk fibers have low interaction forces with curcumin; this leads to the deposition of curcumin, which is not hydrophilic and continues to aggregate inside the empty space between silk fibers. The silk fabric dyed with curcumin and without the use of fixing treatment displayed unsatisfactory wash-fastness for staining [88, 100]. Many researchers have attempted to identify the woven fabric parameters by image analysis with the advancement of computer technology, which has further simplified the research.

4.2.2 Possible bond formation between Curcumin (dye), tannic acid (mordant) and Silk

As it has been found that post-mordant samples have better fastness properties compared to pre-mordant or un-mordanted samples possible bond formation taking place has been proposed. Considering the hydrogen bonding between tannins and protein described in Lincoln Taiz & Eduardo Zeiger in Plant Physiology [101], the protein-curcumin reaction and curcumin-tannic acid reactions by Habib et. al (2022) [102], and forms of curcumin and bonding sites described by Gupta et. al (2011) [103], possible curcumin reaction with silk, the possible reaction of the pre-mordanting and possible reaction of post-mordanting have been proposed. It has been mentioned that the functional groups on curcumin found suitable for interaction with other macromolecules include the α , β -unsaturated β -diketone moiety, carbonyl and enolic groups of the β -diketone moiety, methoxy, and phenolic hydroxyl groups, and the phenyl rings. The Michael acceptor, Methoxy, and Hydroxy group of the keto form of curcumin has been adapted from Gupta et al., as can be seen in Fig 4.25. In the absence of a mordant, curcumin might bind with the hydroxy group of the keto form which is similar to the proposed mechanism of tannin and protein interaction. The easy removal of curcumin in the absence of mordant gives the idea of weak bond formation and hence, instead of a covalent bond, a hydrogen bond

Physico-chemical, Antibacterial, Antioxidant, Bio Compatibility, and Biodegradation Studies of Washed and Dyed Eri, Muga, and Pat Silk Fabric

might have taken place as depicted in fig. 25. According to Zhou et al. (2015) the affinity of curcumin to silk fiber are predominantly attributed to physical rather than chemical interactions [100].

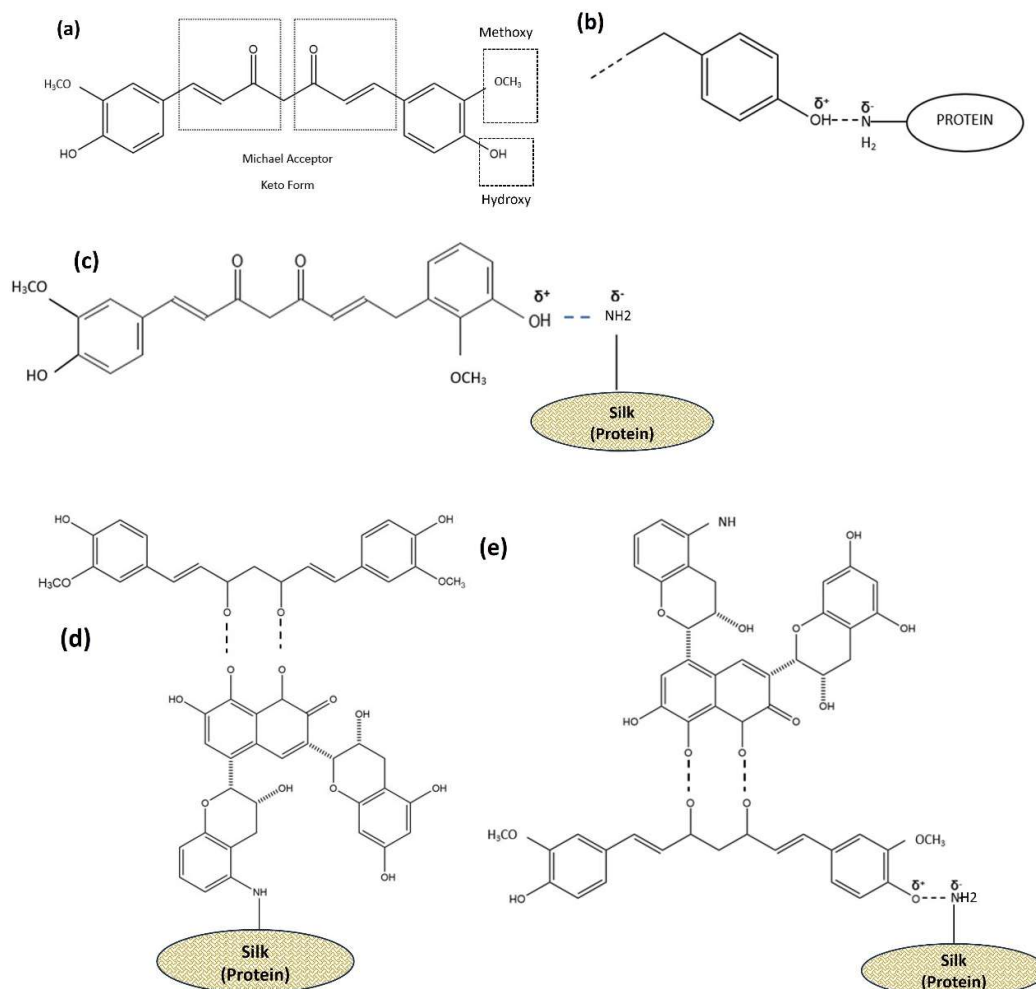


Fig. 4.25 a) The molecular structures of curcumin with sites for interactions adapted from Gupta et al. b) Mechanism of tannin-protein interaction proposed by Lincoln Taiz & Eduardo Zeiger c) Possible curcumin-silk (protein) reaction d) Possible pre-mordant (tannic acid) dyeing (curcumin) with silk (protein) e) Possible post-mordant (tannic acid) dyeing (curcumin) with silk (protein)

4.2.3 DPPH scavenging (antioxidant) properties of treated Eri, Muga, and Pat

One of the most vital characteristics of bioactive textiles is their antioxidant capacity and those that can stabilize strong reactive and damaging species like free oxygen radicals are known as radical scavengers. Through the adsorption of antioxidant

compounds, textiles can be given antioxidant activity. Free radicals and reactive oxygen species (ROS) interact with DNA, as is well known. Numerous skin conditions, including carcinogenesis, are caused by DNA-based modifications of the skin. Since silk is frequently worn next to the skin, fabrics with antioxidant properties are highly desired [104]. When used, silk is frequently in direct contact with skin, so it is crucial to create healthy, hygienic, and anti-microbial silk textiles and materials. DPPH antioxidant assay is based on the ability of 2,2-Diphenyl-1-picrylhydrazyl radical (DPPH), a stable free radical, to get colorless with the addition of antioxidants. The absorbance at 517 nm and the apparent deep purple color are both caused by the odd electron that is present in the DPPH radical [95]. When an antioxidant compound donates an electron to DPPH, the DPPH undergoes decolorization, which can be quantified by changes in absorbance. The DPPH assay was used to examine the antioxidant activity of the *Eri*, *Muga*, and *Pat* samples and their treated counterparts. The DPPH scavenging abilities of untreated *Eri* silk and *Eri* silk with various dye and mordant combinations are shown in Fig 4.26.

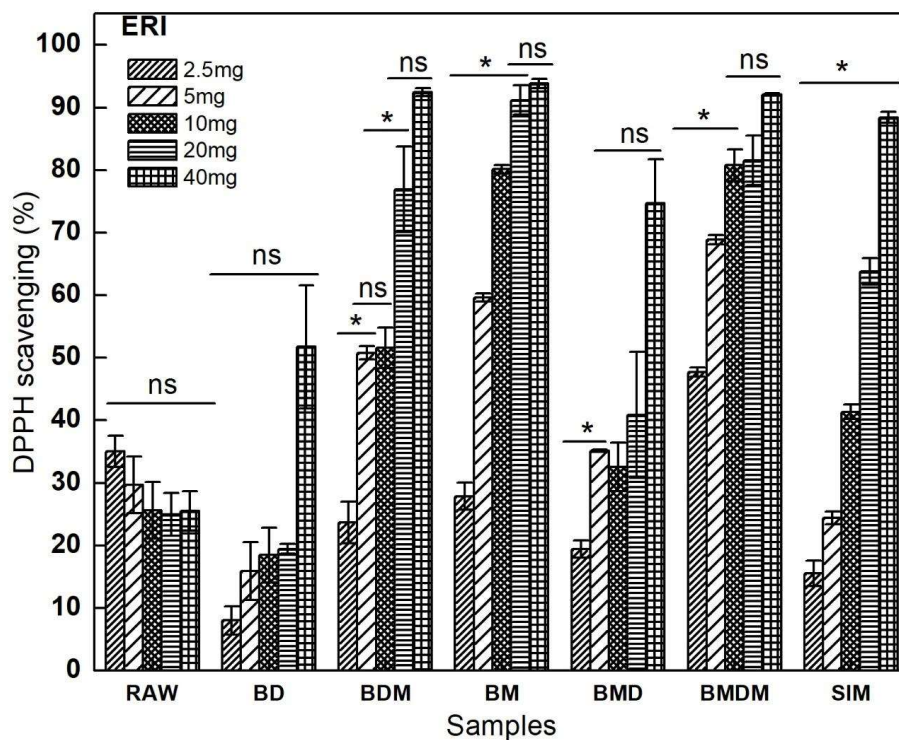


Fig 4.26: DPPH scavenging activity of treated *Eri*; RAW, BD, BDM, BM, BMD, BMDM and SIM with fabric weight 2.5mg, 5mg, 10mg, 20mg and 40 mg (Data are reported as mean \pm SD from three independent experiments; *P < 0.05 compared with adjacent weight result; *= significantly different, ns= non-significantly different)

The samples from *Eri* had the highest percentage of DPPH inhibition when tannic acid was used as a mordant (Fig 4.26). *Eri*-BMDM demonstrated the highest DPPH scavenging activity in the dye and mordant combination at 2.5mg of fabric. The control *Eri* case has a high standard error, indicating that some of its natural color has leaked into the solution and produced a range of results. Overall, the results of the five fabric weights used produced non-significant results, despite the fact that the control (RAW) *Eri* results show a variety of percentages. This demonstrates the inadequate radical scavenging capacity of the original fabrics and implies the release of some natural color to the solution, which contributes to varied outcomes in control *Eri*. Despite the diversity of the overall range, the sample of *Eri*-BD (fig 4.26) displays non-significance, which suggests that *Eri* was not dyed uniformly. *Eri* fibers are thick, as was observed, and physical non-uniform trapping of curcumin dye in the joints may be the cause of the varied standard error bars in *Eri*-BD and their non-significance despite the range being different. Results

at 20mg and 40mg for all treatments (aside from *Eri-SIM*) show negligible changes, indicating 20mg saturation.

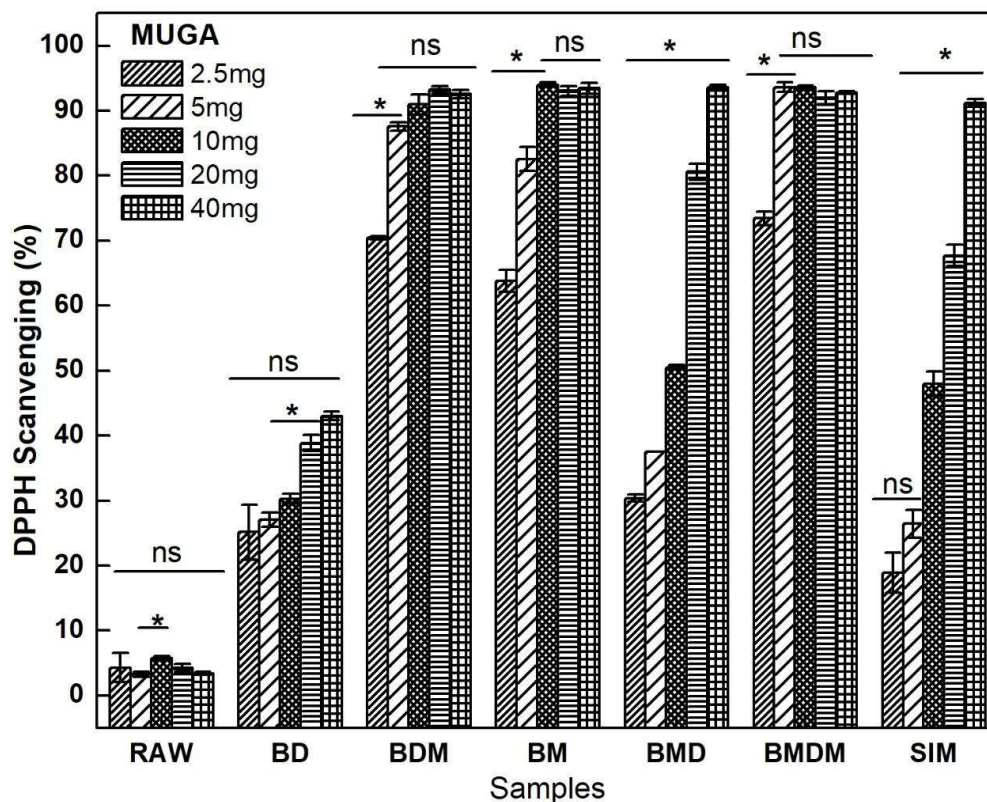


Fig 4.27: DPPH scavenging activity of treated *Muga*; RAW, BD, BDM, BM, BMD, BMDM and SIM with fabric weight 2.5mg, 5mg, 10mg, 20mg and 40 mg (Data are reported as mean \pm SD from three independent experiments; *P < 0.05 compared with adjacent weight result; *= significantly different, ns= non-significantly different)

The control (Raw) *Muga's* antioxidant property is almost non-existent and non-significant until 40 mg, as shown in Fig 4.27, indicating that it has no antioxidant property. Although the antioxidant properties of *Muga*-BD gradually increase, the overall results are found to be non-significant, as was the case with *Eri*. A non-significant antioxidant result of *Muga* fabric between 2.5 mg and 40 mg weight is anticipated in the absence of a mordant due to the non-uniform physical bonding of *Muga*. The non-significant response observed in the *Muga*-BDM and *Muga*-BMDM (fig 4.27) cases ranged from 5 mg to 40 mg, indicating a straining of saturation at 5 mg. With regard to *Muga*-BM, no significant differences were seen at 10 mg, indicating saturation at this level of *muga* fabric weight. The DPPH scavenging activity of *Muga*-BMD and *Muga*-SIM has gradually increased, with the exception of *Muga*-SIM 2.5 and 5 mg (fig 4.27).

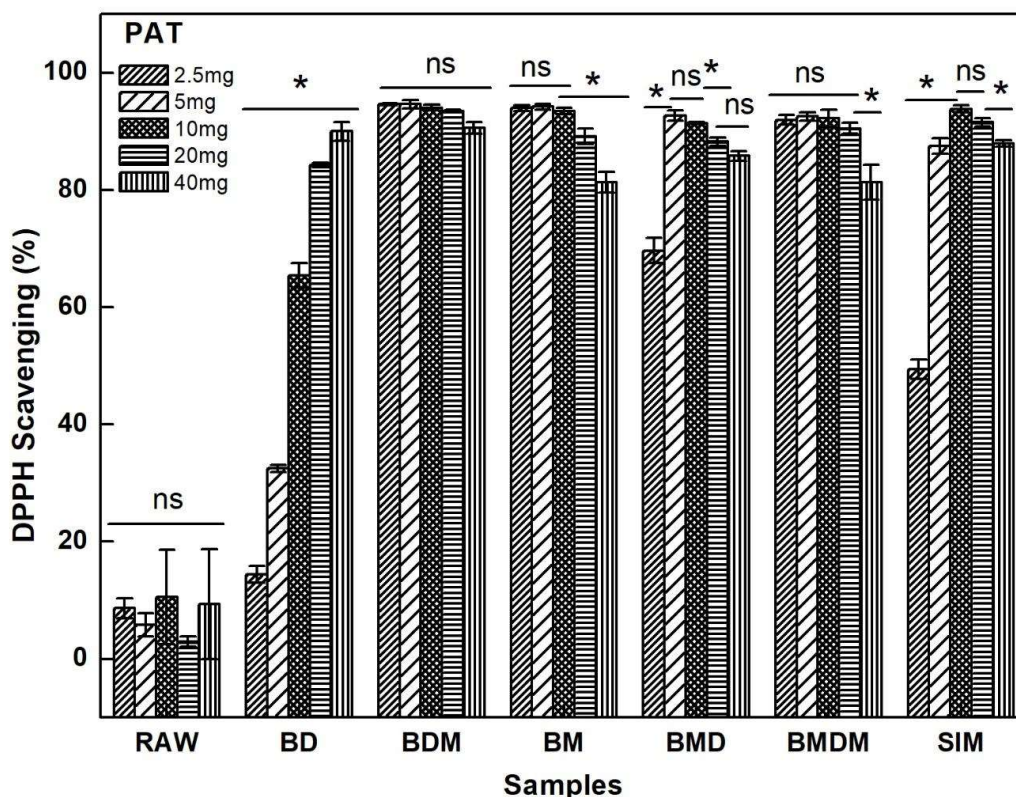


Fig 4.28: DPPH scavenging activity of *Pat*; RAW, BD, BDM, BM, BMD, BMDM and SIM with fabric weight 2.5mg, 5mg, 10mg, 20mg and 40 mg (Data are reported as mean \pm SD from three independent experiments; *P < 0.05 compared with adjacent weight result; *= significantly different, ns= non-significantly different)

Figure 4.28 illustrates the DPPH radical scavenging capacity of uncoloured pat fabric and variously coloured *Pat* fabric. *Pat* the control exhibits very little scavenging activity, and all of the weight yields insignificant results. The scavenging property of *Pat*-BD increases noticeably and gradually. Saturation is at 2.5 mg in the case of *Pat*-BDM, and there has not been a significant change. Higher fabric weight has been associated with a reduction in DPPH scavenging activity for *Pat*-BMD, *Pat*-BM, *Pat*-BMD, *Pat*-BMDM, and *Pat*-SIM; however, for *Pat*-BDM, the overall activity is non-significant (fig 4.28). The activity does gradually decrease with *Pat*-BMD, but there are no appreciable differences between the 20 mg, and there could be some interference from too much tannic acid, which would explain the low scavenging activity or the inconsistent results could be the result of uneven mordant or dyeing.

In general, it can be seen that curcumin and tannic acid both exhibit good scavenging properties when combined with silk. This suggests the antioxidant properties of tannic acid and curcumin. Tannic acid's strong antioxidant properties are attributed to the large number of hydroxyl groups that make up its structure [105]. The small change in absorption intensity after the addition of the raw silk fabric shows that the raw silk fabric lacks the group necessary to undergo a redox reaction with DPPH. The conjugate structure of DPPH can be broken down by the hydroxyl group of tannic acid, which significantly reduces the absorption peak intensity at 517 nm [106]. Tannic acid's polyphenolic composition, relatively hydrophobic "core," and hydrophilic "shell" are thought to be the causes of its antioxidant properties [107]. The hydrophobic interactions between curcumin and the β -sheet regions of silk may allow for binding, and the potent hydrophobic interaction prevented curcumin's leaching from the silk matrix into the nearby medium [108]. Curcumin has two hydrogen-donating phenolic hydroxyl groups located on either side of its structure, which is thought to be the cause of its capacity to scavenge free radicals [104]. Literature supports curcumin to have antioxidant activity by scavenging free radicals [109, 110]. The phenolic hydroxyl groups in curcumin are widely acknowledged to be the primary cause of the antioxidant mechanism of this substance. Antioxidant properties are also significantly influenced by the hydrogen atom transfer from the methylene group [110-112]. According to research by Zhou et al. (2015), the silk fabric dyed with curcumin has a high level of antioxidant activity. However, fixing the treatment is probably going to have an impact on the antioxidant activity of the curcumin-dyed silk [88]. The affinities of silk fiber are primarily associated with physical rather than chemical interactions found in the chemical structures of curcumin [100].

4.2.4 FTIR spectrum of control and the combinations of dyeing and mordant on *Eri*, *Muga*, and *Pat*

The FTIR spectrum of untreated *Eri*, Bleached, and pre-mordanted samples has been shown in Fig 4.29 (a); whereas the bleached, dyed, post-mordant, and simultaneous dyeing and mordanting have been shown in Fig 4.29 (b).

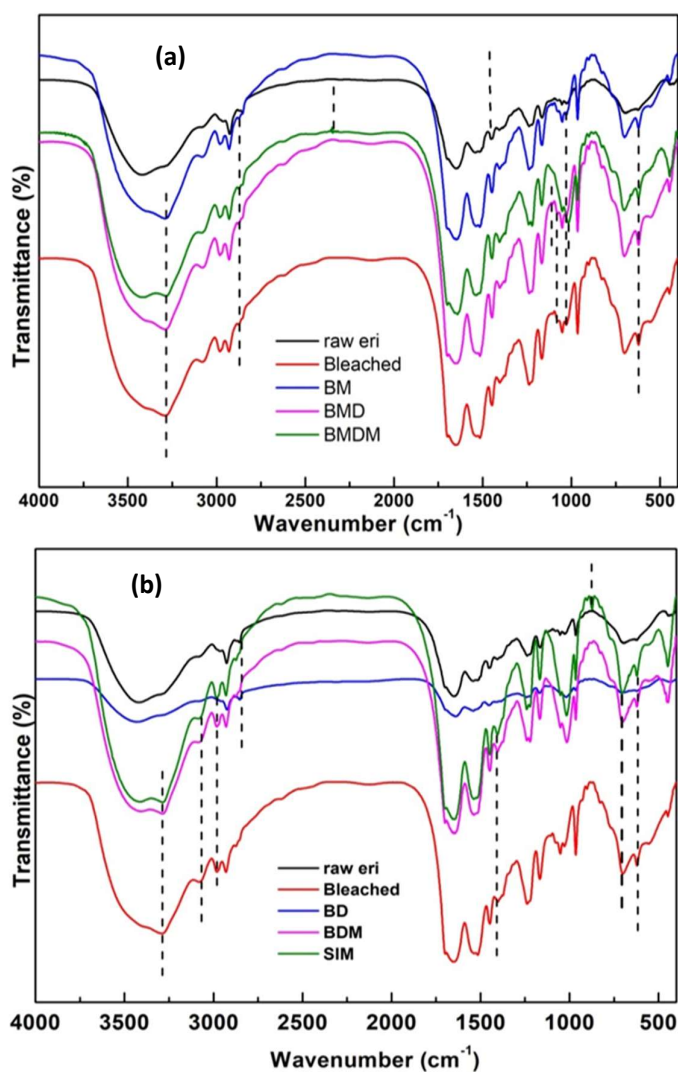


Fig 4.29: FTIR spectra of control and *Eri* treated with a) Bleached and pre mordants, b) Bleached, dyed, post mordant and simultaneous dyeing and mordanting

Physico-chemical, Antibacterial, Antioxidant, Bio Compatibility, and Biodegradation Studies of Washed and Dyed Eri, Muga, and Pat Silk Fabric

Table 4.11: FTIR spectrum of dyeing and mordant combinations of *Eri* fabric

SAMPLES (<i>Eri</i>)	PEAKS (cm ⁻¹)	ASSOCIATION	LITERATURE	REF
RAW, BMDM, BD, SIM	3414-3437	Hydroxy group, H-bonded OH stretch	3570–3200	[36]
B, BM, BMD, BMDM, BDM, SIM	3287-3295	Normal “polymeric” OH stretch	3400–3200	[36]
B, BM, BMD, BMDM, BDM, SIM	3081-3084	Pendant (vinylidene) C-H stretch	3095-3075	[36]
RAW, BD	2953-2967	Methyl (-CH ₃) C-H Asymmetric stretch	2970-2950	[36]
RAW, B, BM, BMD, BMDM, BDM, SIM	2981-2982	C–H stretch	~2982	
ALL	2924-2931	Methylene (-CH ₂ -) C-H Asymmetric stretch	2935-2915	[35]
ALL	2870-2874	Methyl (-CH ₃) C-H Symmetric stretch	2880-2860	[36]
RAW, BD	2854-2855	Methylene (-CH ₂ -) C-H Symmetric stretch	2865-2845	[36]
RAW, B, BM, BMD, BMDM, BDM, SIM	1693-1699	stretching C=O in aromatic carboxylic acids	1680-1740	[37]
RAW, B, BDM	1651-1655	C=O stretching	1650–1750	[38]
BM, BMD, BMDM, BD, SIM	1642-1648	Alkenyl C=C stretch; Primary amine, NH bend; Secondary amine, NH bend	1680–1620; 1650–1590; 1650–1550	[36]
RAW, B, BM, BMDM, BD, BDM, SIM	1527-1543	N-O	1550-1500	[36]
RAW, B, BM, BMD, BMDM, SIM	1514-1517	C-C aromatic compounds	1514-1521	[40]
RAW, B, BM, BMD, BMDM, BD, SIM	1448-1456	Methylene C-H bend (=CH ₂)	1485–1445	[36]
BD	1420	Vinyl C-H in-plane bend	1420–1410	[36]
RAW, B, BM, BMD, BMDM, BD, BDM, SIM	1382-1405	Phenol or tertiary alcohol, OH bend	1410–1310	[36]
ALL	1238-1241	Aromatic ethers,	1230-1270	[36]
RAW, BMDM, BD, BDM, SIM	1219-1221	Stretching vibration of C–O (C–O–C)	~1219	
ALL	1166-1170	C–O stretching and C–H bending	1166 cm ⁻¹	[42]
B, BM, BMD, BD	1100-1114	Silicon; C–C and C–O–C	~1105	[43]
RAW, B, BM, BMD,	1071-1075			
RAW, B, BM, BMD, BMDM, BDM, SIM	1050-1053	Alkyl-substituted ether, C-O stretch (C-O-C)	1150–1050	
RAW, B, BMD, BMDM, BD, BDM, SIM	1016-1030	Phosphate ion; Aliphatic phosphates (P-O-C stretch)	1100–1000; 1050–990	[36]
ALL	963-966	trans-C-H out-of-plane bend	970–960	[36]
BM, BMD, BMDM, BD	924-929	deformational vibrations (C-H) vibration	~930	[45]
B, BM, BMD, BMDM, BD, SIM	901-903			
BM, BMDM, BD, BDM, SIM	870-874	CO ₃ (²⁻)	877	[46]
BM, BMD, BMDM, BDM, SIM	824-827	bending of a strong C–H aromatic bending group	~826	[47]
BD	770	1,2-Disubstitution (ortho); Monosubstitution (phenyl) (C-H)	770–735; 770–730 + 710–690	[36]
ALL	697-708	Alcohol, OH out-of-plane bend; Thiol or thioether, CH ₂ -S- (C-S stretch)	720–590; 710–685	[36]
B, BM, BMD, BMDM, BD, BDM, SIM	618-622	Alkyne C-H bend	680–610	[36]
BD	483	polysulfides (S-S)	500-470	[36]
ALL	438-448	Aryl disulfides (S-S)	500-430	[36]

The Methylene (-CH₂-) C-H Asymmetric stretch at 2924-2931 cm⁻¹, Methyl (-CH₃) C-H Symmetric stretch at 2870-2874 cm⁻¹, Aromatic ethers at 1238-1241, C-O stretching and C-H bending at 1166-1170 cm⁻¹, trans-C-H out-of-plane bend at 963-966 cm⁻¹, Alcohol, OH out-of-plane bend; Thiol or thioether, CH₂-S- (C-S stretch) at 697-708 cm⁻¹ and Aryl disulfides (S-S) at 438-448 cm⁻¹ was found in all *Eri* samples irrespective of treatment [35, 36, 42]. The C-H stretching vibrations of the biopolymer chain's alkane groups caused peaks around 2933 and 2877 cm⁻¹ to occur [36]. Vinyl C-H in-plane bend at 1420 cm⁻¹; 1,2-Disubstitution (ortho); Mono-substitution (phenyl) (C-H) at 770 cm⁻¹ and polysulfides (S-S) has been found specific to *Eri*-BD which wasn't present in other samples [36]. The C=O stretching which was seen in the case of *Eri*-Raw, *Eri*-B, and *Eri*-BDM at 1651-1655 cm⁻¹ got shifted to Alkenyl C=C stretch; Primary amine, NH bend; Secondary amine, NH bend at 1642-1648 cm⁻¹ [37, 38]. It was found that the N-O bond at 1550-1500 cm⁻¹ found in seven samples was missing in the case of *Eri*-BMD [36]. This suggests that pre-mordanting has a different linkage in silk. For *Eri*-BD, the formation of the bond at 1440 cm⁻¹ attributed to vinyl C-H in-plane bend has been reported [36]. According to what was previously stated, the bond at 1443 cm⁻¹ corresponds to the olefinic bending vibrations of the C H bound to the benzene rings of curcumin. The bond's presence at *Eri*-BD and absence in other samples point to a mordant-caused impediment or a change in bond during curcumin's reaction with a mordant. A peak at 770 cm⁻¹ in the case of *Eri*-BD has been observed and is thought to be C-H, 1,2-disubstitution (ortho), or monosubstitution (phenyl) [36].

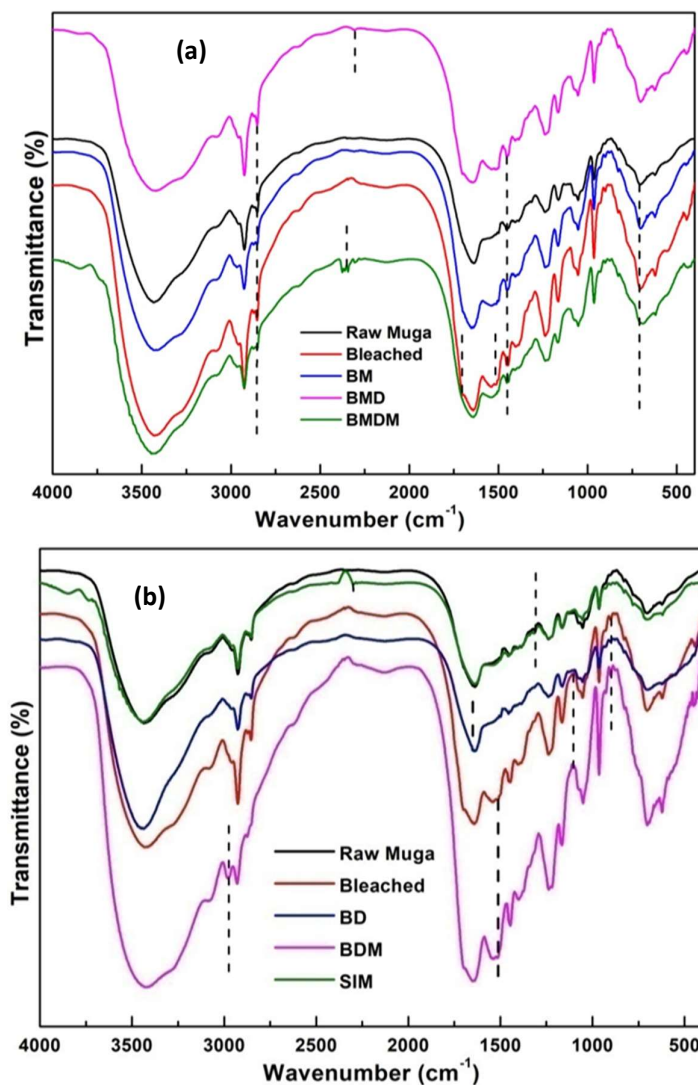


Fig 4.30: FTIR spectra of control and *Muga* treated with a) Bleached and pre mordants, b) Bleached, dyed, post mordant and simultaneous dyeing and mordanting

The FTIR spectrum of untreated *Muga*, bleached and pre-mordanted samples are shown in Fig 4.30 (a); whereas the bleached, post-mordant and simultaneously dyed samples are shown in Fig 4.30 (b).

Physico-chemical, Antibacterial, Antioxidant, Bio Compatibility, and Biodegradation Studies of Washed and Dyed Eri, Muga, and Pat Silk Fabric

Table 4.12: FTIR spectrum of dyeing and mordant combinations of *Muga fabric*

SAMPLES (<i>MUGA</i>)	PEAKS (cm ⁻¹)	ASSOCIATION	LITERATURE	REF
ALL	3424-3447	Hydroxy group, H-bonded OH stretch	3570–3200	[36]
BMD	3078	Pendant (vinylidene) C-H stretch	3095-3075	[36]
RAW,B, BM, BMD, BMDM	2954-2964	Methyl (-CH3) C-H Asymmetric stretch	2970-2950	[36]
BDM	2981	C–H stretch	~2982	
RAW,B, BM, BMD, BMDM, BD, BDM, SIM	2925-2930	Methylene (-CH2-) C-H Asymmetric stretch	2935-2915	[36]
RAW, B, BM, BMD, BMDM, BD, BDM	2869-2880	Methyl (-CH3) C-H Symmetric stretch	2880-2860	[36]
RAW, B, BM, BMD, BMDM, BD, SIM	2851-2853	Methylene (-CH2-) C-H Symmetric stretch	2865-2845	[36]
B, BMD	1697-1698	stretching C=O in aromatic carboxylic acids	1680-1740	[37]
BM, BDM	1651	C=O stretching	1650–1750	[38]
All	1639-1641	Alkenyl C=C stretch; Primary amine, NH bend; Secondary amine, NH bend	1680–1620; 1650–1590; 1650–1550	[36]
B, BM, BMD, BMDM, SIM	1537-1544	N-O	1550-1500	41
BMDM	1517	C-C aromatic compounds	1514-1521	[40]
ALL	1445-1456	Methylene C-H bend (=CH2)	1485–1445	[36]
RAW, BD	1498	Aromatic C=C	~1498	
RAW, B, BM, BMD, BDM, SIM	1384-1390	Phenol or tertiary alcohol, OH bend	1410–1310	[36]
RAW, BM, BMD, BMDM,	1403-1407	Phenol or tertiary alcohol, OH bend	1410–1310	[36]
ALL	1237-1241	Aromatic ethers,	1230-1270	[36]
ALL	1164-1168	C–O stretching and C–H bending	1166 cm ⁻¹	[42]
BMD	1104	Silicon ; C–C and C–O–C	~1105	[43]
RAW, BM, BMD, BMDM, BD, BDM, SIM	1051-1068	Alkyl-substituted ether, C-O stretch (C-O-C); Phosphate ion	1150–1050; 1100–1000	[36]
RAW, B, BM, BMDM, BD, BDM, SIM	964-965	trans-C-H out-of-plane bend	970–960	[36]
RAW, BMD, BMDM, BD, BDM	925 - 930	deformational vibrations (C-H) vibration	~930	[45]
BM, BMD, BMDM, BD, BDM	875-877	CO ₃ (2-)	877	[46]
ALL	825-827	bending of a strong C–H aromatic bending group		[47]
ALL	691-710	Alcohol, OH out-of-plane bend; Thiol or thioether, CH ₂ -S- (C-S stretch)	720–590; 710–685	[36]
ALL	616-663	Alkyne C-H bend	680–610	[36]
B, BM, BMD, BMDM, BD, BDM, SIM	442-448	Aryl disulfides (S-S)	500-430	[36]

The FTIR graph of differently dyed *Muga* is shown in Fig 4.30, and the data peaks are shown in Table 4.12. It has been found that Hydroxy group, H-bonded OH stretch at 3424-3447 cm^{-1} , Alkenyl C=C stretch, Primary amine, NH bend; Secondary amine, NH bend at 1639-1641 cm^{-1} , Methylene C-H bend (=CH₂) at 1445-2456 cm^{-1} , Aromatic ethers at 1237-1241 cm^{-1} , C-O stretching and C-H bending at 1164-1168 cm^{-1} , bending of a strong C-H aromatic bending group at 825-827 cm^{-1} and alkyne C-H bend at 616-663 cm^{-1} have been found in all the treated and untreated samples [36, 40, 42, 47]. The aromatic C=C bond present in *Muga*-Raw silk at $\sim 1498 \text{ cm}^{-1}$ vanished in the case of bleached and other treated samples but was found in *Muga*-BD, indicating the aromatic C=C bond of curcumin in *Muga*-BD (table 4.12). Aryl-disulfides (S-S) were seen in all the treated *Muga* samples that weren't present in untreated samples. The presence of alkyl substituted ether, C-O stretch (C-O-C), or Phosphate ion was present in all treated and untreated samples (table 4.12), however, it was absent for *Muga*-B, indicating the bond has been replaced by tannic acid or curcumin after the application of bleach. Two peaks at the same range for phenol or tertiary alcohol, OH bend has been found in the case of *Muga*-Raw, *Muga*-BM, and *Muga*-BMD; however, for *Muga*-B, *Muga*-BDM, *Muga*-BMDM, and *Muga*-SIM only one peak was found at 1310-1410. No peak was found for *Muga*-BD in this region, this may be due to the phenolic groups of amino acid in the *Muga* silk, which was also seen for tannic acid but with curcumin tertiary alcohol got shield.

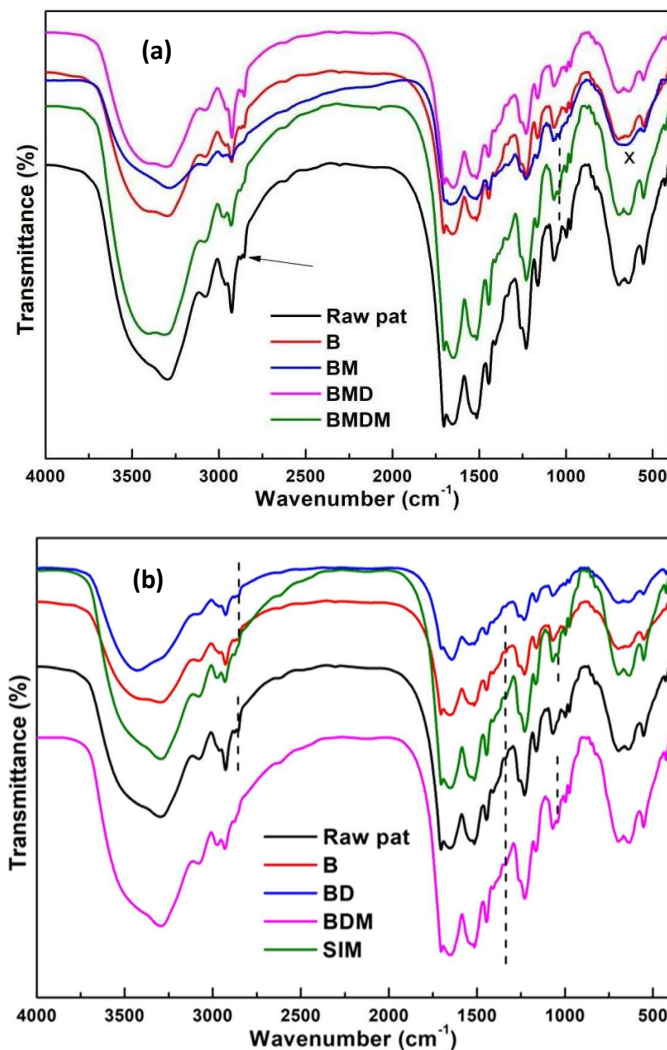


Fig 4.31: FTIR spectra of control and *Pat* treated with a) Bleached and pre mordants, b) Bleached, dyed, post mordant, and simultaneous dyeing and mordanting

The FTIR spectrum of control *Pat*, bleached, and pre-mordant sample has been shown in fig. 4.31 (a) and samples of bleached, dyed, post-mordant samples are shown in Fig 4.31 (b).

According to a previous study [113], curcumin exhibits a broad absorption band at 3350 cm⁻¹ due to phenolic stretching vibration. The other samples' peaks fall within the range for typical "polymeric" OH stretch, so this peak was a shift of *Pat*-BD (table 4.13). Methylene (-CH₂-) C-H Symmetric stretch at 2954-2955 cm⁻¹ was discovered in the cases of *Pat*-raw, *Pat*-B, *Pat*-BD, and *Pat*-BMD, indicating that the addition of tannic

acid results in a change in the bond [36]. The methyl (-CH₃) C-H asymmetric stretch at 2960–2968 cm⁻¹ (table 4.13) was discovered as another such peak using the same samples and *Pat*-BMDM. It is also intriguing that all samples exhibit two peaks at slightly higher wavenumbers that are attributed to methyl (-CH₃) C-H symmetric stretch and methylene (-CH₂-) C-H asymmetric stretch, respectively. It has been stated that peaks at 1631 cm⁻¹ were caused by the carbonyl stretching of the protein's amide-I; however, since the peaks were not observed for *Pat*-raw or *Pat*-B, it can be assumed that the peak is for the carbonyl group of curcumin since curcumin is present in all of the samples [114].

With the exception of *Pat*-Simultaneous (table 4.13), all samples containing curcumin, tannic acid, or both exhibit methylene C-H bending at 1331–1338 cm⁻¹ [36,75]. This suggests that there is no peak for *Pat*-Raw and *Pat*-B, but it is possible that in the case of *Pat*-Simultaneous, curcumin, and tannic acid react before adhering to the silk fabric. Methyl (-CH₃) C-H Asymmetric stretch peak may also be connected to the same cause [36].

Overall, we can infer that the linking is distinct in each of the three silk fabrics when we take into account their associations with tannic acid and curcumin. The peaks of the treated samples were generally similar to those of the untreated samples, though most of the time the peaks displayed shifts in position as a result of the interaction of the silk with either tannic acid or curcumin, or both. According to the FTIR results, there have been no or very minor structural changes in the functional groups of the treated silks.

Physico-chemical, Antibacterial, Antioxidant, Bio Compatibility, and Biodegradation Studies of Washed and Dyed Eri, Muga, and Pat Silk Fabric

Table 4.13: FTIR spectrum of dyeing and mordant combinations of *Pat* fabric

SAMPLES (<i>Pat</i>)	PEAKS (cm ⁻¹)	ASSOCIATION	LITERATURE	REF
	BD 3436	Hydroxy group, H-bonded OH stretch	3570–3200	[36]
RAW, B, BM, BMD, BMDM, BDM, SIM	3291-3308	Normal “polymeric” OH stretch	3400–3200	[36]
	ALL 3071-3084	Pendant (vinylidene) C-H stretch	3095-3075	[36]
RAW, B, BMD, BMDM, BD	2960-2968	Methyl (-CH ₃) C-H Asymmetric stretch	2970-2950	[36]
BM, BDM, SIM	2976-2979	C–H stretch	~2982	
	ALL 2927-2933	Methylene (-CH ₂ -) C-H Asymmetric stretch	2935-2915	[36]
	ALL 2869-2877	Methyl (-CH ₃) C-H Symmetric stretch	2880-2860	[36]
RAW, B, BMD, BD	2854-2855	Methylene (-CH ₂ -) C-H Symmetric stretch	2865-2845	[36]
	ALL 1698-1704	stretching C=O in aromatic carboxylic acids	1680-1740	[37]
RAW, B, BM, BMDM, BDM	1652-1665	C=O stretching	1650–1750	[38]
BMD, BD, SIM	1642-1649	Alkenyl C=C stretch; Primary amine, NH bend; Secondary amine, NH bend	1680–1620;1650–1590; 1650–1550	[36]
B, BM, BMD, BMDM, BD	1528-1546	N-O	1550-1500	41
	ALL 1514-1516	C-C aromatic compounds	1514-1521	[40]
	ALL 1445-1447	Methylene C-H bend (=CH ₂)	1485–1445	[36]
	ALL 1404-1408	Phenol or tertiary alcohol, OH bend	1410–1310	[36]
BM, BMD, BMDM, BD, BDM	1331-1338	Methylene C-H bend	1350-1330	[36,75]
B, BM, BMD, BD	1256-1262	Aromatic ethers,	1230-1270	[36]
B, BM, BMD, BD, SIM	1230-1231	Aromatic ethers,	1230-1270	[36]
	ALL 1161-1165	C–O stretching and C–H bending	1166 cm ⁻¹	[42]
RAW, B, BM, BMD, BD, BDM, SIM	1110-1104	Silicon, C–C and C–O–C	~1105	[43]
	ALL 1069-1073	Alkyl-substituted ether, C-O stretch (C-O-C)	1150–1050	[36]
B, BM, BMD, BMDM, BDM, SIM	1017-1043	Phosphate ion	1100–1000; 1050–990	[36]
RAW, B, BMD, BMDM, BD, BDM, SIM	993-997	Aliphatic phosphates	1050-990	[36]
RAW, BM, BMD, BMDM, BD, BDM, SIM	849-854	1,4 DISUBSTITUTION	860-800	[36]
RAW, BM, BMDM, BD, BDM	874-880	CO ₃ (2–)	877	[46]
RAW, B, BMD, BMDM, BD, BDM, SIM	825-827	bending of a strong C–H aromatic bending group	~826	[47]
RAW, B, BMD, BMDM, BD, BDM, SIM	690-699	Alcohol, OH out-of-plane bend; Thioether, CH ₂ -S- (C-S stretch)	or 720–590; 710–685	[36]
B, BM, BMD, BMDM, BD, BDM, SIM	633-670	Alkyne C-H bend	680–610	[36]
	553-555	C=O		[36]

4.3 To study the biocompatibility and biodegradation of *Eri*, *Muga*, and *Pat* silk clothes treated in Objectives 1 & 2.

4.3.1 Optical Scan, microscope, and SEM analysis of degraded Silk samples

Figure 4.32 shows the scanned, optical microscope, and SEM images of the untreated and treated *Eri* samples at 200 X and 2000 X. Soil burial severely and extensively altered the distinctive fiber morphology. The level of damage is different for different treatments. Some damages were already present during treatment, which was seen in changes in appearance. The occurrence of dullness in the *Eri* fabrics is visible in the scanned images. The rigidity of the fibers was lost in all the *Eri* samples. In the case of the untreated (raw) sample of *Eri*, very minimal damage has been seen. However, for *Eri*-Bleached and *Eri*-Traditional, the fiber almost degraded; the rigidity of the fiber can't be seen. The surface seems to be porous. *Eri*-BMD (Fig 4.31) showed comparatively less degradation than *Eri*-B (fig 4.31) but some splitting and fibrillation have been noticed, along with a porous surface at some sites. In the case of *Eri*-BM, the damages aren't on the overall fibers but can be seen only in some specific areas. It has been discovered that not all of the fibers in the case of *Eri*-Detergent (Fig 4.31) degrade uniformly. Some fibers have significant damage, whereas others have minimal damage. For *Eri*-Shampoo, flattening of the majority of the fibers has been found. Occasional splitting has been described by Peacock (1996) to be as 'fine strands' which was also seen [115,116]. The appearance of the inner fibrils and the breakdown of the fibroin's outer layer are thought to be the causes of the striated appearance [115,117]. *Eri* fibers had distinct damage, and soil burial-related degradation was apparent.

Physico-chemical, Antibacterial, Antioxidant, Bio Compatibility, and Biodegradation Studies of Washed and Dyed Eri, Muga, and Pat Silk Fabric

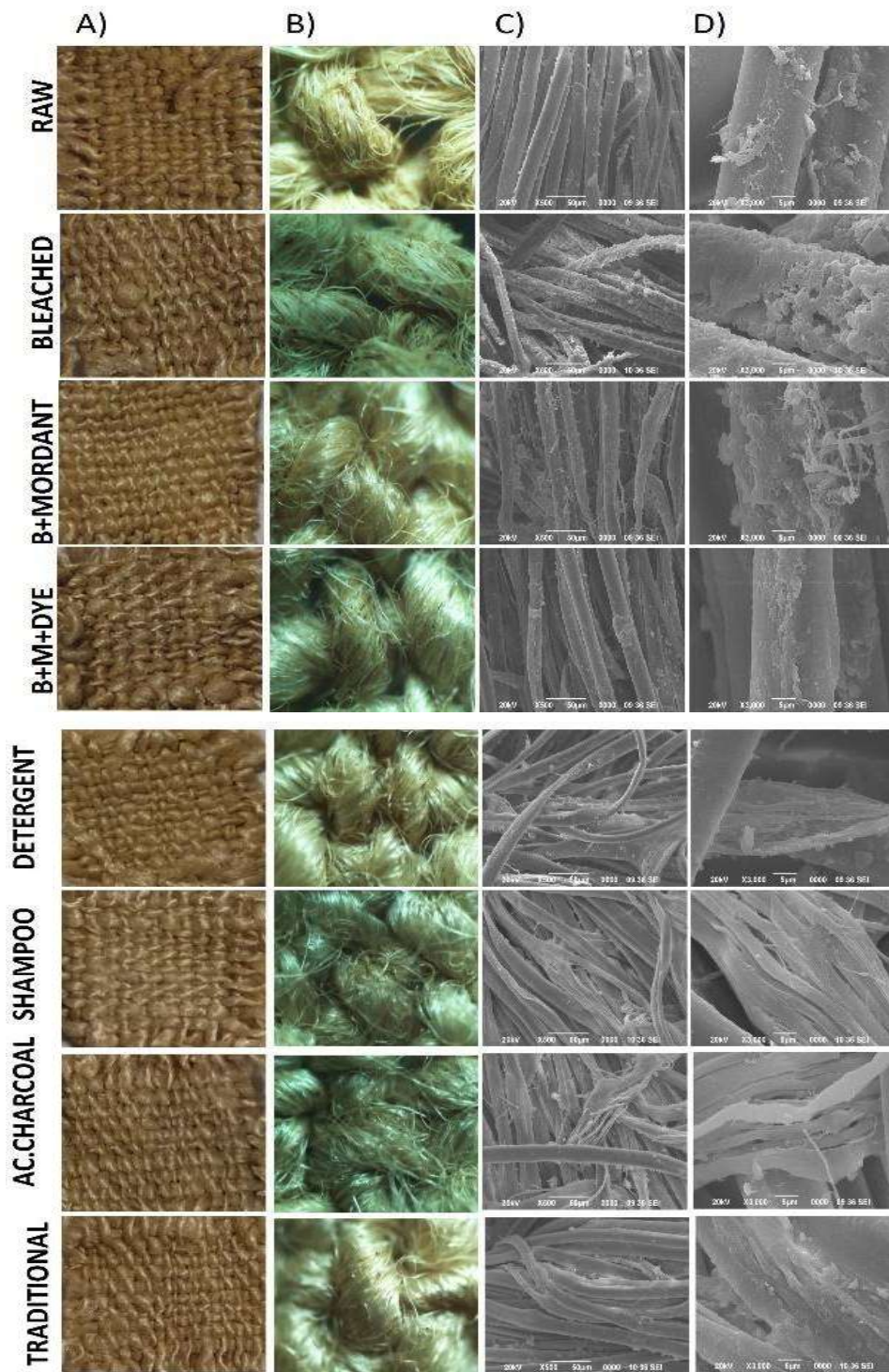


Fig 4.32: Scan, microscope and SEM images of degraded Eri samples

The images of untreated and treated *Muga* samples post-degradation are shown in Fig 4.33. The discoloration of all the samples was evident from the scanned images. The luster of all *Muga* samples was lost. In the case of *Muga*-Raw (fig 4.33), flattening of the fibers has been observed along with degradation with clear debris in specific areas of the fibers. In the case of *Muga*-B, the surface of the fibers exhibits unevenness and roughness. At higher magnification, the surface degradation is clearly visible. The unevenness of all the fibers has been observed in the case of *Muga*-BM (fig 4.33), and on higher magnification, tearing off and damage to the silk fiber has also been seen.

For *Muga*-BMD, it has been observed that the damage is not uniform and is specific to some fibers. In the case of *Muga*-Detergent (fig 4.33), a striated-type formation has been noted, which is clearly visible on the surface of the fibers. The damage appears to be a rough cement wall or orange peel and is almost uniform throughout all of the fibers. The *Muga*-Shampoo sample showed clearly visible deterioration in splits, erosion, longitudinal striations, and exposure of inner fibers. *Muga*-Act. Charcoal shows very minimal damage and no direct degradation on the entire surface of the fiber (fig 4.33). Very little damage at some specific sites of the fiber has been observed. With *Muga*-traditional, specific damage sites can be found, but there is not any general fiber damage. There is surface damage on all of the *Muga* fibers as a result of degradation in the soil. In the scanned images of *Muga*, it was seen that there has been the formation of some flattening-like areas of the fabric at some specific areas in the case of *Muga*-BM, *Muga*-Detergent, *Muga*-Shampoo, and *Muga*-Traditional. *Muga* is known to have stripe-like structures with deep grooves [6], so the damages are evident as these grooves show debris after soil burial treatment indicating degradation does take place in *Muga* fabric [115]. Some globular structures were also discovered in *Muga*-B and *Muga*-BM (fig 4.33) attached to the fiber, which seems to be a component of the fiber.

Physico-chemical, Antibacterial, Antioxidant, Bio Compatibility, and Biodegradation Studies of Washed and Dyed Eri, Muga, and Pat Silk Fabric

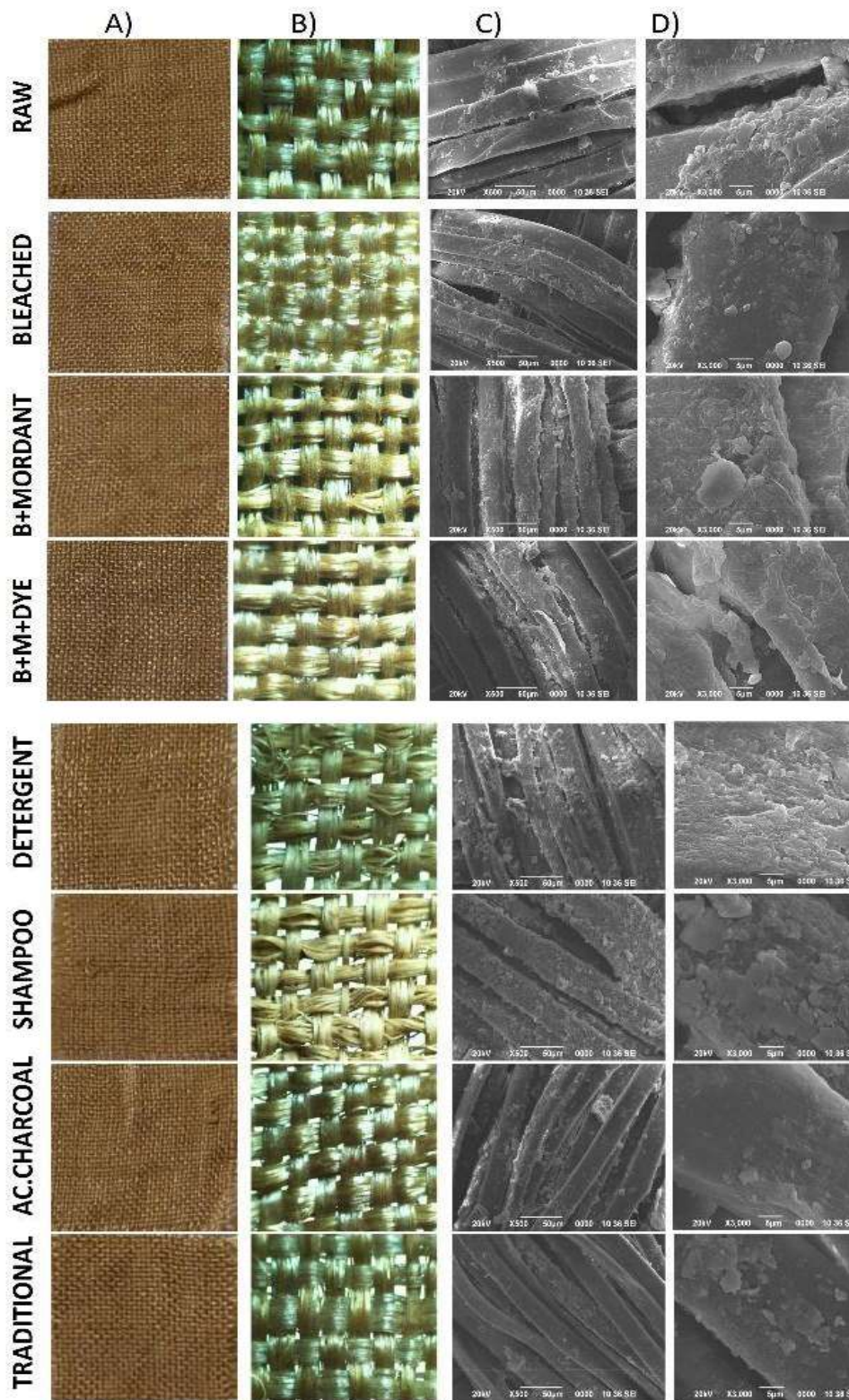


Fig 4.33: Scan, microscope and SEM images of degraded *Muga* samples

Physico-chemical, Antibacterial, Antioxidant, Bio Compatibility, and Biodegradation Studies of Washed and Dyed Eri, Muga, and Pat Silk Fabric

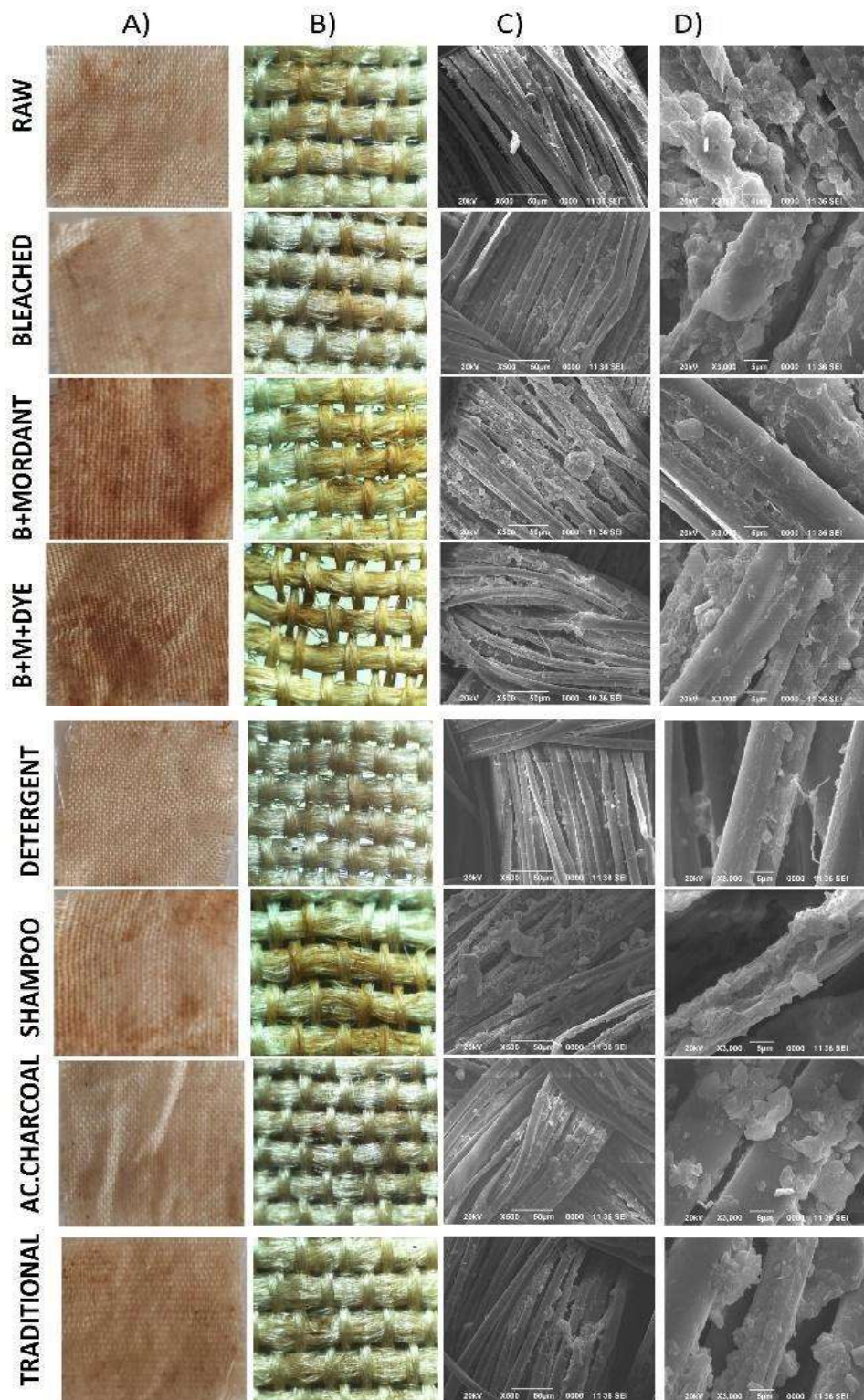


Fig 4.34: Scan, microscopic and SEM images of degraded *pat* samples

The scanned, optical microscope and SEM images of the post-biodegradation of *Pat* are shown in Fig 4.34. The discoloration of the samples is clearly visible in the scanned images. The creation of non-uniform brown zones in the samples suggests a targeted attack by microorganisms in the fabric. The shininess of *Pat* silk has been lost, which can be seen clearly. The degradation can be seen in *Pat*-Raw, with a debris-like presence in the fiber and a globular type on the surface. The scanned image of *Pat*-B shows a comparatively clearer sample; however, in SEM images (fig 4.34), it has been found that selected fibers are damaged where debris like this can be seen in the fibers. *Pat*-BM and *Pat*-BMD show the majority of the area being darkened in the scanned images. The type of damage in both samples seems to be similar in SEM images; however, *Pat*-BMD shows unevenness in almost all fibers, which is lower for *Pat*-BM. *Pat*-Detergent shows very minimal damage. *Pat*-Shampoo shows distinct damage to the fibers, with visible thinning of the fibers (fig 4.34). Formation of grooves, and tearing of fibers can also be noticed in *Pat*-shampoo. *Pat*-Act Charcoal doesn't have any degradation in the entire fiber; however, some globular formations can be seen attached to the surface, whereas the other parts of the fiber seem undamaged. *Pat*-Traditional shows some fibers with minimal damage, whereas some fibers are damaged with debris and globular-like formations on the surface (fig 4.34).

The breakage and debris-like formations in the fibers facilitate the colonization of microorganisms in the fabric. The characteristics of silk biodegradation behavior vary with different enzymes [118]. Most proteolytic enzymes preferentially degrade silk fibroins with low molecular weights and non-compact structures. As a result, the structure and molecular weight of polymers are two key variables influencing the biodegradation process. This shows that the degradation behavior is closely related to the molecular weight and structure of silk biomaterials. It is simple for enzymes to bind to the surface of silks and exhibit hydrolysis behaviors due to the low molecular weight and non-compact structure [119]. The tightly packed supramolecular structure of the protein fibroin, which makes up the degummed silk fibers, is most likely what gives them their high resistance to the effects of microorganisms (142, 143, 144). Silk is categorized as non-degradable in accordance with the US Pharmacopeia's definition. However, it can be inferred from the literature and the experiments conducted here that it is a degradable material. The cause may be related to the fact that a foreign body response typically

mediates silk degradation behavior [119-123]. There have been reports on how microorganisms affect fibers, causing their distinctive morphology to be significantly and extensively altered [115]. It is possible that differences in the rates of degradation of different treatments of the same silk are caused by the incorporation of the chemical group characteristics of the modifying agent into the protein substrate during the chemical modification of silk [124]. When soil degrades, micro- and macroorganisms attack the fibers. Water then seeps into the fibers at these locations, degrading the silk fiber [125]. The slight, localized darkening, foxing, and brown staining that was observed in *Eri*, *Muga*, and *Pat* degradations were also present in other degradations of silk [115, 126]. According to earlier research, after degradation, some fabric sections could be observed in both their intact and degraded states [115, 127]. It has been documented that fibrillation in textile fibers causes the outer layer to erode and split along transverse and longitudinal axes, exposing the inner microfibrils and eventually causing the fibers to completely disintegrate into fibrils [115, 116]. This research also uncovered such occurrences.

4.3.2: Degradation (%) of silk samples post burial on the basis of weight loss

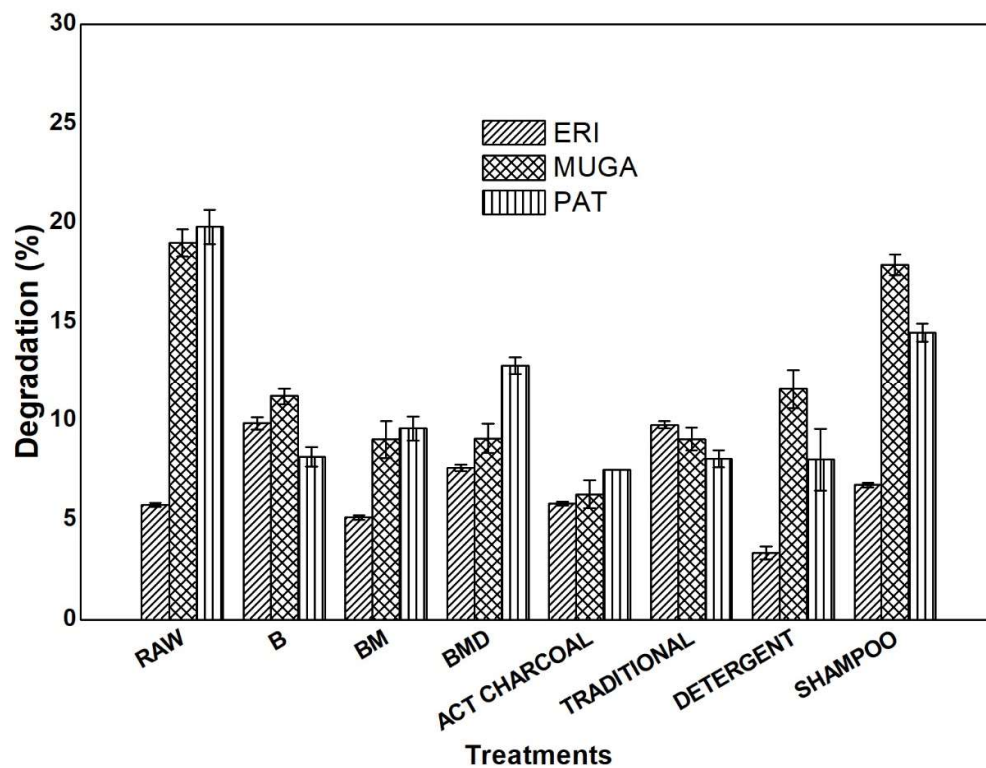


Fig 4.35: Degradation percentage of *Eri*, *Muga*, and *Pat* fabric post soil burial; RAW, B, BM, BMD, Act Charcoal, Traditional, Detergent, Shampoo. (Data are reported as mean \pm SD from three experiments; *P < 0.05 compared with adjacent weight result; the significance has been carried out with each other among same fabric and is reported in-text)

Visual analysis of post-burial silk samples confirmed the degradation loss and the resulting changes in appearance were easily discernible. The resulting loss of weight was calculated, and the results are highlighted in Fig 4.35. In comparison to *Eri* and *Pat*, *Muga* has been found to degrade more quickly. There is no statistically significant difference in the rate of degradation between the *Eri*-Bleached and *Eri*-Traditional of the *Eri* sample. The degradation% in decreasing order is, *Eri*-Bleached > *Eri*-Traditional > *Eri*-BMD > *Eri*-Shampoo > *Eri*-Act. Charcoal > *Eri*-Raw > *Eri*-BM > *Eri*-SEW. The degradation percent between *Eri*-Act. charcoal and *Eri*-Raw is non-significant. The range of degradation in *Eri* is between 3.3 - 7.6 % (fig 4.35).

For *Muga* silk, the degradation pattern was different. *Muga*-Raw and *Muga*-Shampoo showed the highest degradation, but there was no statistically significant

difference between the two. *Muga*-Detergent came afterward. The degradation % in decreasing order is *Muga*-Raw > *Muga*-Shampoo > *Muga*-Detergent > *Muga*-Bleached > *Muga*-Traditional > *Muga*-BM > *Muga*-BMD > *Muga*-Act Charcoal. The range for *Muga* degradation is between 6.2 - 18.99 % (fig 4.35).

For *Pat* silk, *Pat*-Raw showed the highest degradation followed by *Pat*-BMD and *Pat*-Shampoo with the latter having no significant difference between them. The sequence in decreasing order, *Pat*-Raw > *Pat*-Shampoo > *Pat*-BMD > *Pat*-BM > *Pat*-B > *Pat*-traditional > *Pat*-Detergent > *Pat*-Act. Charcoal. The range for *Pat* degradation is between 7.4 - 16.08 % (fig 4.35).

The first indication that fibers, textiles, etc. have begun to degrade biologically is a physical change that is obvious to the unaided eye. Fabrics' integrity and structure also begin to break down as soon as there is a noticeable degradation. The percentage of weight loss is regarded as a direct way to assess the degree of biodegradability. A fabric's higher hydrophilicity makes it more biodegradable, and the resulting sites or breaks make it easier for microorganisms to colonize the fabric [118]. It has been found that the fibroin of *Pat* silk is rich in β -sheet-forming blocks, which are hydrophobic in nature. Protein units consisting of heavy-chain proteins, light-chain proteins, and a p25 glycoprotein in a 6:6:1 M ratio are assembled from these blocks via disulfide bonds and hydrophilic linkers. The *Pat* fibroin is highly crystalline and insoluble in the majority of organic solvents due to the repeated glycine-X amino acid sequence and layers of nonpolar β -sheet forming regimes within the fibroin structure [128-130]. Destabilizing *Pat* silk's fibroin's hydrogen bonds or hydrophobic interactions is, therefore typically difficult.

Due to a higher alanine content, *Eri* silk fibroin is more crystalline and has a higher crystallinity percent compared to *Pat* silk, which may explain why *Eri* silk biodegrades more slowly than *Pat* silk and *Muga* silk [130]. The intricate structure of silk fiber weakens and eventually disintegrates as water seeps in through its cut edges during burial, a process known as biodegradation. It has been discovered that silk's high number of peptide bonds and a significant number of polar hydroxyl side groups which are thought to be from the material's significant serine content, play a role in how well it absorbs water [131].

4.3.3: FTIR result of pre and post-biodegradation of Silk

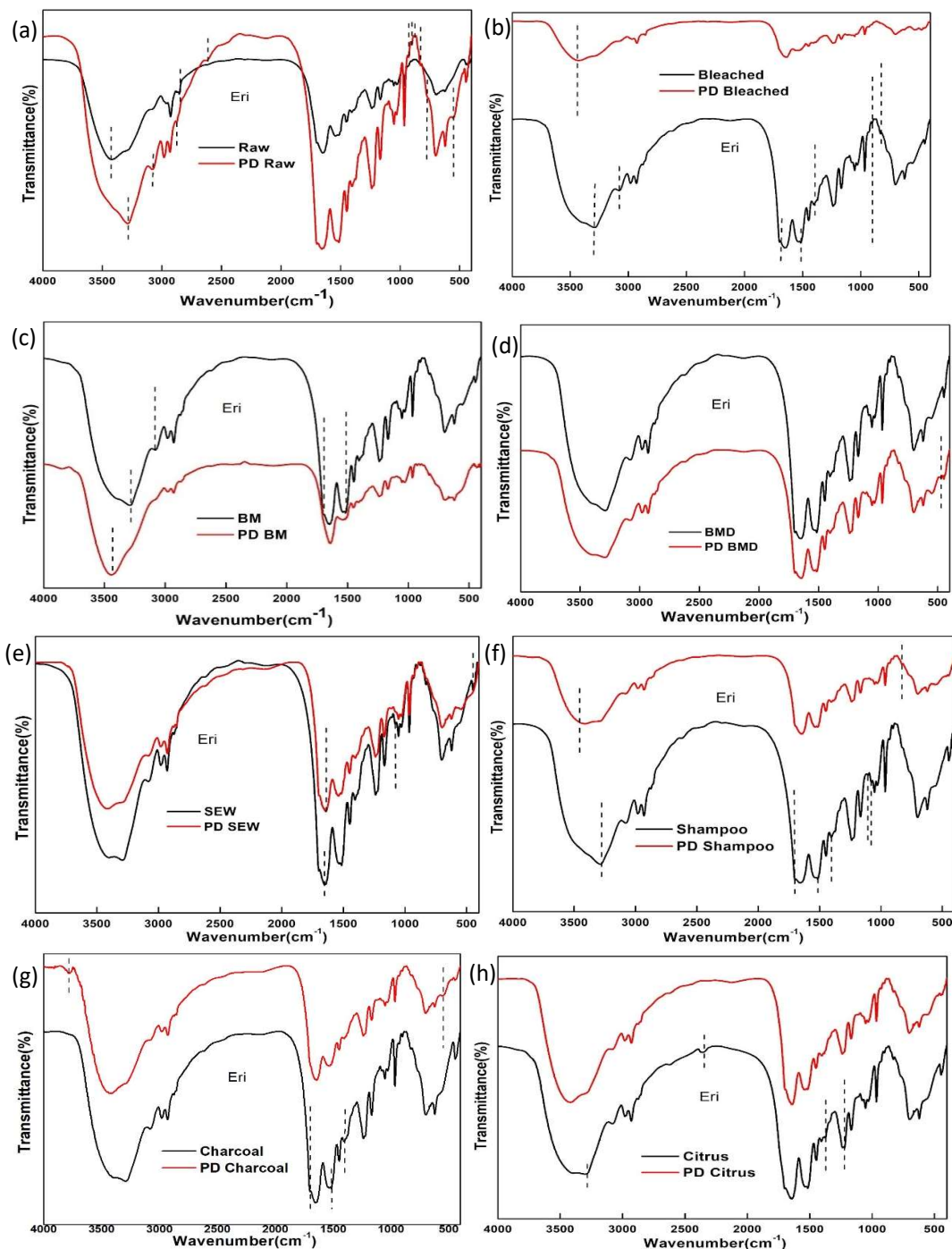


Fig 4.36: Eri fabric pre and Post degradation (a)Raw (b) Bleached (c) Bleached-Mordant (d) Bleached-Mordant-Dye (e) Detergent (SEW) (f) Shampoo (g) Act. Charcoal (h) Traditional (Citrus)

From the FTIR reports of pre and post-*Eri* degradation seen in Fig 4.36, it was found that, in the case of *Eri*-Raw, 2855 cm^{-1} (Methylene (-CH₂-) C-H Symmetric stretch), 1548 cm^{-1} (NH stretching) [114], 1078 cm^{-1} (Cyclic ethers, large rings, C-O stretch (C-O-C) or Primary amine, CN stretch) were the peaks that were absent post biodegradation. Formation of new bonds was also found in *Eri*-Raw (fig 4.36 (a)) post biodegradation, here, 2982 cm^{-1} (C-H stretch; [132], 1372 cm^{-1} (Methyl C-H sym. bend), 929 cm^{-1} , 901 cm^{-1} (Silicate ion), 877 cm^{-1} , 828 cm^{-1} (1,4-Disubstitution (para)) [106], 554 cm^{-1} (Aliphatic iodo compounds, C-I stretch). The peaks at $\sim 877 \text{ cm}^{-1}$ and $\sim 828 \text{ cm}^{-1}$ (Fig 4.36 (a)) are absorption peaks of the C-H bond on the multi-substituted benzene ring. Even though there are peak shifts, FTIR results show no change in secondary structure in *Eri*-Raw pre and post-biodegradation results.

In the case of *Eri*-Bleached fig 4.36 (b), the peaks that got lost after degradation were 1697 cm^{-1} , 1697 cm^{-1} , 1029 cm^{-1} (Primary amine, CN stretch), 902 cm^{-1} (Silicate ion), and 876 cm^{-1} and 829 cm^{-1} both associated with the C-H bond on the multi-substituted benzene ring. There was formation of new bands for *Eri*-Bleached (fig 4.36 (b)), 3418 cm^{-1} (NH stretching deformations) [124], 3432 cm^{-1} (O H stretching) [113], $\sim 2855 \text{ cm}^{-1}$ (C-H stretching vibrations) [114], 1635 cm^{-1} (Alkenyl C=C stretch), 1560 cm^{-1} (Aliphatic nitro compounds), 1551 cm^{-1} (Aliphatic nitro compounds), 1540 cm^{-1} (Aliphatic nitro compounds), 1418 cm^{-1} (Vinyl C-H in-plane bend), 1385 cm^{-1} (CH₃ of either the lipid hydrocarbon chain, and the protein amino acid side chains) [133], 1312 cm^{-1} (Aromatic tertiary amine, CN stretch), 1079 cm^{-1} (Primary amine, CN stretch or phosphate ion), 928 cm^{-1} , 530 cm^{-1} (Aliphatic iodo compounds, C-I stretch), and 475 cm^{-1} (Polysulfides (S-S stretch)). The anti-parallel beta sheets at 1697 cm^{-1} of *Eri*-Bleached were missing in the degraded sample [134].

For *Eri*-BM, (fig 4.36 (c)) peaks at 3282 cm^{-1} (Normal polymeric OH stretch), 1538 cm^{-1} (Aliphatic nitro compounds), 1106 cm^{-1} (Alkyl-substituted ether, C-O stretch (C-O-C) or Cyclic ethers, large rings, C-O stretch (C-O-C)), 1074 cm^{-1} (Alkyl-substituted ether, C-O stretch (C-O-C) or Cyclic ethers, large rings, C-O stretch (C-O-C)), 701 cm^{-1} (Thiol or thioether, CH₂-S- (C-S stretch) or Aryl thioethers, phi-S (C-S stretch) or Disulfides (C-S stretch)) and 556 cm^{-1} (Aliphatic iodo compounds, C-I stretch) of non-degraded were missing after degradation. Additionally, 3446 cm^{-1} (NH stretching

deformations) [45], 928 cm^{-1} (deformational vibrations C-H) [45], and 465 cm^{-1} (Aryl disulfides (S-S stretch)). There have been shifts (fig 4.36 (c)) from 1648 cm^{-1} \rightarrow 1638 cm^{-1} , here, 1648 cm^{-1} is attributed to random coil/ a-helix, whereas, 1638 cm^{-1} is for random coils/extended chains.

In the case of *Eri*-BMD (fig 4.36 (d)), two bands were missing after degradation, 1374 cm^{-1} (Methyl C-H sym. bend) and 1077 cm^{-1} (Alkyl-substituted ether, C-O stretch (C-O-C) or Cyclic ethers, large rings, C-O stretch (C-O-C)). There were four peaks formed after degradation for *Eri*-BMD, 3081 cm^{-1} (Pendant (vinylidene) C-H stretch), 1647 cm^{-1} (Alkenyl C=C stretch), 661 cm^{-1} (Alkyne C-H bend) and 471 cm^{-1} (Aryl disulfides (S-S stretch)). The formation of the peak at 1647 cm^{-1} (Fig 4.36 (d)) is also attributed to random coils.

For *Eri*-Detergents (fig 4.36 (e)), peaks are 3289 cm^{-1} (Normal polymeric OH stretch), 1698 cm^{-1} (C=O stretching) [135], 1106 cm^{-1} (Alkyl-substituted ether, C-O stretch (C-O-C) or Cyclic ethers, large rings, C-O stretch (C-O-C)), 1079 cm^{-1} (Alkyl-substituted ether, C-O stretch (C-O-C) or Cyclic ethers, large rings, C-O stretch (C-O-C)), 829 cm^{-1} (C-H bond on the multi-substituted benzene ring.), and 447 cm^{-1} (Aryl disulfides (S-S stretch)) that were absent after degradation. The formation of peaks (fig 4.36 (e)) were 3414 cm^{-1} (O H stretching) [113], 2854 cm^{-1} (C-H stretching vibrations) [114], 1539 cm^{-1} (Aliphatic nitro compounds), 928 cm^{-1} (deformational vibrations C-H) [135], 662 cm^{-1} (Thiol or thioether, CH₂-S- (C-S stretch)), and 550 cm^{-1} (Aliphatic iodo compounds, C-I stretch). The shifting of 1654 cm^{-1} (Random coil/ a-helix) to 1646 cm^{-1} (random coils/extended chains) took place in the post-biodegradation of *Eri*-Detergent (fig 4.36 (e)).

In *Eri*-Shampoo (fig 4.36 (f)), peaks at 3289 cm^{-1} (Normal polymeric OH stretch), 1697 cm^{-1} (C=O stretching) [135], and 446 cm^{-1} (Aryl disulfides (S-S stretch)) went missing after degradation. New peaks were formed after degradation at 3429 cm^{-1} (O H stretching) [113], 3081 cm^{-1} (Pendant (vinylidene), 1538 cm^{-1} (Aliphatic nitro compounds), 880 cm^{-1} (carbon-ate groups) (fig 4.36 (f)) [136], 828 cm^{-1} (1,4-Disubstitution (para) of C-H) and 582 cm^{-1} (Disulfides (C-S stretch)). Shifting of the peak from 1656 cm^{-1} (Random coil/ a-helix) to 1648 cm^{-1} (random coils/extended chain) and 1373 cm^{-1} (Methyl C-H sym. bend) to 1385 cm^{-1} (bending of secondary amide (-N-H)), was observed [137].

Eri-Act Charcoal (fig 4.36 (g)) has peaked at 3289 cm^{-1} (Normal polymeric OH stretch), 1516 cm^{-1} (C-C aromatic compounds/CN stretching/NH bending), 1080 cm^{-1} (Alkyl-substituted ether, C-O stretch (C-O-C) or Cyclic ethers, large rings, C-O stretch (C-O-C)) and 664 cm^{-1} (Thiol or thioether, CH₂-S- (C-S stretch)) that went missing after degradation. However, the newly formed peaks (fig 4.36 (g)) are 3453 cm^{-1} (O H stretching or Heterocyclic amine, NH stretch) [113], 3411 cm^{-1} , 559 cm^{-1} (Disulfides (C-S stretch)). Peak shift was observed for 1654 cm^{-1} (Random coil/ α -helix) to 1646 cm^{-1} (random coils/extended chain) and from 2875 cm^{-1} (Methyl (-CH₃) C-H Symmetric stretch) to 2858 cm^{-1} (Methylene (-CH₂-) C-H Symmetric stretch).

In the case of *Eri*-Traditional (fig 4.36 (h)), where citrus was used, it was found that peaks at 3082 cm^{-1} (Pendant (vinylidene) C-H stretch), 1699 cm^{-1} (C=O stretching) [135], 1516 cm^{-1} (C-C aromatic compounds/CN stretching/NH bending), 1373 cm^{-1} (Methyl C-H sym. bend), 1221 cm^{-1} (Aromatic phosphates (P-O-C stretch)), and 1077 cm^{-1} (Alkyl-substituted ether, C-O stretch (C-O-C) or Cyclic ethers, large rings, C-O stretch (C-O-C)) were absent after degradation. The newly formed peaks were 3416 cm^{-1} (O H stretching) [113], 1105 cm^{-1} (C-C and C-O-C), 928 cm^{-1} (deformational vibrations C-H) [45], 877 cm^{-1} (carbon-ate groups), 563 cm^{-1} (Aliphatic iodo compounds, C-I stretch), 550 cm^{-1} (Aliphatic iodo compounds, C-I stretch), and 471 cm^{-1} (Aryl disulfides/Polysulfides (S-S stretch)). Peak shifts (fig 4.36 (h)) were observed for 1639 cm^{-1} (Random coil/extended chains/ intramolecular β -sheets) to 1645 cm^{-1} (random coils/extended chains).

The biodegradation of both untreated and treated *Eri* samples can provide clues about the locations of degradation sites. Except for the samples with mordants, all the rest of the samples had a new peak around $550\text{--}582\text{ cm}^{-1}$. The peak at $>3400\text{ cm}^{-1}$ has been observed in the samples, which corresponds to strongly adsorbed and/or bound H₂O during degradation [136]. In the case of *Eri*-Bleached, *Eri*-Detergent, *Eri*-Shampoo, and *Eri*-Citrus absence of peak 1698 cm^{-1} was seen, which is associated with the β -turn conformation of the hairpin-folded antiparallel β -sheet structure. The presence of the peak was also found in *Eri*-Raw and *Eri*-BMD, however, the peak was found to be intact even after biodegradation. The treatments that are applied to silk fibroins result in differences in their secondary structure, which in turn results in differences in how easily they degrade [138].

Physico-chemical, Antibacterial, Antioxidant, Bio Compatibility, and Biodegradation Studies of Washed and Dyed Eri, Muga, and Pat Silk Fabric

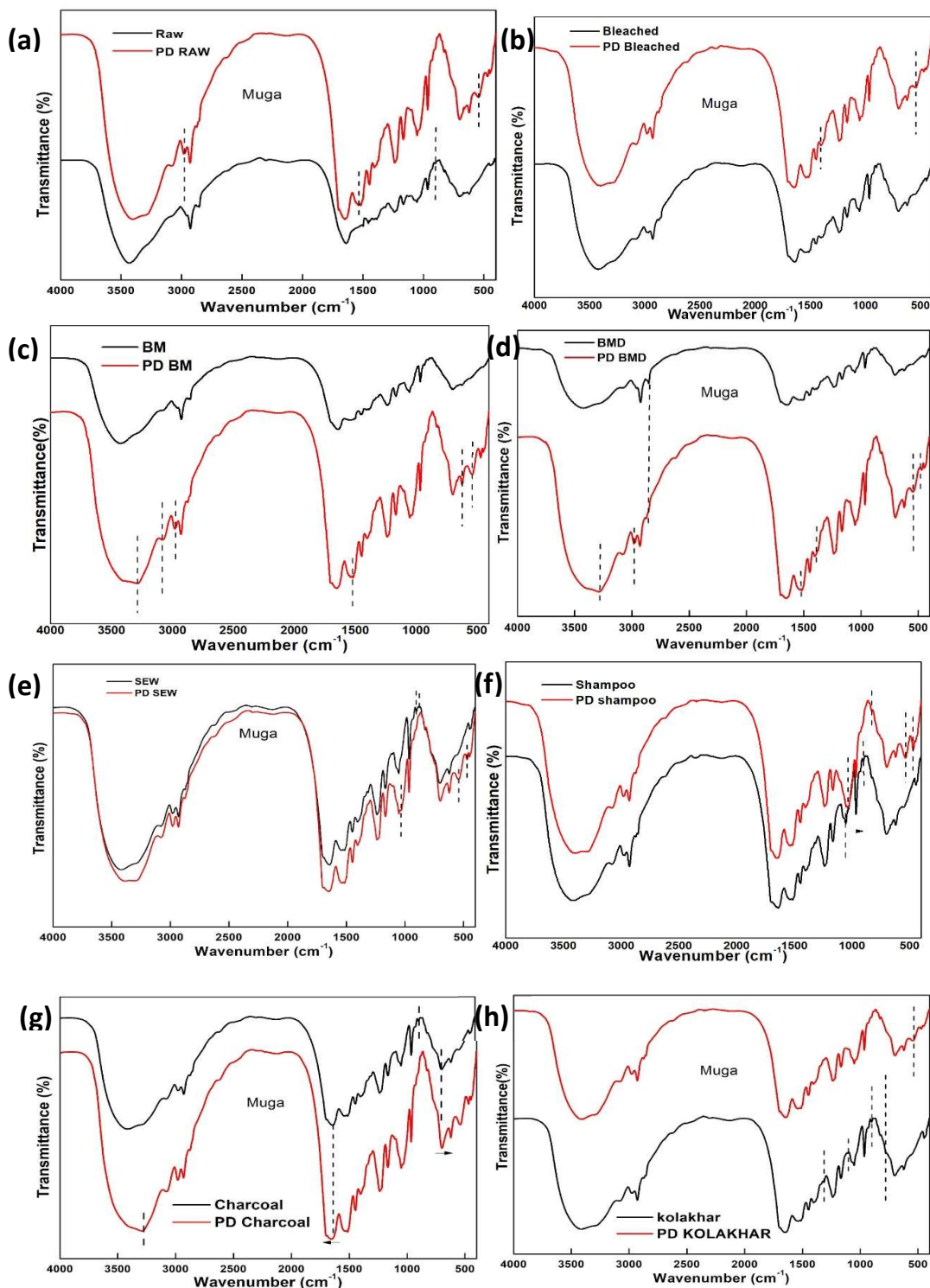


Fig 4.37: *Muga* fabric pre and post degradation (a)Raw (b) Bleached (c) Bleached-Mordant (d) Bleached-Mordant-Dye (e) Detergent (SEW) (f) Shampoo (g) Act. Charcoal (h) Traditional (*kolakhar*)

In Fig 4.37, we can see the pre- and post-biodegradation FTIR graphs of untreated and treated *Muga* samples. In the case of *Muga*-Raw (fig 4.37 (a)), peaks that got lost after degradation are 2855 cm^{-1} (Methylene (-CH₂-) C-H Symmetric stretch), 1498 cm^{-1} (Aromatic ring stretch), 1385 cm^{-1} (CH₃ of either the lipid hydrocarbon chain and the protein amino acid side chains) [133], 1316 cm^{-1} (Phenol or tertiary alcohol, OH bend), 1120 cm^{-1} (Alkyl-substituted ether, or Cyclic ethers, large rings, C-O stretch (C-O-C)) and 903 cm^{-1} (Skeletal C-C vibrations). Whereas the newly formed peaks were 1535 cm^{-1} (NH stretching) [114], 1517 cm^{-1} (C-C aromatic compounds/CN stretching/NH bending), 1105 cm^{-1} (C-C and C-O-C), 928 cm^{-1} (deformational vibrations C-H) [45], 545 cm^{-1} and 471 cm^{-1} (Aryl disulfides/Polysulfides (S-S stretch)). Peak shifts (fig 4.37 (a)) that were observed were 3434 cm^{-1} (Heterocyclic amine, NH stretch) to 3406 cm^{-1} ; 2958 cm^{-1} (Methyl (-CH₃) C-H Asymmetric stretch) to 2980 cm^{-1} ; 1640 cm^{-1} (random coils/extended chain) to 1649 cm^{-1} (random coils) and 1456 cm^{-1} (Methylene C-H bend (=CH₂)) to 1446 cm^{-1} (Methylene C-H bend (=CH₂)).

For *Muga*-Bleached (fig 4.37 (b)), peaks at 3421 cm^{-1} (O H stretching) [113], 1315 cm^{-1} (Phenol or tertiary alcohol, OH bend), 901 cm^{-1} (Skeletal C-C vibrations), 879 cm^{-1} (carbon-ate groups) [136] were absent after degradation. However, new peaks at 3398 cm^{-1} (O-H stretching) [139], 3081 cm^{-1} (Pendant (vinylidene) C-H stretch), 1702 cm^{-1} (Carboxylic acid), 928 cm^{-1} (deformational vibrations C-H) [45], 544 cm^{-1} and 471 cm^{-1} (Aryl disulfides/Polysulfides (S-S stretch)) were found after degradation. The peak shifts that were observed are, 2970 cm^{-1} (Methyl (-CH₃) C-H Asymmetric stretch) to 2980 cm^{-1} ; 1642 cm^{-1} (random coils/extended chains) to 1648 cm^{-1} (random coils/ α -helix) (fig 4.37 (b)).

In the case of *Muga*-BM (fig 4.37 (c)), peaks at 3421 cm^{-1} (O H stretching) [113], 2855 cm^{-1} (Methylene (-CH₂-) C-H Symmetric stretch), 1498 cm^{-1} (Aromatic ring stretch), 1388 cm^{-1} (CH₃ bending) [140], 929 cm^{-1} (deformational vibrations C-H) [45], 902 cm^{-1} (Skeletal C-C vibrations), 875 cm^{-1} (carbon-ate groups) [136] and 704 cm^{-1} (Disulfides (C-S stretch) were absent after degradation. The newly formed peaks were 3289 cm^{-1} (Normal “polymeric” OH stretch), 1517 cm^{-1} (C-C aromatic compounds/CN stretching/NH bending), 828 cm^{-1} (1,4-Disubstitution (para) C-H), 539 cm^{-1} , 409 cm^{-1} and 449 cm^{-1} (Aryl disulfides (S-S stretch)). The peak shifts (fig 4.37 (c)) were seen for

2958 cm^{-1} (Methyl (-CH₃) C-H Asymmetric stretch) to 2981 cm^{-1} ; 1641 cm^{-1} (random coils/extended chains) to 1649 cm^{-1} (random coils/ α -helix); 1455 cm^{-1} (Aromatic ring stretch or Methylene C-H bend (=CH₂)) to 1447 cm^{-1} (Methylene C-H bend (=CH₂)).

In the case of *Muga*-BMD (fig 4.37 (d)), 3414 cm^{-1} (O H stretching) [113], 2853 cm^{-1} (Methylene (-CH₂-) C-H Symmetric stretch), 1643 cm^{-1} (Alkenyl C=C stretch), 1539 cm^{-1} (N-H bending), 1385 cm^{-1} (CH₃ of either the lipid hydrocarbon chain and the protein amino acid side chains) [140], 903 cm^{-1} (Skeletal C-C vibrations), 877 cm^{-1} (carbon-ate groups) [136] and 662 cm^{-1} (Thiol or thioether, CH₂-S- (C-S stretch)). The newly formed bonds are, 3274 cm^{-1} (Normal “polymeric” OH stretch), 1446 cm^{-1} (Methylene C-H bend (=CH₂)), 1238 cm^{-1} (Aromatic ethers,), 1105 cm^{-1} (C-C and C-O-C), 929 cm^{-1} (deformational vibrations C-H) [45], 546 cm^{-1} and 471 cm^{-1} (Aryl disulfides/Polysulfides (S-S stretch)) (fig 4.37 (d)). The peak shifts observed were 2957 cm^{-1} (Methyl (-CH₃) C-H Asymmetric stretch) to 2981 cm^{-1} ; 1454 cm^{-1} (Methylene C-H bend (=CH₂)) to 1446 cm^{-1} (Methylene C-H bend (=CH₂)).

For *Muga*-Detergent (fig 4.37 (e)), the lost peaks during degradation were 3421 cm^{-1} (O H stretching) [113], 1315 cm^{-1} (Phenol or tertiary alcohol, OH bend), 901 cm^{-1} ((Skeletal C-C vibrations)), and 877 cm^{-1} (carbon-ate groups) [136]. The peaks, that were newly formed were, 3081 cm^{-1} (Pendant (vinylidene) C-H stretch), 1538 cm^{-1} (N-H bending), 1033 cm^{-1} (Primary amine, CN stretch), 544 cm^{-1} and 471 cm^{-1} (Aryl disulfides/Polysulfides (S-S stretch)). The observed peak shifts (fig 4.37 (e)) found for *Muga*-Detergent are 1642 cm^{-1} (random coils/extended chains) to 1655 cm^{-1} (Random coil/ α -helix).

In the FTIR results for *Muga*-Shampoo (fig 4.37 (f)), peaks at 3406 cm^{-1} (O H stretching) [113], 2855 cm^{-1} (Methylene (-CH₂-) C-H Symmetric stretch), 2361 cm^{-1} , 1699 cm^{-1} (C=O) [135], 1315 cm^{-1} (Phenol or tertiary alcohol, OH bend), 1105 cm^{-1} (Alkyl-substituted ether,), 929 cm^{-1} (deformational vibrations C-H) [45], 901 cm^{-1} (Skeletal C-C vibrations), 876 cm^{-1} (carbon-ate groups) [136] were not seen after degradation. Peaks at 3390 cm^{-1} (Normal “polymeric” OH stretch), 1034 cm^{-1} (Primary amine, CN stretch), 538 cm^{-1} , and 471 cm^{-1} (Aryl disulfides/Polysulfides (S-S stretch)) were newly formed after degradation. Peak shift was found for 2970 cm^{-1} (Methyl (-CH₃))

C-H Asymmetric stretch) to 2981 cm^{-1} and 1640 cm^{-1} (Random coil/ extended chains) to 1648 cm^{-1} (Random coil/ α -helix).

Muga-Act Charcoal (fig 4.37 (g)) had peaked at 3406 cm^{-1} (O H stretching) [113], 1537 cm^{-1} (N-H bending), 901 cm^{-1} (Skeletal C-C vibrations), and 878 cm^{-1} (carbon-ate groups) [136] that were lost during degradation. The peaks that were formed newly were, 3282 cm^{-1} (Normal “polymeric” OH stretch), 541 cm^{-1} , and 469 cm^{-1} (Aryl disulfides/ (S-S stretch)). The peak shifts that have taken place are 1642 cm^{-1} (random coils/extended chains) to 1652 cm^{-1} (Random Coil/ α -helix).

For *Muga*-Traditional (fig 4.37 (h)), *Kolakhar* was used. Here, the peaks that were lost are 1315 cm^{-1} (Phenol or tertiary alcohol, OH bend), 901 cm^{-1} (Skeletal C-C vibrations), 877 cm^{-1} (carbon-ate groups) [136], and 447 cm^{-1} (Aryl disulfides (S-S stretch)). The new peaks formed are 3083 cm^{-1} (Pendant (vinylidene) C-H stretch), 1699 cm^{-1} , 1642 cm^{-1} (Secondary amine, NH bend), 482 cm^{-1} (Polysulfides (S-S stretch)) and 471 cm^{-1} (Aryl disulfides/Polysulfides (S-S stretch)).

The soil burial results gave the biodegraded *Muga* samples, and from here we can relate that the loss of certain bonds, mainly OH stretching at $\sim 3400\text{ cm}^{-1}$, and other bonds in different treatments confirms the effect of degradation. Extra peaks that are meant for polysulfides were seen in all the degraded samples. Thus, the presence of extra peaks for polysulfides can be attributed to an important factor in degrading *Muga* silk.

The pre-and post-biodegradation FTIR graph of *Pat* silk is shown in Fig 4.38. *Pat*-Raw (fig 4.38 (a)) peaks at 3414 cm^{-1} (O H stretching) [113], and 1070 cm^{-1} (Alkyl-substituted ether, Cyclic ethers, large rings, C-O stretch) were lost after degradation; however, new peaks were seen to have formed at 3297 cm^{-1} (Normal “polymeric” OH stretch), and 471 cm^{-1} (Aryl disulfides/Polysulfides (S-S stretch)). There were some peak shifts noticed, 1698 cm^{-1} (β -turn conformation of the hairpin-folded antiparallel β -sheet structure) to 1703 cm^{-1} (β -sheet); 1642 cm^{-1} to (random coils/extended chains) 1660 cm^{-1} (random coil, α -helix conformation, or both); 1017 cm^{-1} (Aliphatic phosphates (P-O-C stretch)) to 1040 cm^{-1} (Aliphatic phosphates (P-O-C stretch) or Primary amine, CN stretch) ; and 998 cm^{-1} to 1002 cm^{-1} were both in the same range for Aliphatic phosphates (P-O-C stretch) fig 4.38 (a).

Physico-chemical, Antibacterial, Antioxidant, Bio Compatibility, and Biodegradation Studies of Washed and Dyed Eri, Muga, and Pat Silk Fabric

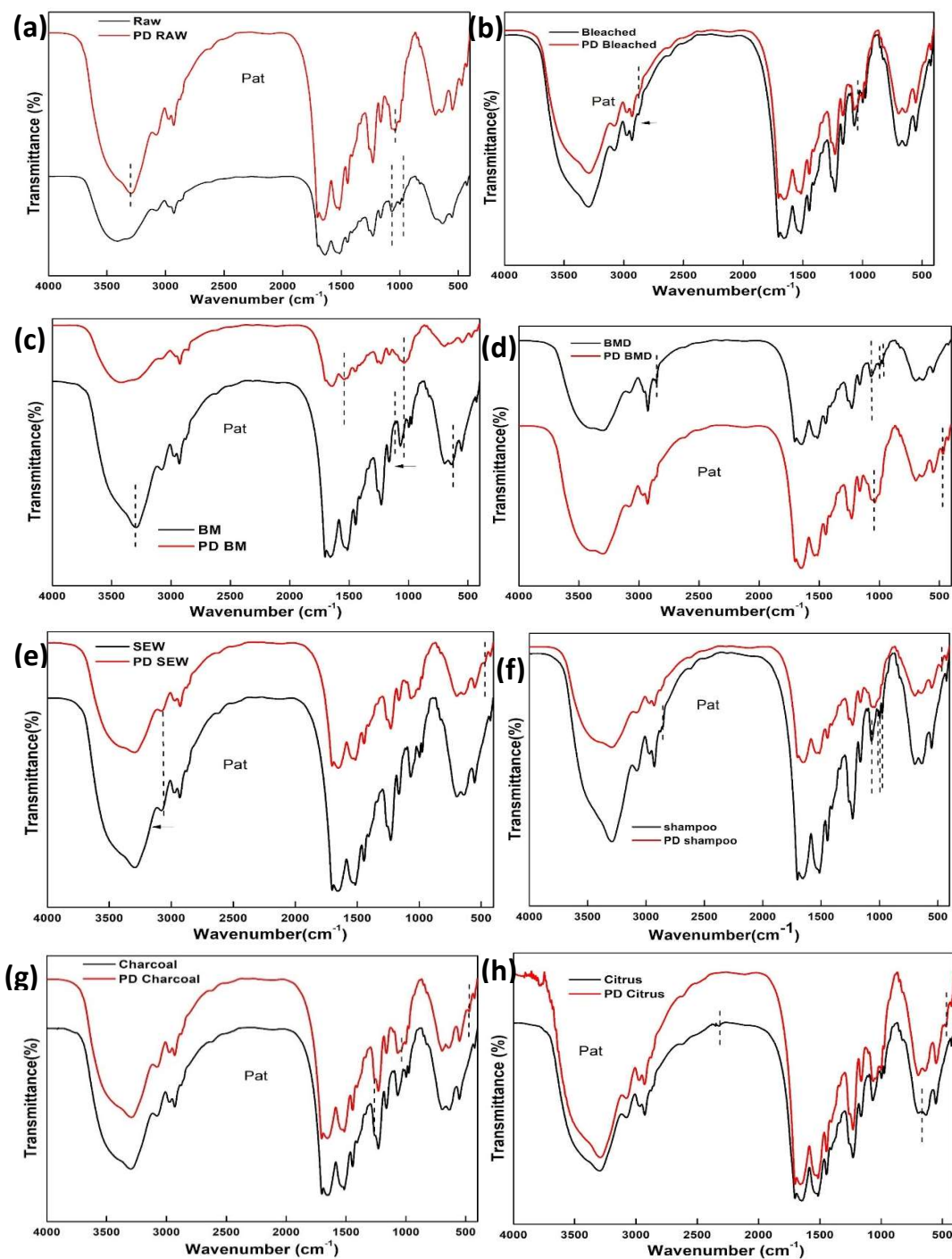


Fig 4.38: Pat pre- and post-degradation (a)Raw (b) Bleached (c) Bleached-Mordant (d) Bleached-Mordant-Dye (e) Detergent (SEW) (f) Shampoo (g) Act. Charcoal (h) Traditional (Citrus)

Physico-chemical, Antibacterial, Antioxidant, Bio Compatibility, and Biodegradation Studies of Washed and Dyed Eri, Muga, and Pat Silk Fabric

In *Pat*-bleached (fig 4.38 (b)), unlike any degradation, no peaks were lost after degradation; however, new peaks were formed at 1340 cm^{-1} (Organic phosphates (P=O stretch)), 1260 cm^{-1} (Organic phosphates (P=O stretch)) and 1015 cm^{-1} (Aliphatic phosphates (P-O-C stretch)).

For *Pat*-BM (fig 4.38 (c)), the peaks that were lost were: 3282 cm^{-1} (Normal “polymeric” OH stretch), 1409 cm^{-1} (Phenol or tertiary alcohol, OH bend), 1104 cm^{-1} (Alkyl-substituted ether, Cyclic ethers, large rings, C-O stretch), 1069 cm^{-1} (Alkyl-substituted ether, C-O stretch), 1016 cm^{-1} (Aliphatic phosphates (P-O-C stretch)), 998 cm^{-1} (Aliphatic phosphates (P-O-C stretch)), 975 cm^{-1} (Aliphatic phosphates (P-O-C stretch)). There were peaks that got formed newly at 3421 cm^{-1} (O H stretching) [113], 2854 cm^{-1} (Methylene (-CH₂-) C-H Symmetric stretch), 2310 cm^{-1} , 1540 cm^{-1} (N-H bending vibration/C-N stretching vibration) [141], 1341 cm^{-1} (Organic phosphates (P=O stretch)), 1262 cm^{-1} (Organic phosphates (P=O stretch)), 1035 cm^{-1} (Primary amine, CN stretch), 471 cm^{-1} (Aryl disulfides/Polysulfides (S-S stretch)). There were also some peak shifts that were found in 1703 cm^{-1} ((β -sheet)) to 1698 cm^{-1} (β -turn conformation of the hairpin-folded antiparallel β -sheet structure); 1657 cm^{-1} (random coil, helical conformation, or both) to 1644 cm^{-1} (random coils/extended chains); 637 cm^{-1} (Thioethers, CH₃-S- (C-S stretch)) to 663 cm^{-1} (Alkyne C-H bend).

In the case of *Pat*-BMD (fig 4.38 (d)), the peaks that were lost are 3082 cm^{-1} (Pendant (vinylidene) C-H stretch), 2854 cm^{-1} (Methylene (-CH₂-) C-H Symmetric stretch), 1341 cm^{-1} (Organic phosphates (P=O stretch)), 1105 cm^{-1} (Alkyl-substituted ether, Cyclic ethers, large rings, C-O stretch), 1069 cm^{-1} (Alkyl-substituted ether, C-O stretch), 1017 cm^{-1} (Aliphatic phosphates (P-O-C stretch)), 997 cm^{-1} (Aliphatic phosphates (P-O-C stretch)), 975 cm^{-1} (Aliphatic phosphates (P-O-C stretch)), 880 cm^{-1} (carbon-ate groups) [136] and 426 cm^{-1} . The peaks that were formed newly were 1039 cm^{-1} (Primary amine, CN stretch), 645 cm^{-1} (Thioethers, CH₃-S-), and 468 cm^{-1} (Aryl disulfides (S-S stretch)). A peak shift has been seen for 1648 cm^{-1} (random coils) to 1651 cm^{-1} (random coils).

For *Pat*-Detergent (fig 4.38 (e)), two peaks were lost after degradation: 1341 cm^{-1} (Organic phosphates (P=O stretch)) and 975 cm^{-1} (Aliphatic phosphates (P-O-C stretch)). However, the peaks that were formed are 2969 cm^{-1} (Methyl (-CH₃) C-H Asymmetric stretch), 1534 cm^{-1} (N-H bending), 1261 cm^{-1} (Organic phosphates (P=O stretch)),

642 cm^{-1} (Thioethers, CH₃-S- (C-S stretch)) and 473 cm^{-1} (Aryl disulfides/polysulfides (S-S stretch)). The peak shift was observed for 1659 cm^{-1} (alpha-helices) to 1655 cm^{-1} (random coils).

For *Pat-Shampoo* (fig 4.38 (f)) three peaks were lost, 1068 cm^{-1} (Alkyl-substituted ether, C-O stretch), 997 cm^{-1} (Aliphatic phosphates (P-O-C stretch)) and 975 cm^{-1} (Aliphatic phosphates (P-O-C stretch)). The newly formed peaks are 1535 cm^{-1} (N-H bending vibration/C-N stretching vibration) [141], 1054 cm^{-1} (Primary amine, CN stretch), 1040 cm^{-1} (Primary amine, CN stretch). 879 cm^{-1} (carbon-ate groups) [136], 643 cm^{-1} (Thioethers, CH₃-S- (C-S stretch)), and 471 cm^{-1} (Aryl disulfides/polysulfides (S-S stretch)). The peak shift occurred in 1655 cm^{-1} (random coils) to 1659 cm^{-1} (alpha-helices).

Pat-Act Charcoal (fig 4.38 (g)), no peak was lost; however, the formation of new peaks was seen at 1340 cm^{-1} (Organic phosphates (P=O stretch)), 1261 cm^{-1} (Organic phosphates (P=O stretch)), 640 cm^{-1} (Thioethers, CH₃-S- (C-S stretch)), and 471 cm^{-1} (Aryl disulfides/polysulfides (S-S stretch)). The peak shift was observed at 1656 cm^{-1} (Random coil/ a-helix) to 1658 cm^{-1} (Random coil/ a-helix) and 1016 cm^{-1} (Phosphate ion) to 1000 cm^{-1} (Phosphate ion).

In the case of *Pat-Citrus* (fig 4.38 (h)), the peaks that were lost are 2352 cm^{-1} , 826 cm^{-1} (1,4-Disubstitution (para) C-H), and 667 cm^{-1} (Alkyne C-H bend). The newly formed peaks are 1340 cm^{-1} (Organic phosphates (P=O stretch)), 1261 cm^{-1} (Organic phosphates (P=O stretch)), 1103 cm^{-1} (Alkyl-substituted ether, Cyclic ethers, large rings, C-O stretch), 1042 cm^{-1} ((Primary amine, CN stretch), 469 cm^{-1} (Aryl disulfides (S-S stretch)). A peak shift was seen for 1647 cm^{-1} to 1659 cm^{-1} .

Overall, the degradation of all the silks revealed the presence of carboxyl, carbonyl, nitro, and sulfoxide groups, which may have caused oxidative damage to the samples [142]. Some bands were found in almost the majority of the samples, which indicates S=O asymmetric stretching with minor contributions from the stretching of sulfoxide, symmetric stretching of Si=O=Si bridges, and bending of O=S=O linkage, which was assigned to SiO₂ and probably originated from the burial environment [142-144].

According to published research, the crystallites are consistently enmeshed in an amorphous matrix that is abundant in residues with large, polar side chains. Tyrosine residues are present in the amorphous region, which is thought to adopt loose structures like distorted b-sheets, distorted b-turns, and 31-helices that are thought to give silk its elastic quality. It is complicated to comprehend how silk fibroin degrades because of its complex structure [142, 145, 146]. A proposed model for dragline spider silk self-assembly: insights from the effect of repetitive domain size on fiber progenies.

4.3.4 Haemolysis Activity of *Eri*, *Muga*, and *Pat*

The hemolytic assay is a crucial test for substances that come in direct contact with blood [147,148]. Hemocompatibility was evaluated using the haemolysis test for biomedical materials. The results of the haemolysis percentages of *Eri*, *Muga*, and *Pat* and their respective treatments are displayed in Fig 4.39. All of *Eri*'s samples had haemolysis rates of 0.6% or less. This suggests *Eri* silk is highly bio-compatible.

For *Muga*, *Muga*-BD showed the lowest haemolysis (%) of 0.03%, followed by *Muga*-RAW at 0.04%, and both are non-significant. The sequence followed by *Muga* in decreasing order is (fig 4.39), *Muga*-BDM > *Muga*-BMDM > *Muga*-SIM > *Muga*-BMD > *Muga*-B > *Muga*-RAW > *Muga*-BD. The untreated *Muga* and *Muga*-BD were found to be biocompatible, as the hemolysis (%) was low; however, in other treatments of the *Muga* silk fabrics, the hemolysis (%) increased. The range of haemolysis in all *Muga* silk treatments was in acceptable range, making all these treatments biocompatible.

Pat-Raw has been discovered to have a significantly high haemolysis percentage, rendering it non-biocompatible in the case of *Pat*. Since there have been reports claiming that *Pat* silk has good biocompatibility, the outcome has been confirmed once more [130]. The haemolysis index of a substance is deemed safe when it is less than 5%, in accordance with the ISO standard (document 10 993-5 1992) [147, 149]. The decreasing order of haemolysis % for *Pat* is as follows (fig 4.39), *PAT*-RAW > *PAT*-B > *PAT*-BM > *PAT*-BDM > *PAT*-BMDM > *PAT*-BMD > *PAT*-SIM > *PAT*-BD. For the three silk fabrics, BD proved to have the lowest haemolysis activity. This can also be related to the leaching of trapped curcumin leading to more available curcumin for reaction in the liquid form.

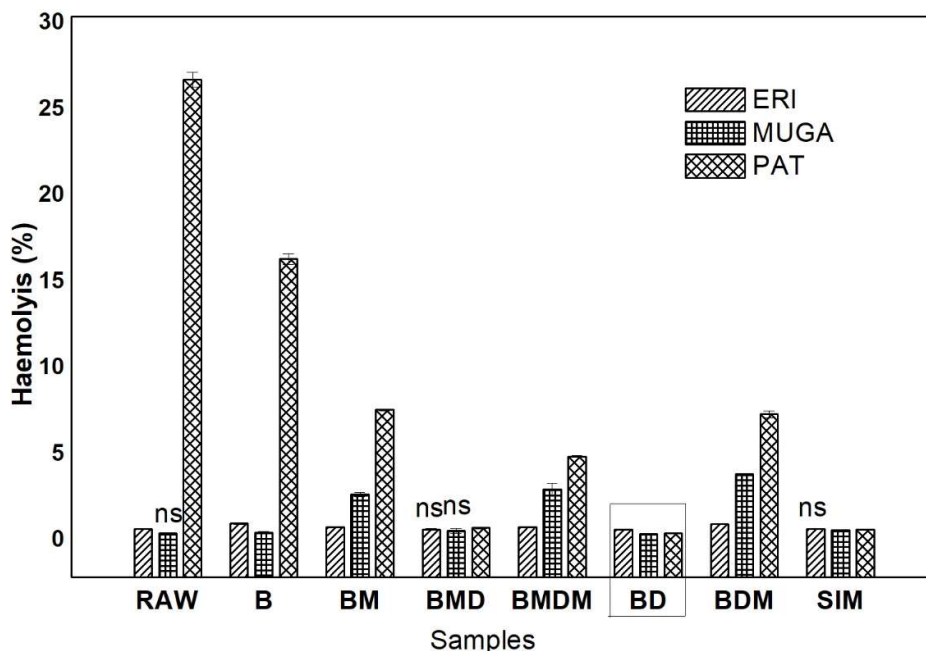


Fig 4.39: Haemolysis activity of *Eri*, *Muga*, and *Pat* fabric (Data are reported as mean \pm SD from three independent experiments; *P < 0.05 compared with BD; ns= non-significantly different, while rest are significantly different)

4.3.5 Antibacterial activity of *Eri*, *Muga*, and *Pat*

Table 4.14: Zone of clearance created by different chemicals in disc diffusion assay against *S. aureus* and *K. pneumoniae* (all units in mm)

Name Disc=5mm	Gentamicin (Gen) mm	DMSO	Curcumin (Cur)	Tannic Acid (TA)	Cur+TA	Gen+Cur
<i>S.aureus</i>	22 \pm 0.24	ND	5.1 \pm 0.4	12 \pm 0.5	7.5 \pm 0.2	22 \pm 0.33
<i>K. pneumoniae</i>	22 \pm 0.3	ND	5.0 \pm 0.4	7.5 \pm 0.5	6.5 \pm 0.5	20 \pm 0.42



Fig 4.40: Disc Diffusion of *S.aureus* a) DMSO and Curcumin b) Gentamicin (Gen) and Tannic acid and c) Gentamicin + Curcumin (Gen + cur) and Tannic acid + Curcumin (com)



Fig 4.41: Disc Diffusion of *K. pneumoniae* a) DMSO and Curcumin b) Gentamicin (Gen) and Tannic acid and c) Gentamicin + Curcumin (Gen + cur) and Tannic acid + Curcumin (com)

Anthraquinone, flavonoid, tannin, and naphthoquinone compounds, which have antibacterial properties, are known to be present in natural dyes. All the strains used were sensitive to the positive control Gentamicin, and no inhibition zone has been observed for the negative control DMSO. No synergistic effect was observed when curcumin was combined with gentamicin in any of the strains. As can be seen in Table 4.14, a thin line of inhibition was seen by curcumin against *Klebsiella pneumoniae* (MTCC 618) and *Staphylococcus aureus* (MTCC 3160). The highest zone of inhibition by tannic acid has been seen in *S. aureus*, and the lowest zone of inhibition can be seen in *K. pneumoniae*. Tannic acid has antibacterial effects on both gram-positive and gram-negative bacteria. Tannic acid's clear zone appears to be brown due to the brownish color of the tannic acid. Fig 4.40 (c) and 4.41 (c) show the antibacterial efficacy of the combination of curcumin and tannic acid; and Curcumin-loaded gentamicin. From the figure, it can be seen that *S. aureus* shows the highest inhibition for curcumin-loaded gentamicin. The highest inhibition zone of the tannic acid and curcumin combination can be seen in *S.*

aureus (~7.5 mm); however, *K. pneumoniae* shows smaller inhibition. Table 4.14 shows the inhibition zones formed by each treatment in the gram-positive and negative bacteria. The results suggest the antibacterial nature of curcumin and tannic acid. All treatments have a stronger antibacterial effect against Gram-positive bacteria than they do against Gram-negative bacteria. Curcumin has also been observed to hinder the effectiveness of other antimicrobial substances and to be difficult to spread. This is demonstrated by the fact that when gentamicin and curcumin are used together, the inhibition zone is smaller than when gentamicin is used alone. A similar trend was also seen in the combination of tannic acid and curcumin.

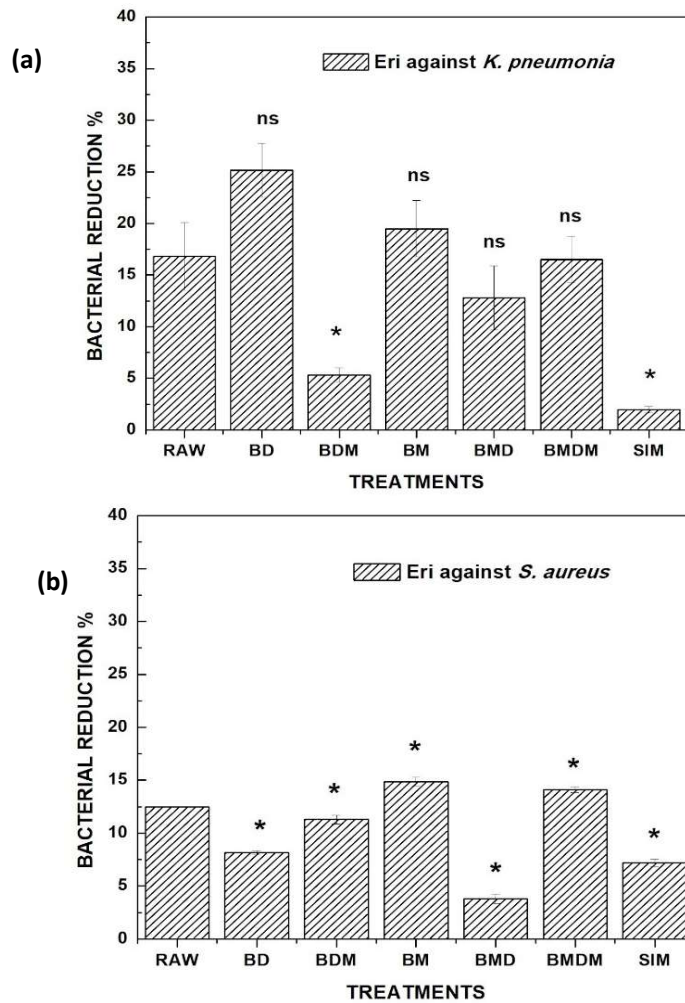


Fig 4.42: Antibacterial activity of treated Eri samples against a) *K. pneumoniae* and b) *S.aureus* (Data are reported as mean \pm SD from three independent experiments; *P < 0.05 compared with untreated ; *= significantly different, ns= non-significantly different)

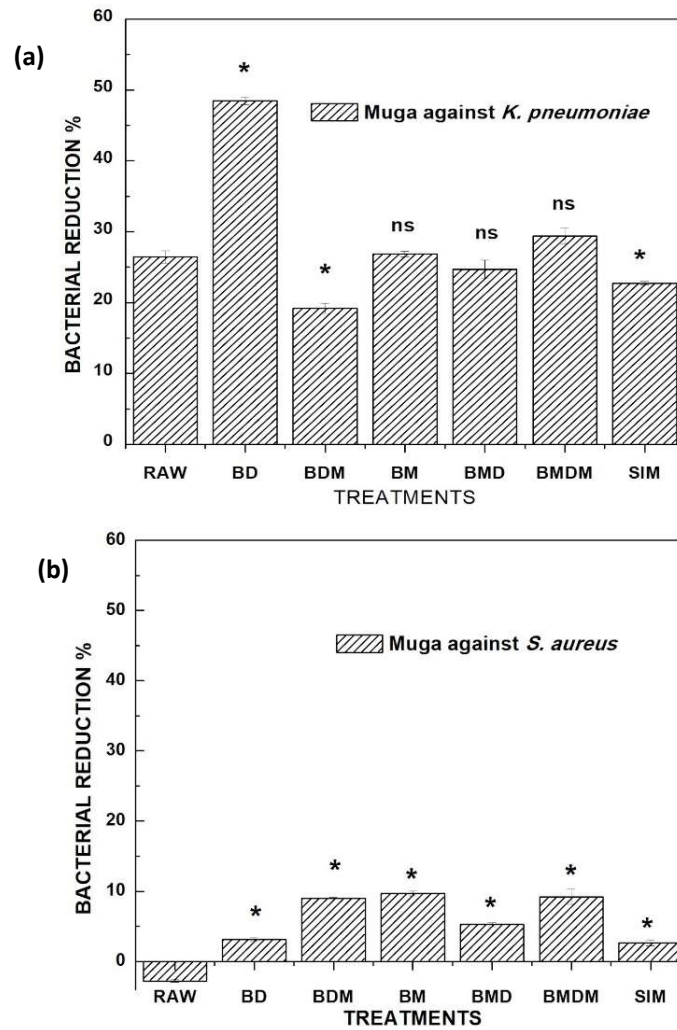


Fig 4.43: Antibacterial activity of treated Muga samples against a) *K. pneumoniae* and b) *S.aureus*

(Data are reported as mean \pm SD from three independent experiments; *P < 0.05 compared with untreated; *= significantly different, ns= non-significantly different)

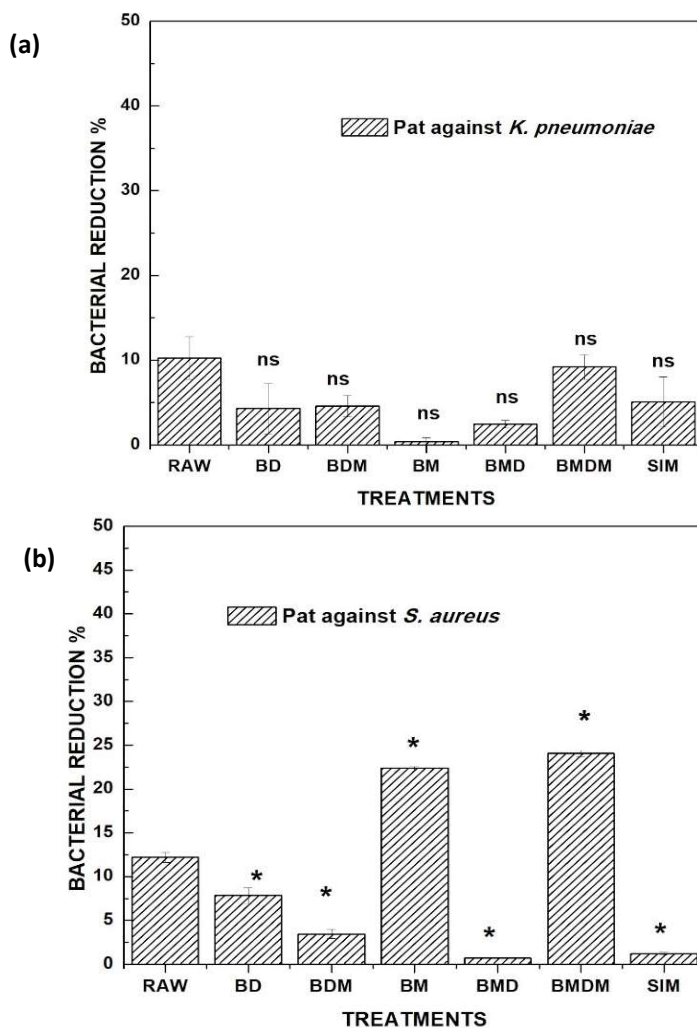


Fig 4.44: Antibacterial activity of treated Pat samples against a) *K. pneumoniae* and b) *S. aureus*

(Data are reported as mean \pm SD from three independent experiments; *P < 0.05 compared with untreated; *= significantly different, ns= non-significantly different)

The antibacterial reduction percentage against gram-negative *k. pneumoniae* of *Eri* showed the highest reduction for *Eri*-BD (~25%), followed by *Eri*-BM (~19%), *Eri*-RAW (~17%), *Eri*-BMDM (~16%), *Eri*-BMD (~13%), *Eri*-BDM (~5%), and lastly *Eri*-SIM (~2%) as seen in Fig 4.42 (a). However, *Eri*-BD, *Eri*-BM, *Eri*-RAW, *Eri*-BMDM, and *Eri*-BMD are non-significant. In gram-positive *S. aureus*, even though the results are significantly different, but overall reduction percent is very low compared to gram-negative. For *S. aureus*, *Eri* showed the highest reduction percentage of ~15% by *Eri*-BM followed by ~14% for *Eri*-BMDM. The decreasing sequence of reduction for *S. aureus*

Physico-chemical, Antibacterial, Antioxidant, Bio Compatibility, and Biodegradation Studies of Washed and Dyed Eri, Muga, and Pat Silk Fabric

by *Eri* is, *Eri*-BM (~15%) > *Eri*-BMDM (14%) > *Eri*-RAW (~12%) > *Eri*-BDM (~11%) > *Eri*-BD (~8%) > *Eri*-SIM (~7%) > *Eri*-BMD (~4%) as seen in Fig 4.42 (b).

In the case of *Muga*, the antibacterial reduction percentage against *K. pneumoniae* was seen to be highest for *Muga*-BD (~48%). The decreasing order of bacterial reduction of *Muga* for *K. pneumoniae* is *Muga*-BD (~48%) > *Muga*-BMDM (~29%) ≥ *Muga*-BM (27%) ≥ *Muga*-Raw (~26%) ≥ *Muga*-BMD (~25%) > *Muga*-BDM (~19%) as seen in Fig 4.43 (a). However, the results of *Muga*-BMDM, *Muga*-BM, *Muga*-Raw, and *Muga*-BMD are not significantly different. In the case of *S. aureus* as seen in Fig 4.43 (b), *Muga*-RAW showed an adverse result, and to cross-check, the experiment was carried out several times to confirm, but the same results came each time. *Muga*-Raw actually helped in the growth of *S. aureus* thus giving the bacterial reduction % in negative. However, the results of its treatments were significantly different. The decreasing order of bacterial reduction is, *Muga*-BM (~9.7%) > *Muga*-BMDM (~9.2%) > *Muga*-BDM (~9%) > *Muga*-BMD (~5.3%) > *Muga*-BD (~3%) > *Muga*-SIM (~2.6%) > *Muga*-RAW (~ -2.8%).

The results for *Pat* against *K. pneumoniae*, showed all the results to be non-significant compared to *Pat*-RAW as can be seen in Fig 4.44 (a). The average reduction percentage ranged from 0.4 % - 10.3%, however, they aren't significantly different. Thus, *Pat* silk has a negligible antibacterial effect against *K. pneumoniae*. The antibacterial results of *Pat* against *S. aureus* showed better results compared to *K. pneumoniae*. The decreasing order of bacterial reduction for *Pat* against *S. aureus* is *Pat*-BMDM (~24%) > *Pat*-BM (~22%) > *Pat*-RAW (~12%) > *Pat*-BD (~8%) > *Pat*-BDM (~3%) > *Pat*-SIM (~1%) > *Pat*-BMD (~0.7%) as seen in fig 4.44 (b).

Comparing all the results, it has been found that, for *K. pneumoniae*, *Muga*-BD showed significantly good antibacterial results, and *Muga* as a whole showed better antibacterial results compared to *Eri* and *Pat* samples. However, for *S. aureus*, *Pat* silk showed better antibacterial results compared to *Eri* and *Muga* samples. The majority of non-significant differences were observed for *K. pneumoniae*; however, *S. aureus* samples had significantly different results. The absence of the antibacterial effect of *Eri* has been previously presented in contact inhibition with no formation of a clear zone [150]; however, in this method, we found some antibacterial activity for raw *Eri*, both for *K. pneumoniae* and *S. aureus*. The absence of a clear zone for *Eri*, *Muga*, and *Pat* has

also been reported earlier [151]. These results can be linked to our findings, as contact inhibition has been observed without the formation of clear zones, but antibacterial activity was seen for the maximum samples when AATCC Test 100-2004 was carried out. The result showing that *Muga* enhances bacterial growth (*S. aureus*) can be related to reports suggesting the presence of sericin as a factor that helps in bacterial growth [152, 153].

4.4 To develop a silk-based water filtration setup and a formulation for silk washing

4.4.1 Filtration method

In accordance with antibacterial results, for filtration, raw samples were selected, with BD, BM, BMD, and BMDM for comparison. As can be seen in Fig 4.45 (a), It was found that *Eri*-Raw and *Eri*-BD showed the highest bacterial reduction and the results aren't significantly different. However, for *Eri*-BM, *Eri*-BMD, and *Eri*-BMDM comparatively low reduction was observed. In the case of *Muga* as seen in Fig 4.45 (b), *Muga*-Raw, *Muga*-BD, and *Muga*-BM showed the highest bacterial reduction, with *Muga*-BMD and *Muga*-BMDM with lower reduction. In the case of *Pat*, high standard deviations were observed and all the results were not significantly different. From these results, we can determine that since filtration is a quick process, the mesh size plays a crucial role. Unlike the results of antibacterial, here raw samples showed better results. It may be due to an increase in fiber gaps during the processing of treatments that ultimately increase the mesh size and lead to poor filtration. This suggests that for filtration, non-degummed or with a very small mesh size prepared by a suspension can act better compared to silk after being made into a fabric [154].

Physico-chemical, Antibacterial, Antioxidant, Bio Compatibility, and Biodegradation Studies of Washed and Dyed Eri, Muga, and Pat Silk Fabric

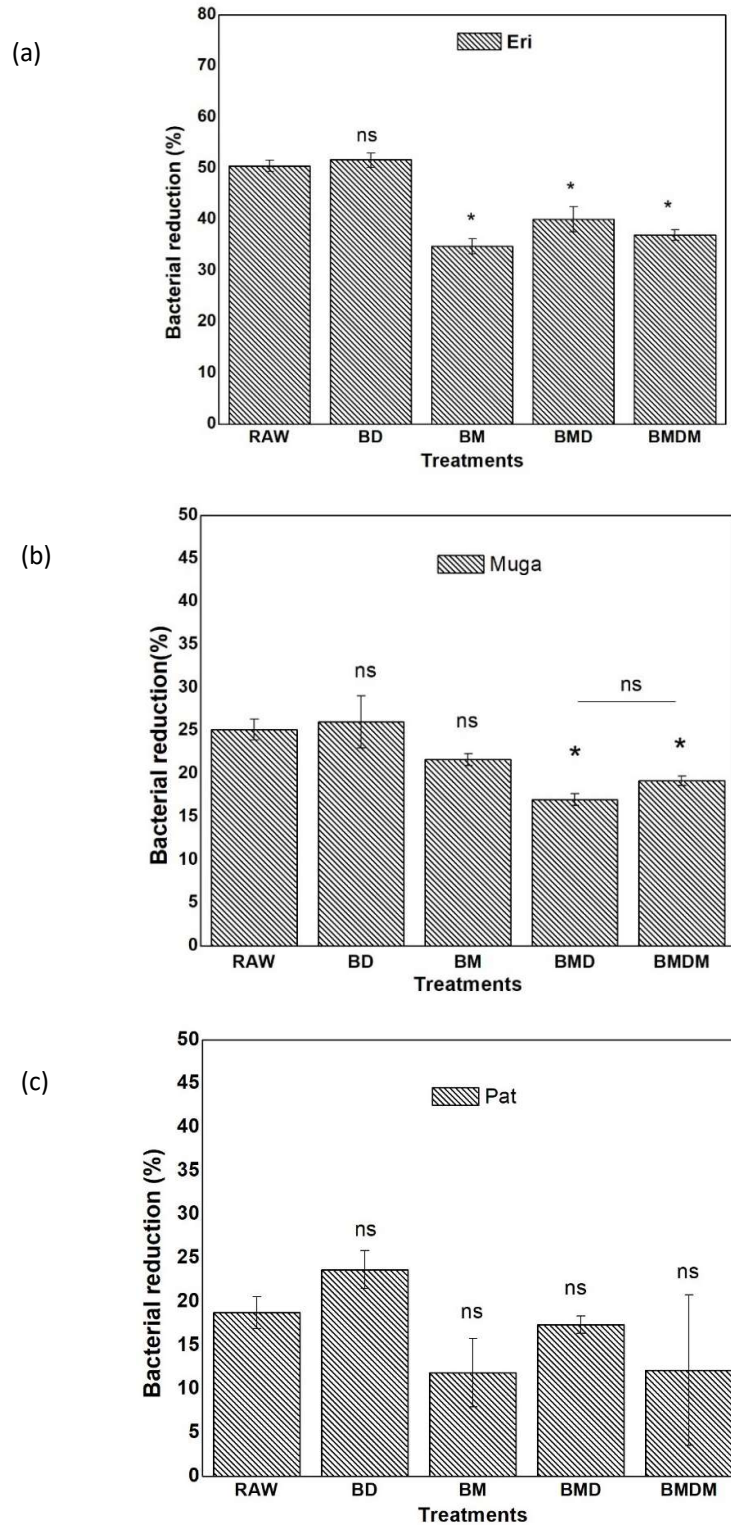


Fig 4.45: Bacterial reduction after filtration with (a) *Eri* (b) *Muga* and (c) *Pat* fabric (Data are reported as mean \pm SD from three independent experiments; *P < 0.05 compared with untreated; *= significantly different, ns= non-significantly different)

4.4.2 Washing formulation

4.4.2.1 Color analysis

From objective 1, considering all the results, and the scantiness in *Muga* washing agents, an activated charcoal study has been detailed to create a washing formulation. An analysis of alternatives has been done in order to formulate the washing agent. The Red Green Blue (RGB) color model is used in image detection and portrayal to a display in electronic systems as well as traditional photography. In different intensities, an object will reflect or emit some wavelengths of light while absorbing or not emitting others. Hue, Saturation, and Brightness are three dimensions that can be derived from RGB values and are comparatively independent. The scanned images shown in Fig 4.46 were used to calculate the RGB. RM accounts for 61.82 percent of the luminosity and has a 40.09 percent saturation percentage. The luminosity percent of all treated samples lies between 66–69 resulting in a 4–8% increase compared to *Muga*-Raw. In comparison to *Muga*-Raw, it was discovered that *Muga*-Act Charcoal exhibits the highest luminosity and performs better when these two factors are combined without significantly deviating from the *Muga*-Raw's hue angle. In the HSL color space, the hue angle is thought to be a component comparable to human vision [18]. When using treatments like *Muga*-Water, *Muga*-Kolakhar, and *Muga*-Detergent, the hue angle deviation is more pronounced, which indicates a change in the original color.

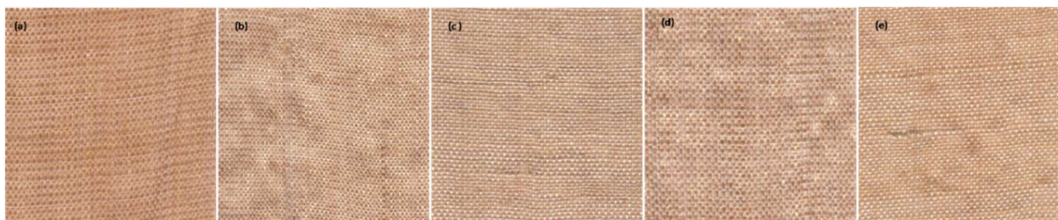


Fig 4.46: Scanned of a) *Muga*-Raw, b) *Muga*-Water c) *Muga*-Kolakhar d) *Muga*-Act Charcoal e) *Muga*-Detergent[155]

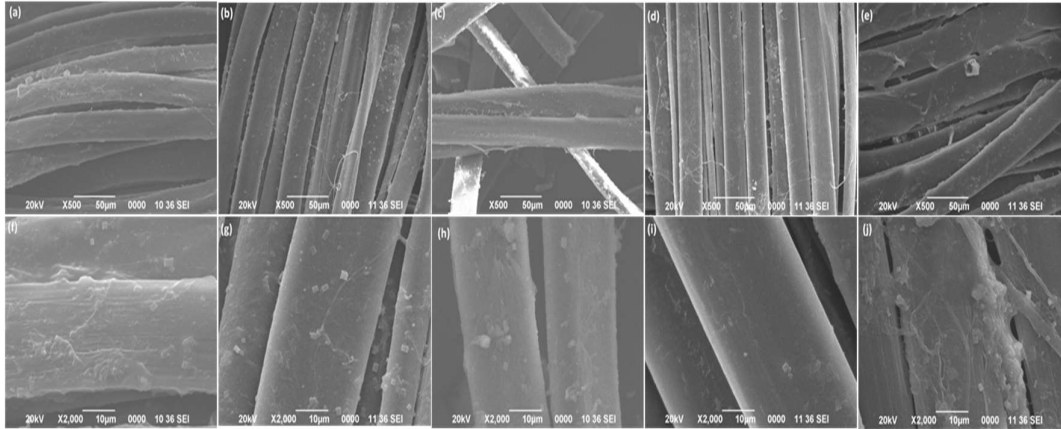


Fig 4.47: SEM images at 500X and 2000X of a) *Muga*-Raw, b) *Muga*-Water c) *Muga*-Kolakhar d) *Muga*- Act Charcoal e) *Muga*-Detergent[155]

4.4.2.2 SEM imaging

The SEM images of the washed and unwashed *Muga* cloth pieces are presented in fig 4.47. The changes in the fiber's surface brought on by exposure to various washing agents are visible in the images that have been magnified by 500X and 2000X, respectively. The observation of intact single fibers in all treatments and *Muga*-Raw is supported by the fact that silk is known to have high bending deformation without breaking [156]. The SEM images revealed some evidence comparing longitudinal fibrillation and fiber peeling. According to SEM findings, the *Muga*-Kolakhar, *Muga*-Act Charcoal, and *Muga*-Water do not exhibit any fiber-level damage. Sericin is present in the *Muga*-Detergent case, but there is also evidence of fiber-level damage. Even though the fiber core (silk fiber) is a highly oriented crystalline fibrous structure that is insoluble in water, it is highly absorbent and gets wet easily by water [157]. The fiber swells as a result of wet abrasion, weakening the inter-microfibril interactions and making the fiber susceptible to fibrillation [158]. The *Muga*-Detergent micro-cracks that are visible cause the roughness of fabrics and eventually weaken their tensile strength.

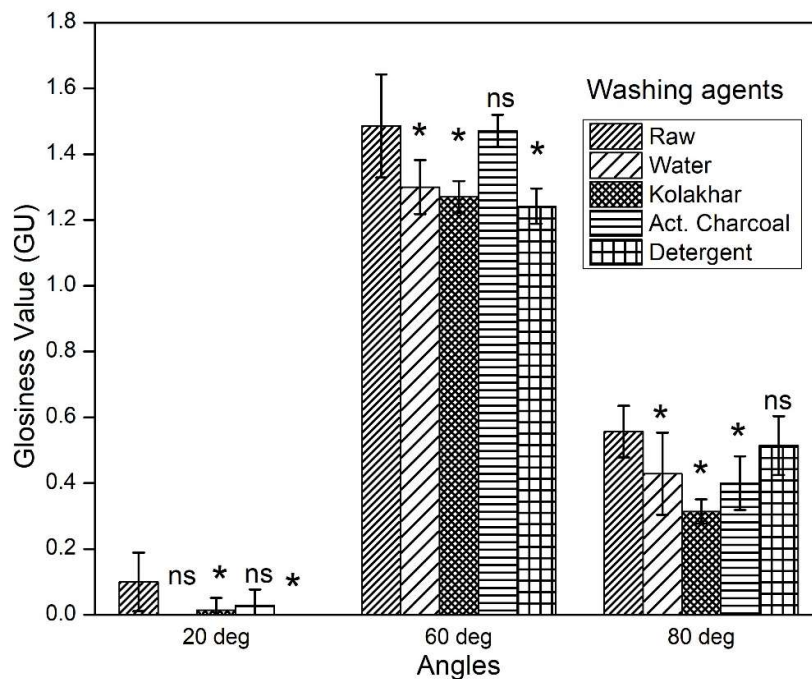


Fig 4.48: Glossiness value at 20°, 60°, 80° of treated and raw *Muga* (Data are reported as mean \pm SD from three independent experiments; *P < 0.05 compared with untreated; *= significantly different, ns= non-significantly different) [155]

4.4.2.3 Glossiness

Gloss is a crucial aspect of physical appearance. Glossiness is characterized by the presence of bright highlights where incident illumination is reflected in the specular direction. Although the samples' glossiness varied depending on which angle, they were viewed from, the treated samples showed little variation. The glossiness Unit (GU) was 0.100 (*Muga*-Raw), 0.000 (*Muga*-Water), 0.014 (*Muga*-Kolakhar), 0.029 (*Muga*- Act Charcoal), and 0.000 (*Muga*-Detergent) at 20 degrees. The GU was determined to be 1.486 (*Muga*-Raw), 1.314 (*Muga*-Water), 1.286 (*Muga*-Kolakhar), 1.471 (*Muga*-Act Charcoal), and 1.257 (*Muga*-Detergent) at 60 degrees. The GU values at 80 degrees were 0.557 (*Muga*-Raw), 0.429 (*Muga*-Water), 0.314 (*Muga*-Kolakhar), 0.400 (*Muga*-Act Charcoal), and 0.514 (*Muga*-Detergent). The findings of Fig 4.48 indicate that CWM has a better gloss than the rest, with *Muga*-Water and *Muga*-Detergent having no glossiness at an angle of 20° and *Muga*-Kolakhar having lower GU values in all angles. The smooth surface of *Muga*-Act Charcoal and *Muga*-Kolakhar, as opposed to the fibrillated surface

of *Muga*-Detergent, is indicated by the SEM images. This could be a potential explanation for the smoother surface of *Muga*-Act Charcoal and *Muga*-*Kolakhar*, which has better glossiness [155]. The glossiness value is non-significant for *Muga*-Act Charcoal at 20° and 60°. However, at 80°, only *Muga*-Detergent showed a non-significant difference at 80°, while the rest were significantly different.

Based on the findings, a washing powder has been created for *Muga*. The northeastern region of India is home to the lustrous golden *Muga* silk. Because silk is expensive, the washing process is crucial in maintaining the shine without lowering the quality of the fiber. *Kolakhar* has been used traditionally for washing *Muga* silk. As shown by the optical microscope images, SEM images, and FTIR results, *Muga*-Act Charcoal is a better washing agent for *Muga* without sacrificing the quality of the fiber when taking into account the after-result shine. For the sole purpose of washing *Muga*, a commercial washing agent can be prepared.

References:

- [1] Zhou, W. and Wang, Z. L. Scanning microscopy for nanotechnology: techniques and applications. *Springer science & business media*, 2007.
- [2] Mohammed, A. and Abdullah, A. Scanning electron microscopy (SEM): A review. in *Proceedings of the 2018 International Conference on Hydraulics and Pneumatics—HERVEX, Băile Govora, Romania*. 7-9.
- [3] Zhou, W., Apkarian, R., Wang, Z. L., Joy, D. Fundamentals of scanning electron microscopy (SEM). *Scanning microscopy for nanotechnology: techniques and applications*, 1-40, 2007.
- [4] Tanzi, M. C. and Farè, S. *Characterization of polymeric biomaterials*. Woodhead Publishing, 2017.
- [5] Hu, Y., Shi, M., Liu, L., Yu, J., and Fan, Y. Top-down extraction of surface carboxylated-silk nanocrystals and application in hydrogel preparation. *International Journal of Biological Macromolecules*, 174: 162-174, 2021.
- [6] Dutta, S., Talukdar, B., Bharali, R., Rajkhowa, R., and Devi, D. Fabrication and characterization of biomaterial film from gland silk of muga and eri silkworms. *Biopolymers*, 99(5): 326-333, 2013.
- [7] Ahmed, M. and Saikia, J. P. Traditional Washing Formulations Outstand Commercial Ones for Washing *Antheraea assamensis* (Muga) Silk Cloth. *Applied Biological research*, 455-462 2022.
- [8] Van Amber, R. R., Niven, B. E., and Wilson, C. Effects of laundering and water temperature on the properties of silk and silk-blend knitted fabrics. *Textile Research Journal*, 80(15): 1557-1568, 2010.
- [9] Amiraliyan, N., Nouri, M., and Kish, M. Effects of some electrospinning parameters on morphology of natural silk-based nanofibers. *Journal of Applied Polymer Science*, 113(1): 226-234, 2009.
- [10] Wang, H., Zhang, Y., Shao, H., and Hu, X. Electrospun ultra-fine silk fibroin fibers from aqueous solutions. *Journal of Materials Science*, 40: 5359-5363, 2005.
- [11] Horan, R. L., Antle, K., Collette, A. L., Wang, Y., Huang, J., Moreau, J. E., Volloch, V., Kaplan, D. L., and Altman, G. In vitro degradation of silk fibroin. *Biomaterials*, 26(17): 3385-3393, 2005.
- [12] Noisuwan, A., Hemar, Y., Wilkinson, B., and Bronlund, J. Adsorption of milk proteins onto rice starch granules. *Carbohydrate Polymers*, 84(1): 247-254, 2011.
- [13] Eliasson, A.-C. and Tjerneld, E. Adsorption of wheat proteins on wheat starch granules. *Cereal chemistry*, 67(4): 366-372, 1990.
- [14] Lundh, G., Eliasson, A.-C., and Larsson, K. Cross-linking of wheat storage protein monolayers by compression/expansion cycles at the air/water interface. *Journal of cereal science*, 7(1): 1-9, 1988.
- [15] Ryan, K. and Brewer, M. Purification and identification of interacting components in a wheat starch–soy protein system. *Food chemistry*, 89(1): 109-124, 2005.
- [16] Wannerberger, L., Wahlgren, M., and Eliasson, A. Adsorption of protein fractions from wheat onto methylated silica surfaces. *Cereal chemistry*, 73(4): 499-505, 1996.
- [17] Zeileis, A., Fisher, J. C., Hornik, K., Ihaka, R., McWhite, C. D., Murrell, P., Stauffer, R., and Wilke, C. colorspace: A toolbox for manipulating and assessing colors and palettes. *arXiv preprint arXiv:1903.06490*. 2019.

- [18] Pan, R., Gao, W., and Liu, J. Color clustering analysis of yarn-dyed fabric in HSL color space. In *2009 WRI World Congress on Software Engineering*. 273-278 (IEEE).
- [19] Luo, M. R., Cui, G., Rigg, B. Application: Endorsed by Inter-Society Color Council, TCG, Canadian Society for Color, Color Science Association of Japan, Dutch Society for the Study of Color, The Swedish Colour Centre Foundation, Colour Society of Australia, Centre Français de la Couleur. The development of the CIE 2000 colour-difference formula: CIEDE2000. *The development of the CIE*, 26(5): 340-350, 2001.
- [20] Joblove, G. H. and Greenberg, D. Color spaces for computer graphics. In *Proceedings of the 5th annual conference on Computer graphics and interactive techniques*. 20-25, 1978
- [21] Judd, D. Hue saturation and lightness of surface colors with chromatic illumination. *JOSA*, 30(1): 2-32, 1940.
- [22] Ganesan, P., Rajini, V., and Rajkumar, R. Segmentation and edge detection of color images using CIELAB color space and edge detectors. *INTERACT-2010*, 393-397, 2010.
- [23] Vigo, T. L. *Textile processing and properties: Preparation, dyeing, finishing and performance*. Elsevier, 2013.
- [24] Zhang, Y., Naebe, M. Lignin: A review on structure, properties, and applications as a light-colored UV absorber. *ACS Sustainable Chemistry & Engineering*, 9(4): 1427-1442, 2021.
- [25] Bianchetti, G. O., Devlin, C. L., and Seddon, K. Bleaching systems in domestic laundry detergents: a review. *Rsc Advances*, 5(80): 65365-65384, 2015.
- [26] Gerwert, K. and Kötting, C. Fourier transform infrared (FTIR) spectroscopy. *eLS*. 2010.
- [27] Kandori, H. Structure/function study of photoreceptive proteins by FTIR spectroscopy. *Bulletin of the Chemical Society of Japan*, 93(7): 904-926, 2020.
- [28] Rolere, S., Liengprayoon, S., Vaysse, L., Sainte-Beuve, J., and Bonfils, F. Investigating natural rubber composition with Fourier Transform Infrared (FT-IR) spectroscopy: A rapid and non-destructive method to determine both protein and lipid contents simultaneously. *Polymer Testing*, 43: 83-93, 2015.
- [29] Valtierra, D. *FTIR investigations of whey protein interactions in relation to model food systems*, McGill University (Canada), (2015).
- [30] Barron, C., Parker, M., Mills, E., Rouau, X., and Wilson, R. FTIR imaging of wheat endosperm cell walls in situ reveals compositional and architectural heterogeneity related to grain hardness. *Planta*, 220: 667-677, 2005.
- [31] Barth, A. and Zscherp, C. Substrate binding and enzyme function investigated by infrared spectroscopy. *FEBS letters*, 477(3): 151-156, 2000.
- [32] Kong, J. and Yu, S. Fourier transform infrared spectroscopic analysis of protein secondary structures. *Acta biochimica et biophysica Sinica*, 39(8): 549-559, 2007.
- [33] Tcholakova, S., Denkov, N. D., Sidzhakova, D., and Campbell, B. Effect of thermal treatment, ionic strength, and pH on the short-term and long-term coalescence stability of β -lactoglobulin emulsions. *Langmuir*, 22(14): 6042-6052, 2006.
- [34] Pervaiz, M. *Protein recovery from secondary paper sludge and its potential use as wood adhesive*. University of Toronto (Canada), 2012.

- [35] Nandiyanto, A. B. D., Oktiani, R., Ragadhita, R. How to read and interpret FTIR spectroscopy of organic material. *Indonesian Journal of Science and Technology*, 4(1): 97-118, 2019.
- [36] Coates, J. Interpretation of infrared spectra, a practical approach. *Encyclopedia of analytical chemistry*, (2000).
- [37] Asemani, M., Rabbani, A. R. Detailed FTIR spectroscopy characterization of crude oil extracted asphaltene: Curve resolve of overlapping bands. *Journal of Petroleum Science and Engineering*, 185: 106618, 2020.
- [38] Siesler, H. W., Kawata, S., Heise, H. M., and Ozaki, Y. *Near-infrared spectroscopy: principles, instruments, applications*. John Wiley & Sons, 2008.
- [39] Fried, A., & Richter, D. Infrared absorption spectroscopy. *Analytical Techniques for Atmospheric Measurement*, 72-146.
- [40] Wahyono, T., Astuti, D. A., Gede Wiryanan, I. K., Sugoro, I., and Jayanegara, A. in *IOP Conference Series: Materials Science and Engineering*. 042045 (IOP Publishing).
- [41] Mizuguchi, M., Nara, M., Kawano, K., and Nitta, K. FT-IR study of the Ca²⁺-binding to bovine α -lactalbumin: Relationships between the type of coordination and characteristics of the bands due to the Asp COO⁻ groups in the Ca²⁺-binding site. *FEBS letters*, 417(1): 153-156, 1997.
- [42] Socaciu, C., Fetea, F., Ranga, F., Bunea, A., Dulf, F., Socaci, S., and Pintea, A. Attenuated total reflectance-fourier transform infrared spectroscopy (ATR-FTIR) coupled with chemometrics, to control the botanical authenticity and quality of cold-pressed functional oils commercialized in Romania. *Applied Sciences*, 10(23): 8695, 2020.
- [43] Souza, N. F., Pinheiro, J. A., Silva, P., Morais, J. P. S., Brígida, A. I. S., Muniz, C. R., de Freitas Rosa, M. Development of chlorine-free pulping method to extract cellulose nanocrystals from pressed oil palm mesocarp fibers. *Journal of Biobased Materials and Bioenergy*, 9(3): 372-379, 2015.
- [44] Queiroz, M. F., Teodosio Melo, K. R., Sabry, D. A., Sasaki, G. L., and Rocha, H. Does the use of chitosan contribute to oxalate kidney stone formation? *Marine drugs*, 13(1): 141-158, 2014.
- [45] Vretik, L., Kyrychenko, V., Smolyakov, G., Yaroshchuk, O., Zagniy, V., Gavrilkov, T., Syromyatnikov, V. Photochemical transformations in bis-methacrylic polymers for liquid crystal photoalignment: IR spectroscopy studies. *Molecular Crystals and Liquid Crystals*, 536(1): 224/[456]-235/[467], 2011.
- [46] Varrica, D., Tamburo, E., Vultaggio, M., Di Carlo, I. ATR-FTIR spectral analysis and soluble components of PM₁₀ and PM_{2.5} particulate matter over the urban area of Palermo (Italy) during normal days and Saharan events. *International journal of environmental research and public health*, 16(14): 2507, 2019.
- [47] Saif, S., Tahir, A., Asim, T., Chen, Y., Adil, S. F. Polymeric nanocomposites of iron-oxide nanoparticles (IONPs) synthesized using Terminalia chebula leaf extract for enhanced adsorption of arsenic (V) from water. *Colloids and Interfaces*, 3(1): 17, 2019.
- [48] James, J., Nancy, P., Vignaud, G., Grohens, Y., Thomas, S., and Kalarikkal, N. Laser assisted synthesis of graphene quantum dots for multifunctional applications. In *AIP conference proceedings*. (AIP Publishing), 2019.

- [49] Berzina-Cimdina, L., Borodajenko, N. Research of calcium phosphates using Fourier transform infrared spectroscopy. *Infrared spectroscopy-materials science, engineering and technology*, 12(7): 251-263, 2012.
- [50] Asapur, P., Mahapatra, S. K., Banerjee, I. Secondary structural analysis of non-mulberry silk fibroin nanoparticles synthesized by using microwave and acetone method. *Journal of Biomolecular Structure and Dynamics*, 40(9): 4100-4109, 2022.
- [51] Lv, C., Wang, H., Liu, Z., Wang, C., Zhang, W., Li, M., and Zhu, Y. Fabrication of durable fluorine-free polyphenylene sulfide/silicone resin composite superhydrophobic coating enhanced by carbon nanotubes/graphene fillers. *Progress in Organic Coatings*, 134: 1-10, 2019.
- [52] Ling, S., Qi, Z., Knight, D. P., Shao, Z., and Chen, X. Synchrotron FTIR microspectroscopy of single natural silk fibers. *Biomacromolecules*, 12(9): 3344-3349, 2011.
- [53] Chankow, S., Luemunkong, S., and Kanokpanont, S. Conformational transitions of thai silk fibroin secondary structures. In *2016 9th Biomedical Engineering International Conference (BMEiCON)*. 1-5 (IEEE).
- [54] Kamalha, E., Zheng, Y. S., Zeng, Y. C., and Fredrick, M. FTIR and WAXD study of regenerated silk fibroin. *Advanced Materials Research*, 677: 211-215, 2013.
- [55] Hu, X., Kaplan, D., and Cebe, P. Dynamic protein– water relationships during β -sheet formation. *Macromolecules*, 41(11): 3939-3948, 2008.
- [56] Bhat, N. and Nadiger, G. Crystallinity in silk fibers: Partial acid hydrolysis and related studies. *Journal of Applied Polymer Science*, 25(5): 921-932, 1980.
- [57] Taddei, P., Arai, T., Boschi, A., Monti, P., Tsukada, M., and Freddi, G. J. B. In vitro study of the proteolytic degradation of *Antheraea pernyi* silk fibroin. *Biomacromolecules*, 7(1): 259-267, 2006.
- [58] Arafat, A., Samad, S. A., Masum, S. M., Moniruzzaman, M. Preparation and characterization of chitosan from shrimp shell waste. *International journal of scientific & engineering research*, 6(5): 538-541, 2015.
- [59] Kashte, S., Arbade, G., Sharma, R., Kadam, S. Herbally painted biofunctional scaffolds with improved osteoinductivity for bone tissue engineering. *Journal of Biomimetics, Biomaterials and Biomedical Engineering*, 41: 49-68, 2019.
- [60] Brožová, L., Holler, P., Kovářová, J., Stejskal, J., Trchová, M. The stability of polyaniline in strongly alkaline or acidic aqueous media. *Polymer Degradation and Stability*, 93(3): 592-600, 2008.
- [61] Qin, S., Wang, J., Zhao, C., Zhang, S. Long-term, low temperature simulation of early diagenetic alterations of organic matter: A FTIR study. *Energy Exploration & Exploitation*, 28(5): 365-376, 2010.
- [62] Huang, Y., Li, S., Chen, J., Zhang, X., and Chen, Y. Adsorption of Pb (II) on mesoporous activated carbons fabricated from water hyacinth using H₃PO₄ activation: adsorption capacity, kinetic and isotherm studies. *Applied Surface Science*, 293: 160-168, 2014.
- [63] Barth, A. Infrared spectroscopy of proteins. *Biochimica et Biophysica Acta (BBA)-Bioenergetics*, 1767(9): 1073-1101, 2007.
- [64] Sari, I. P. and Simarani, K. Comparative static and shaking culture of metabolite derived from methyl red degradation by *Lysinibacillus fusiformis* strain W1B6. *Royal Society open science*, 6(7): 190152, 2019.

- [65] Workman Jr. *Concise Handbook Of Analytical Spectroscopy, The: Theory, Applications, And Reference Materials (In 5 Volumes)*. World Scientific, 2016.
- [66] Hu, X., Kaplan, D., and Cebe, P. Determining beta-sheet crystallinity in fibrous proteins by thermal analysis and infrared spectroscopy. *Macromolecules*, 39(18): 6161-6170, 2006.
- [67] Zhang, Y., Zhao, W., Yang, R. Steam flash explosion assisted dissolution of keratin from feathers. *ACS Sustainable Chemistry & Engineering*, 3(9): 2036-2042, 2015.
- [68] Hay, M. B. and Myneni, S. C. Structural environments of carboxyl groups in natural organic molecules from terrestrial systems. Part 1: Infrared spectroscopy. *Geochimica et cosmochimica acta*, 71(14): 3518-3532, 2007.
- [69] Masaki, S., Nakano, Y., Ichiyoshi, K., Kawamoto, K., Takeda, A., Ohnuki, T., Hochella Jr, M. F., and Utsunomiya, S. Adsorption of extracellular polymeric substances derived from *S. cerevisiae* to ceria nanoparticles and the effects on their colloidal stability. *Environments*, 4(3): 48, 2017.
- [70] Asakura, T. J. M. Structure of silk I (*Bombyx mori* silk fibroin before spinning)-type II β -turn, not α -helix. *Molecules*, 26(12): 3706, 2021.
- [71] Goormaghtigh, E., Gasper, R., Bénard, A., Goldsztein, A., Raussens, V. Protein secondary structure content in solution, films and tissues: redundancy and complementarity of the information content in circular dichroism, transmission and ATR FTIR spectra. *Biochimica et Biophysica Acta (BBA)-Proteins and Proteomics*, 1794(9): 1332-1343, 2009.
- [72] Patwa, R., Singh, M., Kumar, A., and Katiyar, V. Kinetic modelling of thermal degradation and non-isothermal crystallization of silk nano-discs reinforced poly (lactic acid) bionanocomposites. *Polymer Bulletin*, 76: 1349-1382, 2019.
- [73] Hu, Y., Zhang, Q., You, R., Wang, L., Li, M. The relationship between secondary structure and biodegradation behavior of silk fibroin scaffolds. *Advances in Materials Science and Engineering*, 185905, 2012.
- [74] Lin, S.-Y., Hsu, C.-H., Sheu, M. Curve-fitting FTIR studies of loratadine/hydroxypropyl- β -cyclodextrin inclusion complex induced by co-grinding process. *Journal of pharmaceutical and biomedical analysis*, 53(3): 799-803, 2010.
- [75] Yadav, A. and Rai, M. Bioreduction and mechanistic aspects involved in the synthesis of silver nanoparticles using *Holarrhena antidysenterica*. *Journal of Bionanoscience*, 5(1): 70-73, 2011.
- [76] Yang, H., Yang, S., Kong, J., Dong, A., and Yu, S. Obtaining information about protein secondary structures in aqueous solution using Fourier transform IR spectroscopy. *Nature protocols*, 10(3): 382-396, 2015.
- [77] Lefèvre, T., Subirade, M. Structural and interaction properties of β -Lactoglobulin as studied by FTIR spectroscopy. *International Journal of Food Science & Technology*, 34(5-6): 419-428, 1999.
- [78] Fabian, H., Vogel, H. Fourier transform infrared spectroscopy of calcium-binding proteins. *Calcium-Binding Protein Protocols: Volume 2: Methods and Techniques*, 57-74, 2002.
- [79] De Jongh, H. H., Goormaghtigh, E., and Ruyschaert, J. The different molar absorptivities of the secondary structure types in the amide I region: an attenuated total reflection infrared study on globular proteins. *Analytical biochemistry*, 242(1): 95-103, 1996.

- [80] Slayton, R. M. and Anfinrud, P. Time-resolved mid-infrared spectroscopy: methods and biological applications. *Current opinion in structural biology*, 7(5): 717-721, 1997.
- [81] Tsukada, M., Freddi, G., Gotoh, Y., and Kasai, N. Physical and chemical properties of tussah silk fibroin films. *Journal of Polymer Science Part B: Polymer Physics*, 32(8): 1407-1412, 1994.
- [82] Lucas, F., Shaw, J., and Smith, S. The Chemical Constitution of some Silk Fibroins and its Bearing on their Physical Properties. *Journal of the Textile Institute Transactions*, 46(6): T440-T452, 1955.
- [83] Tao, W., Li, M., and Zhao, C. Structure and properties of regenerated *Antheraea pernyi* silk fibroin in aqueous solution. *International Journal of Biological Macromolecules*, 40(5): 472-478, 2007.
- [84] Hang, Y., Zhang, Y., Jin, Y., Shao, H., and Hu, X. Preparation of regenerated silk fibroin/silk sericin fibers by coaxial electrospinning. *International journal of biological macromolecules*, 51(5): 980-986, 2012.
- [85] Li, M., Lu, S., Wu, Z., Yan, H., Mo, J., and Wang, L. Study on porous silk fibroin materials. I. Fine structure of freeze dried silk fibroin. *Journal of applied polymer science*, 79(12): 2185-2191, 2001.
- [86] Gulrajani, M. Degumming of silk. *Review of Progress in Coloration and Related Topics*, 22(1): 79-89, 1992.
- [87] Rajkhowa, R., Wang, L., Kanwar, J. R., and Wang, X. Molecular weight and secondary structure change in eri silk during alkali degumming and powdering. *Journal of applied polymer science*, 119(3): 1339-1347, 2011.
- [88] Zhou, Y. and Tang, R. Influence of fixing treatment on the color fastness and bioactivities of silk fabric dyed with curcumin. *The Journal of the Textile Institute*, 108(6): 1050-1056, 2017.
- [89] Price, L. C. and Buescher, R. Decomposition of turmeric curcuminoids as affected by light, solvent and oxygen 1. *Journal of food biochemistry*, 20(5): 125-133, 1996.
- [90] Tønnesen, H. H., Másson, M., and Loftsson, T. Studies of curcumin and curcuminoids. XXVII. Cyclodextrin complexation: solubility, chemical and photochemical stability. *International journal of pharmaceuticals*, 244(1-2): 127-135, 2002.
- [91] Suwannateep, N., Wanichwecharungruang, S., Haag, S., Devahastin, S., Groth, N., Fluhr, J., Lademann, J., Meinke, M. Encapsulated curcumin results in prolonged curcumin activity in vitro and radical scavenging activity ex vivo on skin after UVB-irradiation. *European journal of pharmaceuticals and biopharmaceuticals*, 82(3): 485-490, 2012.
- [92] Tønnesen, H. H., De Vries, H., Karlsen, J., and Van Henegouwen, G. Studies on curcumin and curcuminoids IX: investigation of the photobiological activity of curcumin using bacterial indicator systems. *Journal of pharmaceutical sciences*, 76(5): 371-373, 1987.
- [93] Gupta, V. K. Fundamentals of natural dyes and its application on textile substrates. *Chemistry and technology of natural and synthetic dyes and pigments*, 2019.
- [94] Zhou, C. Z., Confalonieri, F., Jacquet, M., Perasso, R., Li, Z. G., Janin, J. Silk fibroin: structural implications of a remarkable amino acid sequence. *Proteins: Structure, Function, and Bioinformatics*, 44(2): 119-122, 2001.

- [95] Ghoreishian, S. M., Maleknia, L., Mirzapour, H., Norouzi, M. Antibacterial properties and color fastness of silk fabric dyed with turmeric extract. *Fibers and Polymers*, 14: 201-207, 2013.
- [96] Witzel, C. and Gegenfurtner, K. Category effects on colour discrimination. *Colour studies: A broad spectrum*, 200-211, 2014.
- [97] Blackburn, R., Burkinshaw, S., Collins, G. The application of cationic fixing agents to cotton dyed with direct dyes under different pH conditions. *Journal of the Society of Dyers and Colourists*, 114(11): 317-320, 1998.
- [98] Tang, R.-C., Tang, H., Yang, C. Adsorption isotherms and mordant dyeing properties of tea polyphenols on wool, silk, and nylon. *Industrial & engineering chemistry research*, 49(19): 8894-8901, 2010.
- [99] Ganesan, P. and Karthik, T. Analysis of colour strength, colour fastness and antimicrobial properties of silk fabric dyed with natural dye from red prickly pear fruit. *The journal of the textile institute*, 108(7): 1173-1179, 2017.
- [100] Zhou, Y., Zhang, J., Tang, R.-C., Zhang, J. Simultaneous dyeing and functionalization of silk with three natural yellow dyes. *Industrial crops and products*, 64: 224-232, 2015.
- [101] Taiz, L., Zeiger, E., Møller, I. M., and Murphy, A. *Plant physiology and development*. Sinauer Associates Incorporated, 2015.
- [102] Habib, N., Akram, W., Adeel, S., Amin, N., Hosseinezhad, M., Haq, E. Environmental-friendly extraction of Peepal (*Ficus Religiosa*) bark-based reddish brown tannin natural dye for silk coloration. *Environmental Science and Pollution Research*, 29(23): 35048-35060, 2022.
- [103] Gupta, S. C., Prasad, S., Kim, J. H., Patchva, S., Webb, L. J., Priyadarsini, I. K., and Aggarwal, B.. Multitargeting by curcumin as revealed by molecular interaction studies. *Natural product reports*, 28(12): 1937-1955, 2011.
- [104] Palaskar, S. S., Kale, R. D., Deshmukh, R.. Application of natural yellow (curcumin) dye on silk to impart multifunctional finishing and validation of dyeing process using BBD model. *Color Research & Application*, 46(6): 1301-1312, 2021.
- [105] Zhang, W., Yang, Z.-Y., Cheng, X.-W., Tang, R.-C., and Qiao, Y. Adsorption, antibacterial and antioxidant properties of tannic acid on silk fiber. *Polymers*, 11(6): 970, 2019.
- [106] Chen, J., Ni, Y., Mei, B., Jiang, H., Wang, Y., Chen, Y., and Qi, H. Extraction of pigments from camellia seed husks and their application on silk fabrics. *RSC advances*, 12(53): 34715-34723, 2022.
- [107] Gülçin, İ., Huyut, Z., Elmastaş, M., and Aboul-Enein, H. Radical scavenging and antioxidant activity of tannic acid. *Arabian journal of chemistry*, 3(1): 43-53, 2010.
- [108] Luo, T., Yang, L., Wu, J., Zheng, Z., Li, G., Wang, X., Kaplan, D. Stabilization of natural antioxidants by silk biomaterials. *ACS applied materials & interfaces*, 8(21): 13573-13582, 2016.
- [109] Priyadarsini, K. I. The chemistry of curcumin: from extraction to therapeutic agent. *Molecules*, 19(12): 20091-20112, 2014.
- [110] Priyadarsini, K. I., Maity, D. K., Naik, G., Kumar, M. S., Unnikrishnan, M., Satav, J., Mohan, H. Role of phenolic OH and methylene hydrogen on the free radical reactions and antioxidant activity of curcumin. *Free Radical Biology and Medicine*, 35(5): 475-484, 2003.

Physico-chemical, Antibacterial, Antioxidant, Bio Compatibility, and Biodegradation Studies of Washed and Dyed Eri, Muga, and Pat Silk Fabric

- [111] Barclay, L. R. C., Vinqvist, M. R., Mukai, K., Goto, H., Hashimoto, Y., Tokunaga, A., and Uno, H. On the antioxidant mechanism of curcumin: classical methods are needed to determine antioxidant mechanism and activity. *Organic letters*, 2(18): 2841-2843, 2000.
- [112] Jha, N. S., Mishra, S., Jha, S. K., and Surolia, A. Antioxidant activity and electrochemical elucidation of the enigmatic redox behavior of curcumin and its structurally modified analogues. *Electrochimica Acta*, 151: 574-583, 2015.
- [113] Madusanka, N., de Silva, K. N., and Amaratunga, G. A curcumin activated carboxymethyl cellulose–montmorillonite clay nanocomposite having enhanced curcumin release in aqueous media. *Carbohydrate polymers*, 134: 695-699, 2015.
- [114] Roy, S., Rhim, J. Preparation of antimicrobial and antioxidant gelatin/curcumin composite films for active food packaging application. *Colloids and Surfaces B: Biointerfaces*, 188: 110761, 2020.
- [115] Margariti, C. The effects of micro-organisms in simulated soil burial on cellulosic and proteinaceous textiles and the morphology of the fibres. *Studies in Conservation*, 66(5): 282-297, 2021.
- [116] Peacock, E. Biodegradation and characterization of water-degraded archaeological textiles created for conservation research. *International biodeterioration & biodegradation*, 38(1): 49-59, 1996.
- [117] Srinivasan, R. and Jakes, K. Examination of Silk Fibers from a Deep Ocean Site: SEM, EDS, & DSC. *MRS Online Proceedings Library (OPL)*, 462, 1996.
- [118] Sölar, V., Devrim, G. Biodegradation behaviour of different textile fibres: visual, morphological, structural properties and soil analyses. *Fibres & Textiles in Eastern Europe*, (1 (133)): 100--111, 2019.
- [119] Cao, Y. and Wang, B. Biodegradation of silk biomaterials. *International journal of molecular sciences*, 10(4): 1514-1524, 2009.
- [120] Altman, G. H., Diaz, F., Jakuba, C., Calabro, T., Horan, R. L., Chen, J., Lu, H., Richmond, J., and Kaplan, D. L. Silk-based biomaterials. *Biomaterials*, 24(3): 401-416, 2003.
- [121] Rossitch, E., Bullard, D. E., and Oakes, W. J. Delayed foreign-body reaction to silk sutures in pediatric neurosurgical patients. *Child's Nervous System* 3: 375-378, 1987.
- [122] Soong, H. K. and Kenyon, K. R. Adverse reactions to virgin silk sutures in cataract surgery. *Ophthalmology*, 91(5): 479-483, 1984.
- [123] Salthouse, T. N., Matlaga, B. F., and Wykoff, M. H. Comparative tissue response to six suture materials in rabbit cornea, sclera, and ocular muscle. *American Journal of Ophthalmology*, 84(2): 224-233, 1977.
- [124] Prachayawarakorn, J. and Kryratsamee, W. Dyeing properties of Bombyx mori silks grafted with methyl methacrylate and methacrylamide. *Journal of applied polymer science*, 100(2): 1169-1175, 2006.
- [125] Shubhra, Q. T., Alam, A., and Beg, M. Mechanical and degradation characteristics of natural silk fiber reinforced gelatin composites. *Materials letters*, 65(2): 333-336, 2011.
- [126] Choi, S. Foxing on paper: a literature review. *Journal of the American Institute for Conservation*, 46(2): 137-152, 2007.
- [127] Chen, R. *A study of cotton fibers recovered from a marine environment*. The Ohio State University, 1998.

- [128] Banerjee, S. RETRACTED ARTICLE: Glyoxal modification mediates conformational alterations in silk fibroin: Induction of fibrillation with amyloid features. *Journal of Biosciences*, 45(1): 32, 2020.
- [129] Zafar, M. S., Belton, D. J., Hanby, B., Kaplan, D. L., and Perry, C. Functional material features of Bombyx mori silk light versus heavy chain proteins. *Biomacromolecules*, 16(2): 606-614, 2015.
- [130] Muthumanickam, A., Subramanian, S., Goweri, M., Sofi Beaula, W., and Ganesh, V. Comparative study on eri silk and mulberry silk fibroin scaffolds for biomedical applications. *Iranian Polymer Journal*, 22: 143-154, 2013.
- [131] Sheik, S., Nagaraja, G., Prashantha, K. Effect of silk fiber on the structural, thermal, and mechanical properties of PVA/PVP composite films. *Polymer Engineering & Science*, 58(11): 1923-1930, 2018.
- [132] Jesurani, S., Kanagesan, S., Velmurugan, R., and Kalaivani, T. Phase formation and high dielectric constant of calcium copper titanate using sol-gel route. *Journal of Materials Science: Materials in Electronics*, 23: 668-674, 2012.
- [133] Ami, D., Mereghetti, P., Leri, M., Giorgetti, S., Natalello, A., Doglia, S. M., Stefani, M., and Bucciantini, M. A FTIR microspectroscopy study of the structural and biochemical perturbations induced by natively folded and aggregated transthyretin in HL-1 cardiomyocytes. *Scientific Reports*, 8(1): 12508, 2018.
- [134] Cebe, P., Partlow, B. P., Kaplan, D. L., Wurm, A., Zhuravlev, E., and Schick, C. Silk I and Silk II studied by fast scanning calorimetry. *Acta Biomaterialia*, 55: 323-332, 2017.
- [135] Navarro-Pardo, F., Martínez-Barrera, G., Martínez-Hernández, A. L., Castaño, V. M., Rivera-Armenta, J. L., Medellín-Rodríguez, F., and Velasco-Santos, C. J. M. Effects on the thermo-mechanical and crystallinity properties of nylon 6, 6 electrospun fibres reinforced with one dimensional (1D) and two dimensional (2D) carbon. *Materials*, 6(8): 3494-3513, 2013.
- [136] Prekajski, M., Mirković, M., Todorović, B., Matković, A., Marinović-Cincović, M., Luković, J., and Matović, B. Ouzo effect—New simple nanoemulsion method for synthesis of strontium hydroxyapatite nanospheres. *Journal of the European Ceramic Society*, 36(5): 1293-1298, 2016.
- [137] Krisanti, E., Safiya, A., and Mulia, K. Formulation and characterization of chitosan-alginate freeze dried matrices loaded with oleoresin extract of red ginger. In *IOP Conference Series: Materials Science and Engineering*. 012008 (IOP Publishing).
- [138] Rajkhowa, R., Gil, E. S., Kluge, J., Numata, K., Wang, L., Wang, X., and Kaplan, D. L. Reinforcing silk scaffolds with silk particles. *Macromolecular bioscience*, 10(6): 599-611, 2010.
- [139] Farahmandjou, M. and Soflaee, F. J. P. C. R. Synthesis and characterization of α -Fe₂O₃ nanoparticles by simple co-precipitation method. *Physical Chemistry Research*, 3(3): 191-196, 2015.
- [140] Trivedi, M., Patil, S., Shettigar, H., Bairwa, K., and Jana, S. Spectroscopic characterization of biofield treated metronidazole and tinidazole. *Medicinal chemistry*, 7(5): 340-344, 2015.
- [141] SHIMADZU. *Protein Secondary Structural Analysis by FTIR*. Retrieved on from <https://www.shimadzu.com/an/industries/life-science/life-science-proteomics/protein-secondary/index.html>.

- [142] Li, M.-Y., Zhao, Y., Tong, T., Hou, X.-H., Fang, B.-S., Wu, S.-Q., Shen, X.-Y., Tong, H. Study of the degradation mechanism of Chinese historic silk (*Bombyx mori*) for the purpose of conservation. *Polymer degradation and stability*, 98(3): 727-735, 2013.
- [143] Mansour, E. Semi-quantitative analysis for FTIR spectra of Al₂O₃-PbO-B₂O₃-SiO₂ glasses. *Journal of non-crystalline solids*, 358(3): 454-460, 2012.
- [144] Adamczyk, A., Długoń, E. The FTIR studies of gels and thin films of Al₂O₃-TiO₂ and Al₂O₃-TiO₂-SiO₂ systems. *Spectrochimica Acta Part A: Molecular and Biomolecular Spectroscopy*, 89: 11-17, 2012.
- [145] Lefèvre, T., Rousseau, M.-E., and Pézolet, M. Protein secondary structure and orientation in silk as revealed by Raman spectromicroscopy. *Biophysical journal*, 92(8): 2885-2895, 2007.
- [146] Ittah, S., Barak, N., and Gat, U. A proposed model for dragline spider silk self-assembly: Insights from the effect of the repetitive domain size on fiber properties. *Biopolymers*, 93(5): 458-468, 2010.
- [147] Ganjali, F., Eivazzadeh-Keihan, R., Aghamirza Moghim Aliabadi, H., Maleki, A., Pouri, S., Ahangari Cohan, R., Hashemi, S. M., Mahdavi, M. Biocompatibility and antimicrobial investigation of agar-tannic acid hydrogel reinforced with silk fibroin and zinc manganese oxide magnetic microparticles. *Journal of Inorganic and Organometallic Polymers and Materials*, 32(10): 4057-4069, 2022.
- [148] Hoffman, J. M., Margolis, K. G. Building community in the gut: A role for mucosal serotonin. *Nature Reviews Gastroenterology & Hepatology*, 17(1): 6-8, 2020.
- [149] Zhou, H. Y., Zhang, Y. P., Zhang, W. F., and Chen, X. Biocompatibility and characteristics of injectable chitosan-based thermosensitive hydrogel for drug delivery. *Carbohydrate polymers*, 83(4): 1643-1651, 2011.
- [150] Muthumanickam, A., Subramanian, S., Sathiyaraj, M., Preethi, P., and Ashwini, M. Development of herb based (*Nigella sativa*) eri silk nanofibrous mat for biomedical applications. *Materials Today: Proceedings*, 22: 585-588, 2020.
- [151] Baruah, P. K., Raman, M. A., Chakrabarty, I., Rangan, L., Sharma, A. K., and Khare, A. Antibacterial effect of silk treated with silver and copper nanoparticles synthesized by pulsed laser ablation in distilled water. In *AIP conference proceedings*. 030064 (AIP Publishing LLC).
- [152] Kaur, J., Rajkhowa, R., Afrin, T., Tsuzuki, T., and Wang, X. J. B. Facts and myths of antibacterial properties of silk. *Biopolymers*, 101(3): 237-245, 2014.
- [153] Seves, A., Romanò, M., Maifreni, T., Sora, S., Ciferri, O. J. I. b., and biodegradation. The microbial degradation of silk: a laboratory investigation. *International biodeterioration & biodegradation*, 42(4): 203-211, 1998.
- [154] Zheng, K., Zhong, J., Qi, Z., Ling, S., and Kaplan, D. Isolation of silk mesostructures for electronic and environmental applications. *Advanced Functional Materials*, 28(51): 1806380, 2018.
- [155] Ahmed, M. and Saikia, J. P. A Novel Activated Charcoal Based Wash to Make Muga Silk Shiny. *Journal of Natural Fibers*, 20(1): 2145407, 2023.
- [156] Shah, D. U., Porter, D., Vollrath, F. Opportunities for silk textiles in reinforced biocomposites: Studying through-thickness compaction behaviour. *Composites Part A: Applied Science and Manufacturing*, 62: 1-10, 2014.

- [157] Mishra, S. *A text book of fibre science and technology*. New Age International, 2000.
- [158] Ma, M., You, L., Chen, L., and Zhou, W. Effects of ultrasonic laundering on the properties of silk fabrics. *Textile Research Journal*, 84(20): 2166-2174, 2014.